



**AUTOMATIC MODULATION CLASSIFICATION OF COMMON
COMMUNICATION AND PULSE COMPRESSION RADAR
WAVEFORMS USING CYCLIC FEATURES**

THESIS

John A. Hadjis, Second Lieutenant, USAF

AFIT-ENG-13-M-20

**DEPARTMENT OF THE AIR FORCE
AIR UNIVERSITY**

AIR FORCE INSTITUTE OF TECHNOLOGY

Wright-Patterson Air Force Base, Ohio

**DISTRIBUTION STATEMENT A.
APPROVED FOR PUBLIC RELEASE; DISTRIBUTION UNLIMITED**

The views expressed in this thesis are those of the author and do not reflect the official policy or position of the United States Air Force, the Department of Defense, or the United States Government.

This material is declared a work of the U.S. Government and is not subject to copyright protection in the United States.

AFIT-ENG-13-M-20

AUTOMATIC MODULATION CLASSIFICATION OF COMMON
COMMUNICATION AND PULSE COMPRESSION RADAR
WAVEFORMS USING CYCLIC FEATURES

THESIS

Presented to the Faculty
Department of Electrical and Computer Engineering
Graduate School of Engineering and Management
Air Force Institute of Technology
Air University
Air Education and Training Command
in Partial Fulfillment of the Requirements for the
Degree of Master of Science in Electrical Engineering

John A. Hadjis, B.S.E.E.
Second Lieutenant, USAF

March 2013

DISTRIBUTION STATEMENT A.
APPROVED FOR PUBLIC RELEASE; DISTRIBUTION UNLIMITED

AFIT-ENG-13-M-20

MODULATION CLASSIFICATION OF COMMON COMMUNICATION
AND PULSE COMPRESSION RADAR WAVEFORMS
USING CYCLIC FEATURES

John A. Hadjis, B.S.E.E.
Second Lieutenant, USAF


Approved:



Richard K. Martin, PhD (Chairman)

7 Mar 2013

Date



Michael A. Temple, PhD (Member)

8 Mar 2013

Date



Julie A. Jackson, PhD (Member)

8 Mar 2013

Date

Abstract

This research develops a feature-based maximum *a posteriori* (MAP) classification system and applies it to classify several common pulse compression radar and communication modulations. All signal parameters are treated as unknown to the classifier system except SNR and the signal carrier frequency. The features are derived from estimated duty cycle, cyclic spectral correlation, and cyclic cumulants. The modulations considered in this research are BPSK, QPSK, 16-QAM, 64-QAM, 8-PSK, and 16-PSK communication modulations, as well as Barker₅ coded, Barker₁₁ coded, Barker_{5,11} coded, Frank₄₉ coded, Px₄₉ coded, and LFM pulse compression modulations. Simulations show that average correct signal modulation type classification $\%C > 90\%$ is achieved for $\text{SNR} > 9\text{dB}$, average signal modulation family classification $\%C > 90\%$ is achieved for $\text{SNR} > 1\text{dB}$, and an average communication versus pulse compression radar modulation classification $\%C > 90\%$ is achieved for $\text{SNR} > -4\text{dB}$. Also, it is shown that the classification performance using selected input features is sensitive to signal bandwidth but not to carrier frequency. Mismatched bandwidth between training and testing signals caused degraded classification of $\%C \approx 10\% - 14\%$ over the simulated SNR range.

For my Family and Friends who listened to my research ramblings and helped me get through the stressful days

Table of Contents

	Page
Abstract	iv
Dedication	v
Table of Contents	vi
List of Figures	viii
List of Tables	x
List of Acronyms	xi
I. Introduction	1
1.1 Research Motivation and Related Research	1
1.2 Research Goal	2
1.3 Research Methodology	3
1.4 Thesis Organization	4
II. Literature Review	5
2.1 Waveforms Considered	5
2.1.1 Communication	5
2.1.2 Radar	8
2.2 Pattern Recognition	15
2.2.1 Likelihood-Based Tests	15
2.2.2 Feature Based Tests	16
2.3 Cyclostationarity	16
2.3.1 Theory	18
2.3.2 Cyclic Autocorrelation Function	19
2.3.3 Spectral Correlation Function	22
2.4 Estimating the Spectral Correlation Function	23
2.4.1 Temporal Smoothing	25
2.4.1.1 FFT Accumulation Method	28
2.4.1.2 Strip Spectral Correlation Algorithm	30
2.4.2 Frequency Smoothing	31
2.5 Cyclic Cumulants	31

	Page
III. Methodology	36
3.1 Simulating Modulations	36
3.2 Simulating SNR with AWGN	41
3.3 Extracting Features	43
3.3.1 Duty Cycle	43
3.3.2 Cyclic Spectral Correlation	45
3.3.3 Cyclic Cumulants	50
3.4 Classifier Training	52
3.5 Performance Criteria	55
IV. Results and Analysis	58
4.1 Simulation Setup	58
4.2 Classifier Performance with Ideal Training Data	60
4.2.1 Signal Modulation Type Classification	60
4.2.2 Signal Modulation Family Classification	65
4.2.3 Communication vs. Pulse Compression Radar Modulation Classification	69
4.3 Classifier Bandwidth Sensitivity	73
4.4 Classifier Carrier Frequency Sensitivity	76
V. Conclusions	77
5.1 Summary	77
5.2 Impact	78
5.3 Recommendations for Future Work	79
Bibliography	80

List of Figures

Figure	Page
2.1 Communication Constellations	7
2.2 Pulse Repetition Interval	10
2.3 Nested Barker _{4,5} Code	14
2.4 Frequency Spectrum of Frequency Translates	21
2.5 SCF Support Region	23
2.6 Temporal Smoothing	27
2.7 FAM Estimate Resolution	29
2.8 SSCA Estimate Resolution	30
2.9 Frequency Smoothing	32
3.1 Waveform Simulation Process	37
3.2 MATLAB® Generated Pulse Shaping Filter Properties	39
3.3 MATLAB® Generated Pulse Shaping Filter Applied to Simulated BPSK Signal	40
3.4 Simulated SNR Scaling Process	41
3.5 Estimating the Duty Cycle in Observation Time Δt	44
3.6 Estimated Duty Cycles Over a Range of SNR _{dB} with 95% Confidence Intervals	45
3.7 Estimated BPSK SCF at SNR = 20dB	46
3.8 Estimated QPSK SCF at SNR = 20dB	47
3.9 Estimated BPSK SCF at SNR = -5dB	48
3.10 Estimated SCF Feature Ratio	50
3.11 Estimated Cyclic Cumulant Spectrums for BPSK	51
3.12 Classifier Training	54
3.13 Test the Classifier	55
3.14 Confusion Matrix	56

Figure	Page
3.15 ROC Curve Examples	57
4.1 Classifier System's Average Performance for 12 Signal Modulation Types with Ideal Training Data	61
4.2 Classifier System's Modulation Type Classification Performance with Ideal Training Data	62
4.3 Classifier System ROCs for 12 Modulation Types at SNR = 9dB	63
4.4 Classifier System ROCs for 12 Modulation Types at SNR = 0dB	64
4.5 Classifier System's Average Performance for 7 Modulation Families with Ideal Training Data	66
4.6 Classifier System's Modulation Family Classification Performance with Ideal Training Data	67
4.7 Classifier System ROCs for 7 Modulation Families at SNR = 0dB	68
4.8 Classifier System's Average Performance for Distinguishing Communication from Pulsed Radar Modulations with Ideal Training Data	69
4.9 Classifier System's Pulsed Radar and Communication Modulation Classifica- tion Performance with Ideal Training Data	70
4.10 Classifier System ROCs for Communication vs Pulsed Radar Detection at SNR = $-5dB$	71
4.11 Classifier System's Performance Sensitivity to Bandwidth	73
4.12 Classifier System's Modulation Type Classification Performance with Mis- matched Bandwidth	74
4.13 Classifier System ROCs for 12 Modulation Types at SNR = 8dB with Mismatched Bandwidth	75
4.14 Classifier System's Performance Sensitivity to Carrier Frequency	76

List of Tables

Table	Page
2.1 Known Barker codes [21]	13
2.2 Some Frank Code Phase Sequences [21]	14
2.3 Some P_x Code Phase Sequences [21]	14
2.4 Cumulant Partitions for $n=4, q=2$	33
2.5 Cumulants	34
3.1 SCF Classifier Features	49
3.2 Cyclic Cumulant Features	52
3.3 Classifier Features	53
4.1 Classifier System's Confusion Matrix for 12 Modulation Types at SNR = 9dB .	61
4.2 Classifier System's Confusion Matrix for the 12 Modulation Types at SNR = 0dB	64
4.3 Modulation Families	65
4.4 Classifier System's Confusion Matrix for 7 Modulation Families at SNR= 0dB	68
4.5 Radar and Communication Waveforms	70
4.6 Classifier System's Confusion Matrix for Communication vs Pulsed Radar Modulations at SNR = -1dB	72
4.7 Classifier System's Confusion Matrix for Communication vs Pulsed Radar Modulations at SNR = -5dB	72
4.8 Classifier System's Confusion Matrix for 12 Modulations Types at SNR = 8dB with Mismatched Bandwidths	75

List of Acronyms

Acronym	Definition
ALRT	average likelihood ratio test
ASK	amplitude shift keying
AWGN	additive white gaussian noise
BPSK	binary phase shift keying
CAF	cyclic autocorrelation function
CC	cyclic cumulant
CTC	cyclic temporal cumulant
CTCF	cyclic temporal cumulant function
DFT	discrete fourier transform
EW	electronic warfare
FAM	fast fourier transform (FFT) accumulation method
FFT	fast fourier transform
FSK	frequency shift keying
GLRT	generalized likelihood ratio test
IF	intermediate frequency
LFM	linear frequency modulation
MAP	maximum <i>a posteriori</i>
MATLAB [®]	matrix laboratory
ML	maximun likelihood
OFDM	orthogonal frequency division multiplexing
PDF	probability density function
PMF	probability mass function
PRI	pulse repetition interval

Acronym	Definition
PSD	power spectral density
PSK	phase shift keying
QAM	quadrature amplitude modulation
QPSK	quadrature phase shift keying
RADAR	radio detection and ranging
RF	radio frequency
ROC	receiver operating characteristic
SCF	spectral correlation function
SDR	software defined radio
SNR	signal to noise ratio
SSCA	strip spectral correlation algorithm
TCF	temporal cumulant function
TMF	temporal moment function
WSCS	wide-sense cyclo-stationary
WSS	wide-sense stationary

AUTOMATIC MODULATION CLASSIFICATION OF COMMON
COMMUNICATION AND PULSE COMPRESSION RADAR
WAVEFORMS USING CYCLIC FEATURES

I. Introduction

THIS chapter summarizes the research presented in this thesis. Its motivation and goals are explained, as well as the assumptions used to limit the problem's scope. Last, the organization of information and results presented in this thesis are explained.

1.1 Research Motivation and Related Research

In this digital age, with increasing technology and decreasing electronic component size, many capabilities are being integrated into single complex systems. Also, the ever increasing need for higher data rates and larger bandwidths in the electromagnetic spectrum is demanding efficient, adaptive new methods to utilize the licensed and unlicensed spectrums. The difficult task of increasing spectrum usage while mitigating incurred interference between independent signals can benefit from automatic modulation recognition processes applied to non-cooperative signals of interest.

Cognitive radio technology with software defined radios (SDRs) is receiving much research interest as a potential solution for spectrum management problems because SDRs can adaptively change critical parameters of their receive and transmit operations to adjust to current channel conditions. Accurately sensing and extracting information about current spectrum usage is a key process for a cognitive radio system. In fact, many research papers are solely focused on spectrum sensing techniques for cognitive radios [2, 18, 29]. The increasing complexity of electromagnetic environments is also providing new challenges

for electronic warfare (EW). Spectrums are beginning to overlap and user transmissions are becoming more dynamic in time, frequency, and modulation. Improved sensing techniques of the electromagnetic spectrum is key for future communication and radar systems such as cognitive radios and cognitive radars.

Within spectrum sensing research, automatic modulation recognition has emerged as an important process in cognitive spectrum management and EW applications. Research has been conducted on automatic classification of both digital and analog modulations for at least two decades, and possible applications in cognitive radar and communication systems include threat recognition and analysis, communication interception/demodulation, effective adaptive jammer response, and communication/radar emitter identification [5, 23]. The research continues to trend towards larger modulation sets and more complicated channel environments with minimal *a priori* signal knowledge.

In [30], the feasibility of providing automatic modulation recognition as an integrative technology for radar and communication signals based on features was investigated, but only a limited set of modulation types were simulated and varying signal to noise ratio (SNR) analysis was not provided. [30] is the only research found that addresses both radar and communication waveform modulation recognition. This area remains relatively unexplored and is the focus of this research. A large modulation set including both pulse compression radar and communication modulations is explored for modulation classification with minimal knowledge *a priori* of critical received signal parameters.

1.2 Research Goal

The goal of my research is to advance the application of modulation classification presented in the literature by developing and simulating a reliable automatic modulation recognition system capable of discerning between a wide range of non-cooperative common pulse compression radar and communication modulations. Simulated performance

and limitations of the developed system will be assessed over a wide range of received SNR and varying received signal parameters.

1.3 Research Methodology

First, a wide set of communication and pulse compression radar modulations are simulated with varying SNRs by adding additive white gaussian noise (AWGN). Then, promising distinguishing features are researched and chosen for use in a classifier system. The research is directed by the literature which documents successful feature-based classification methods. This thesis applies these research findings to develop and simulate a reliable modulation classification system for both common communication and pulse compression radar modulations.

In [5], a survey is provided of prior research for automatic communication modulation classification techniques. These techniques are organized by statistical-based and feature-based methods. Although statistical-based techniques are theoretically optimal, they are practically inefficient due to computational complexity. Feature-based techniques using cyclic spectrum features and cumulants are shown to have performed well for varying sets of communication modulations and unknown parameters. These same parameters were also shown to perform well for radar waveform modulation recognition in [23], and [30] illustrated that the estimated duty cycle of a received waveform may be used to distinguish between pulsed radar (linear frequency modulation (LFM) and bi-phase barker₅ coded) and conventional communication (AM, FM, ASK, FSK, BPSK, QPSK) signals with 100% accuracy for SNR greater than 8dB.

The research performed in this thesis is focused on leveraging signal properties that have been shown to be successful modulation classification features to develop a versatile classifier system capable of reliably classifying the modulation of several common communication and radar modulated waveforms. These signal properties include signal duty cycle, cyclostationarity, and cyclic cumulant statistics which were researched for

classification feature selection to distinguish between binary phase shift keying (BPSK), quadrature phase shift keying (QPSK), 16-quadrature amplitude modulation (QAM), 64-QAM, 8-phase shift keying (PSK), and 16-PSK communication signals as well as bi-phase Barker₅ coded, bi-phase Barker₁₁ coded, bi-phase Barker_{5,11} coded, Frank₄₉ coded, P_X₄₉ coded, and LFM pulse compression radar signals.

1.4 Thesis Organization

Chapter II introduces the basic theory of the communication and radar modulations considered, and describes the common classification methods currently utilized for modulation recognition. It then summarizes the theory found in literature concerning cyclostationarity and various algorithms to estimate the spectral correlation function (SCF). Last, the topic of cyclic cumulants (CCs) is addressed.

In *Chapter III*, the steps taken to develop the modulation classification system based on the theory provided in *Chapter II* are presented. First, the process of simulating the various communication and radar waveforms is explained as well as the process used to simulate the received SNR. Then, the process of extracting the signal features researched in *Chapter II* and training the classifier algorithm is explained. Last, the criteria used to assess the developed modulation classification system's performance are presented.

Chapter IV provides the classifier's test simulation results as described in *Chapter III*. Figures for probability of correct classification over a wide SNR range, confusion matrices for SNRs of interest, and receiver operating characteristic (ROC) curves for SNRs of interest are presented for multiple test simulations with varying test parameters. These results are analyzed and compared to assess the classifier's performance.

Finally, *Chapter V* gives a summary of the research with an estimate of its findings' theoretical and operational impact. The thesis concludes with a discussion of potential areas for continued research and further testing.

II. Literature Review

THIS chapter provides a theoretical background of concepts used in this research as well as a review of previous work published in the area of interest. Section 2.1 covers the various communications and radar waveforms considered in the research. Section 2.2 introduces the two main approaches to classification and pattern recognition. Section 2.3 provides the development of cyclostationary concepts such as the cyclic autocorrelation function (CAF) and spectral correlation function (SCF). These concepts are extended for practical applications by introducing various methods to estimate the cyclic spectrum of signals in Section 2.4. Last, Section 2.5 provides the framework for higher-order cyclic statistics as used in this work.

2.1 Waveforms Considered

This research includes a broad range of common communication and radar waveforms for modulation recognition analysis. This section presents the fundamental theory for defining each modulation type and provides the general equations that represent them.

2.1.1 *Communication.*

Digital forms of communication can vary envelope, phase, frequency, or any combination of these to relay information through radio frequency (RF) transmission. This information is generally encoded and represented with communication symbols. A modulation scheme utilizing M symbols is referred to as M -ary. The simplest modulation forms only modulate in one domain and are well known as M -ary amplitude shift keying (ASK), M -ary phase shift keying (PSK), and M -ary frequency shift keying (FSK). M -ary quadrature amplitude modulation (QAM) is a form of modulation in which both amplitude and phase are varied to form communication symbols. In this research, binary phase shift keying (BPSK), quadrature phase shift keying (QPSK), 8-PSK, 16-PSK, 16-QAM, and

64-QAM communication modulations are considered. All theory in this section is derived from information found in [24, 26].

M -ary ASK transfers information through its amplitude where each amplitude level represents a communication symbol. Transmitted ASK symbols at a carrier frequency, f_c , fit the mathematical form

$$\text{ASK : } s(t) = A_m \cos(2\pi f_c t) \quad 0 \leq t \leq T_{sym} \quad (2.1)$$

where A_m is one of M distinct envelope amplitudes representing communication symbols. In M -ary PSK, however, amplitude is constant because information is transferred through its carrier phase. The carrier phase may have one of M values in any symbol period T_{sym} given by

$$\theta_m = \frac{2\pi}{M}(m-1) \quad (2.2)$$

where $m = 1, 2, \dots, M$. Therefore, the modulated M -PSK waveform at a carrier frequency is

$$\text{M-PSK : } s_m(t) = A \cos\left(2\pi f_c t + \frac{2\pi}{M}(m-1)\right) \quad (2.3)$$

where $0 \leq t \leq T_{sym}$ and $m = 1, 2, \dots, M$. From Equation (2.3) we can calculate the transmitted symbols for BPSK, QPSK, 8-PSK and 16-PSK:

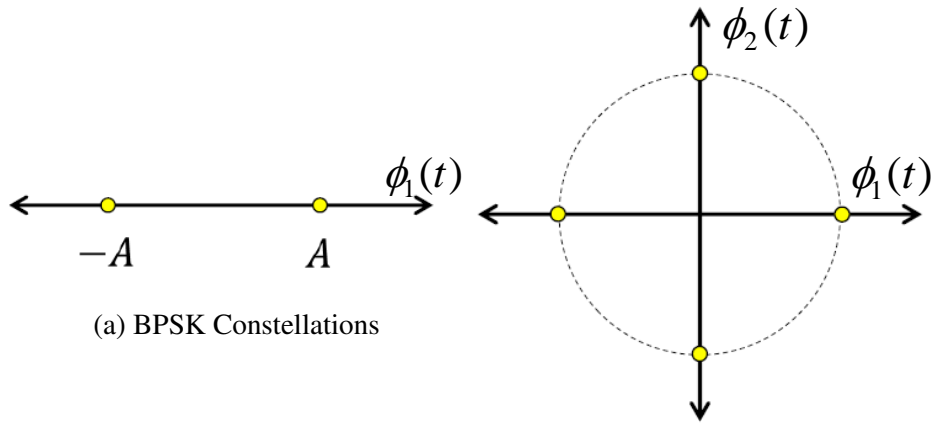
$$\text{BPSK : } s_m(t) = A \cos(2\pi f_c t + m\pi) \quad m = 1, 2 \quad (2.4a)$$

$$\text{QPSK : } s_m(t) = A \cos\left(2\pi f_c t + \frac{\pi}{2}(m-1)\right) \quad m = 1, 2, 3, 4 \quad (2.4b)$$

$$\text{8-PSK : } s_m(t) = A \cos\left(2\pi f_c t + \frac{\pi}{4}(m-1)\right) \quad m = 1, 2, \dots, 8 \quad (2.4c)$$

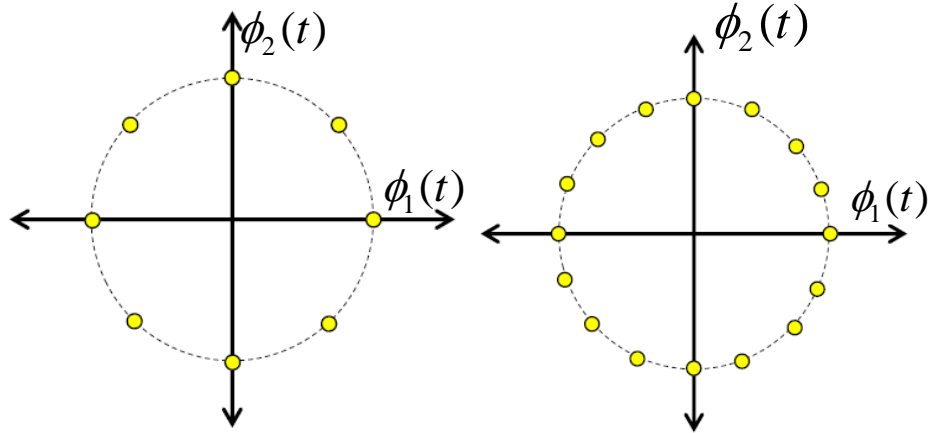
$$\text{16-PSK : } s_m(t) = A \cos\left(2\pi f_c t + \frac{\pi}{8}(m-1)\right) \quad m = 1, 2, \dots, 16 \quad (2.4d)$$

where $0 \leq t \leq T_{sym}$. Utilizing the trig identity $\cos(A+B) = \cos A \cos B - \sin A \sin B$, these transmitted signals can be represented in quadrature form with the basis functions $\phi_1(t) = \cos(2\pi f_c t)$ and $\phi_2(t) = \sin(2\pi f_c t)$. The signal constellations are shown in this two



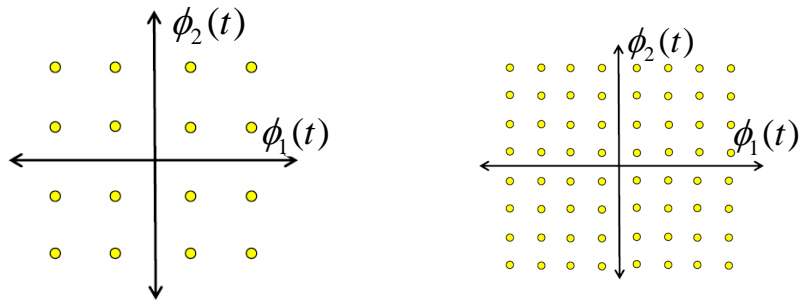
(a) BPSK Constellations

(b) QPSK Constellations



(c) 8 PSK Constellations

(d) 16 PSK Constellations



(e) 16 QAM Constellations

(f) 64 QAM Constellations

Figure 2.1: Communication Constellations

dimensional basis function space in Figure 2.1. Also, M-ary PSK signals have constant envelope magnitudes so the constellation points are equally spaced on a circle of radius A centered at the origin. The constellations for BPSK, QPSK, 8-PSK, and 16-PSK are shown in Figure 2.1a, Figure 2.1b, Figure 2.1c, and Figure 2.1d respectively.

Figure 2.1a illustrates that BPSK can be equal to 2 level antipodal binary ASK. For the case that its two phases are separated by 180° , Equation (2.4a) for BPSK is equal to Antipodal 2-ASK from Equation (2.1). For example, let the phase take the values $\theta = 0$ and π so that the transmitted BPSK signal is

$$s_m(t) = A \cos(2\pi f_c t + m\pi) \quad m = 1, 2 \quad (2.5a)$$

$$= \pm A \cos(2\pi f_c t) \quad (2.5b)$$

It can be seen that although the phase is being shifted, the amplitude of the BPSK signal envelope can take the two values $\pm A$ as in ASK.

M-ary QAM varies both its carrier phase and envelope amplitude to represent data symbols. M-QAM modulated signals can be defined as

$$\text{M-QAM} : s_m(t) = A_m \phi_1(t) + B_m \phi_2(t), \quad 0 \leq t \leq T_{sym}, \quad m = 1, 2, \dots, M \quad (2.6)$$

where $\phi_1(t) = \cos(2\pi f_c t)$, $\phi_2(t) = \sin(2\pi f_c t)$, A_m and B_m are defined as $A_m = (2a_m - 1) - \sqrt{M}$ and $B_m = (2b_m - 1) - \sqrt{M}$ with a_m and b_m all combinations of integers in the set $[1, 2, \dots, \sqrt{M}]$. For 16-QAM, A_m and B_m may have values $[-3, -1, 1, 3]$ and for 64-QAM, A_m and B_m may have values $[-7, -5, -3, -1, 1, 3, 5, 7]$. The constellations for 16-QAM and 64-QAM are therefore square lattices instead of circular and are shown in Figure 2.1e and Figure 2.1f respectively.

2.1.2 Radar.

RADAR stands for radio detection and ranging (RADAR) and it summarizes the two main tasks of RADAR systems. That is to detect targets and determine their range from the RADAR system [21]. The selection of a radar waveform and its specifications are

fundamental to the performance and capabilities of a radar system. Generally, the received signal energy determines the reliability of detection, but the specifications of the waveform are responsible for the accuracy, resolution, and ambiguity of range and Doppler (range rate) of the target [21]. Variables that may be manipulated in RADAR waveforms include: operating frequency, peak power, pulse duration, bandwidth, pulse repetition interval (PRI), modulation type/coding, and polarization. In general, continuous wave RADAR has very good Doppler sensitivities but weak range resolution. Pulsed RADAR is very versatile and, depending on design, can have good radar resolution in Doppler and range estimates to provide both long range detection and adequate resolution. Pulsed waveforms have dominated radar design [21]. Also, due to desirable correlation properties, these waveforms are very similar to common communication modulations. Therefore, this research focuses on recognizing linear frequency modulation (LFM), Barker coded, Frank coded, and Px coded pulse compression radar modulations.

First, general radar equations for the simple, pulsed sinusoid as presented in [28] are included to illustrate the important increased performance realized with pulse compression modulations. Pulse compression modulations utilize many modulation schemes common in communications signals. A fundamental parameter of RF transmission is wavelength. RF wavelength is a function of the speed of light, c and carrier frequency f_c ,

$$\lambda = \frac{c}{f_c}$$

where the speed of light $c = 3 \times 10^8$ m/s. In the most simplistic sense, a single tone RADAR pulse is [28]

$$s(t) = \text{Rect}\left(\frac{t}{\tau}\right) \cos(2\pi f_c t), \quad 0 \leq t \leq \tau \quad (2.7)$$

and the range between a monostatic radar system and a target is given by the range equation [28]

$$R = \frac{cT_r}{2} \quad (2.8)$$

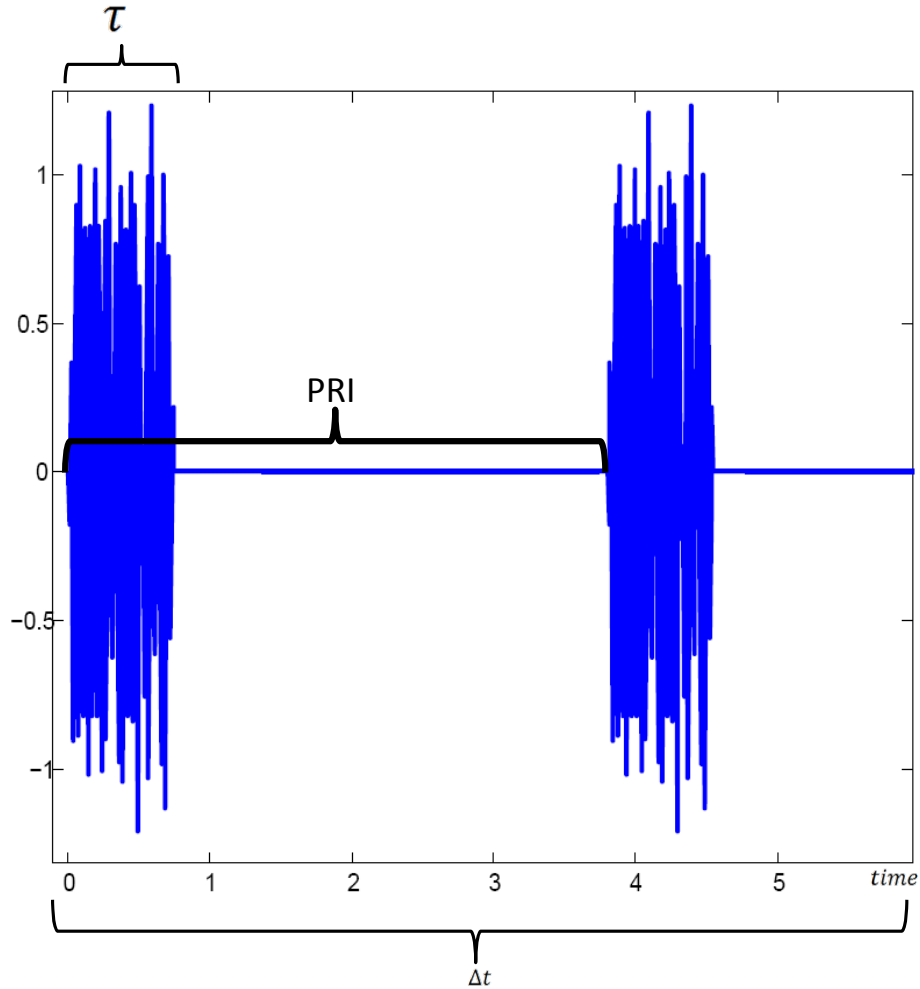


Figure 2.2: Radar Width and Pulse Repetition Interval

where T_r is the round trip time of the radar pulse. Alternatively, the maximum unambiguous range is [28]

$$\text{Unambiguous Range : } R_u = \frac{c \text{ PRI}}{2} \quad (2.9)$$

where the PRI calculated as the time between RADAR pulses. Figure 2.2 shows two radar pulses in an observation interval Δt . The range resolution and accuracy is determined by the pulse's duration τ , the speed of light c , and the received signal to noise ratio (SNR) as in Equation (2.10) and Equation (2.11) respectively [28].

$$\text{Range Resolution : } \Delta R \approx \frac{c \tau}{2} \quad (2.10)$$

$$\text{Range Accuracy : } \delta_R \approx \frac{c \tau}{2 \sqrt{2} \text{ SNR}} \quad (2.11)$$

Range resolution represents the distance required between two distinct targets for the RADAR system to reliably distinguish between them. Equation (2.9), Equation (2.10), and Equation (2.11) provide information for characterizing the performance of a RADAR system. Performance improvements in RADAR systems have been towards greater spatial resolution capabilities of targets with noisy backgrounds [28].

The duty cycle of a constant amplitude pulsed signal is the ratio of the average transmit power over the PRI and the peak transmit power within a pulse [28].

$$\delta_c = \frac{\tau}{\text{PRI}} = \frac{P_{avg}}{P_0} \quad (2.12)$$

The average transmit power P_{avg} is the instantaneous transmitted pulse power's integral over the PRI divided by the PRI and the peak transmitted power P_0 is calculated as the transmitted pulse power's maximum value over the pulse interval τ .

$$P_{avg} = \frac{1}{\text{PRI}} \int_0^{\text{PRI}} p(t) dt \quad (2.13a)$$

$$P_0 = \max(p(t) |_0^\tau) \quad (2.13b)$$

with the instantaneous power of the transmitted pulse $p(t) = |s(t)|^2$.

Range rate, or Doppler, is how the RADAR determines target velocity relative to the RADAR system. The RADAR to target range rate, resolution, and accuracy are given by [28]

$$\text{Range-Rate : } R_{dot} = \frac{f_d \lambda}{2} \quad (2.14a)$$

$$\text{Range-Rate Resolution : } \Delta R_{dot} = \frac{\lambda}{2\tau} \quad (2.14b)$$

$$\text{Range-Rate Accuracy : } \delta_{R_{dot}} = \frac{\lambda}{2\tau \sqrt{2} \text{ SNR}} \quad (2.14c)$$

There is a trade-off between range and range-rate resolution and accuracy determined by the pulse length τ . A long pulse width is desired for acute Doppler resolution and accuracy while a short pulse is desired for fine range resolution and accuracy. However, pulsed radar can achieve both good range and range-rate resolutions through the use of pulse compression techniques. The pulse compression modulations considered in this research are LFM chirped, Barker coded, Frank coded, and P_x coded waveforms.

Pulse compression waveforms allow the receiver to separate targets with overlapping received pulse returns. A compression filter is used to produce a narrow or compressed pulse from the pulse compression modulated received signal. The duration of the pulse is therefore reduced in the receiver and results in a better range resolution than was expected from the transmitted pulse duration [28]. Therefore, pulse compression modulation grants the increased Doppler range resolution of a long-pulse while retaining the range resolution of a narrow-pulse through received echo processing [8].

LFM was the first and still is a widely used pulse compression method. In LFM, the frequency of the signal is swept linearly during the pulse's duration τ over a bandwidth W at the rate $\frac{W}{\tau}$. The effective time-bandwidth product of LFM is $W \times \tau$ and contributes to the increased range resolution of a LFM pulse over a simple sinusoidal pulse. The equation for LFM is [21]

$$\text{LFM} : s(t) = \text{Rect}\left(\frac{t}{\tau}\right) \cos\left(2\pi t\left(f_0 + \frac{W}{2\tau}t\right)\right), \quad 0 \leq t \leq \tau \quad (2.15)$$

where W is the bandwidth that is linearly swept during the pulse duration τ and f_0 is the center frequency. Using a pulse compression receiver, the range resolution is [21]

$$\Delta R \approx \frac{c}{2W} \quad (2.16)$$

which is dependent on the LFM's bandwidth instead of its pulse duration as in Equation (2.10).

The next few pulse compression methods use phase-coded RADAR. Instead of linearly sweeping frequency in a pulse duration τ , phase-coding divides the pulse into M

Table 2.1: Known Barker codes [21]

Code Length	Code
2	11 or 10
3	110
4	1110 or 1101
5	11101
7	1110010
11	11100010010
13	1111100110101

sub-pulses which are assigned a phase value according to a specific phase code sequence. To maintain consistent notation with the communication waveforms, the sub-pulse duration will be referred to as T_{sym} and is calculated as $T_{sym} = \frac{\tau}{M}$ [21].

The next pulse compression method uses a very popular and common family of codes known as Barker codes. Barker codes of M length yield a max peak-to-peak sidelobe ratio of M . There are only nine known Barker codes [21], all listed in Table 2.1; however, Barker codes can be nested to produce larger, sub-optimal sequences such as the length 20 Barker_{4,5} nested code as shown in Figure 2.3. Bi-phase Barker coded RADAR waveforms are expressed as [21]

$$\text{Bi-phase Barker : } s_m(t) = \text{Rect}\left(\frac{t}{\tau}\right) \cos(2\pi f_c t + c_m \pi) , \quad mT_{sym} \leq t \leq (m+1)T_{sym} \quad (2.17)$$

where c_m is the m_{th} value of a known Barker code listed in Table 2.1.

Frank and P_x codes apply for phase sequences of perfect square length $M = L^2$ where s_m for $(1 \leq m \leq M)$ is equal to $s_{(l_1-1)L+l_2}$ for $1 \leq l_1 \leq L$ and $1 \leq l_2 \leq L$. These phase codes produce improved range-rate resolution and accuracy over Barker phase codes [21]. Their sequences are calculated from [21]

$$s_{(l_1-1)L+l_2}(t) = \cos(2\pi f_c t + \phi_{l_1, l_2}) \quad (2.18)$$

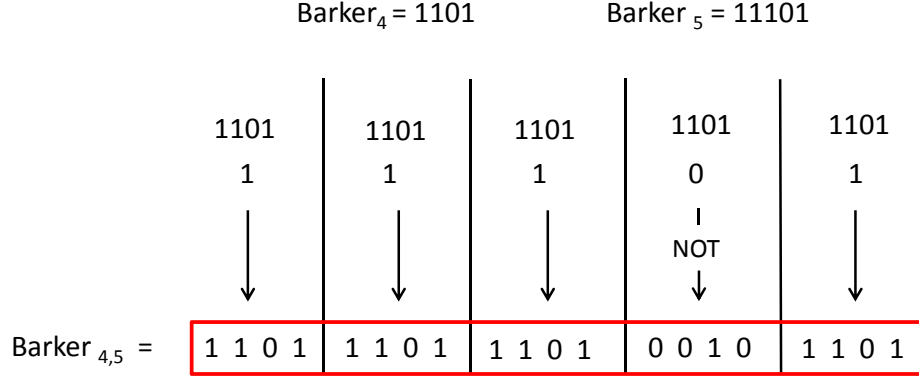


Figure 2.3: Example of nested Barker_{4,5} code

Table 2.2: Some Frank Code Phase Sequences [21]

Code Length	Code
1	0
4	0, 0, 0, π
9	0, 0, 0, 0, $\frac{2\pi}{3}$, $\frac{4\pi}{3}$, 0, $\frac{4\pi}{3}$, $\frac{8\pi}{3}$

Table 2.3: Some P_x Code Phase Sequences [21]

Code Length	Code
1	0
4	$\frac{\pi}{4}$, $\frac{-\pi}{4}$, $\frac{-\pi}{4}$, $\frac{\pi}{4}$
9	$\frac{\pi}{3}$, $\frac{-\pi}{3}$, $-\pi$, 0, 0, 0, $\frac{-\pi}{3}$, $\frac{\pi}{3}$, π

where

$$\text{Frank} : \phi_{l_1, l_2} = 2\pi(l_1 - 1)(l_2 - 1)/L \tag{2.19a}$$

$$\text{P}_x : \phi_{l_1, l_2} = \begin{cases} \frac{2\pi}{L} \left[\frac{(L+1)}{2} - l_2 \right] \left[\frac{(L+1)}{2} - l_1 \right], & L \text{ even} \\ \frac{2\pi}{L} \left[\frac{L}{2} - l_2 \right] \left[\frac{(L+1)}{2} - l_1 \right], & L \text{ odd} \end{cases} \tag{2.19b}$$

Frank phase codes produce linearly stepped linear phase segments as do P_x codes except P_x codes have their zero phase-rate segment terms in the middle of the pulse instead of at the beginning [21]. Phase values for the first three square Frank and P_x phase codes calculated from Equation (2.19) are given in Table 2.2 and Table 2.3 respectively.

2.2 Pattern Recognition

Pattern Recognition has become a very useful tool with applications in many areas including electronic warfare (EW) and Cognitive software defined radio (SDR). Pattern recognition research for selecting and extracting features, developing classifier learning algorithms, and evaluating classifier performance is still prevalent in the literature [1, 5, 7, 19]. For most applications, there are two main methods of pattern recognition that are being used for modulation classification: likelihood-based and feature-based. The likelihood-based approaches strive to minimize false classification and theoretically can achieve near optimal performance, but are impractical in application due to computational complexity. Feature-based methods are much more computationally efficient and have been shown to achieve near optimal performance in the Bayesian sense [5]. A survey of current literature addressing both methods as applied to communication modulation classification was presented in [5] and an example of feature-based classification for radar waveform classification has been presented in [23].

2.2.1 Likelihood-Based Tests.

Likelihood based classification methods hinge on accurately modeling the signal of interest and all other ‘non-signal’ components that comprise the received signal’s probability distribution. Decisions are made by comparing likelihood ratios against a threshold. Among likelihood-based approaches, two ways to model the received signal’s probability distribution are the average likelihood ratio test (ALRT) and generalized likelihood ratio test (GLRT) [5]. Depending on the information known *a priori* about the signals being discriminated, either the ALRT or the GLRT is used.

The ALRT method treats received unknown variables as random variables with assumed known probability density functions (PDFs), but the GLRT method treats the received unknown variables as deterministic unknowns. Therefore the GLRT method does not make any assumptions about the signal or the channel parameters. The final decision is

then based on a maximum likelihood (ML) comparison [5, 22]. For a binary classification problem,

$$\frac{\mathcal{L}_j[H_1|r(t)]}{\mathcal{L}_j[H_0|r(t)]} \underset{H_0}{\overset{H_1}{\gtrless}} \lambda_j, \quad j = A \text{ (ALRT)}, G \text{ (GLRT)} \quad (2.20)$$

where λ_j is a threshold and the method used to compute the likelihood functions \mathcal{L} forms either the ALRT or GLRT on the left side. H_1 represents decision ‘1’, H_0 represents decision ‘0’ in this binary case, and $r(t)$ is the received waveform

2.2.2 Feature Based Tests.

Feature-based classification methods use extracted statistics, or features, from a received signal to make classification decisions based on the reduced data set. This reduced data set is called a feature vector and is represented by $\underline{\psi}$. Some examples of discriminating features include symbol rates, signal magnitude variance, duty cycle, instantaneous frequency, instantaneous phase, cumulants, and many others. Many feature-based methods require some *a priori* knowledge of signal parameters in order to accurately calculate signal features. The extracted signal features are then used for decision making. Decision making methods are usually based on feature PDFs, or feature vector distances from calculated class feature vector means [5].

In literature, cyclostationary-based features have gained popularity as potential features for modulation recognition because they are insensitive to unknown signal and channel parameters and preserve signal phase information [22]. In [27], the received signal’s fourth-order two conjugate cumulants were used as features to discriminate between BPSK, 4-ASK, 16-QAM and 8-PSK when carrier phases, frequency offsets, and timing offsets were unknown.

2.3 Cyclostationarity

A stationary random process is one where all its joint moments are non-varying and all its functions’ expected values are stationary. wide-sense stationary (WSS) is a weaker

form of stationarity, which requires only the 1st and 2nd order statistics to be stationary (not vary with a shift in the time origin). Therefore, a WSS random process has a mean (μ_x) and autocorrelation (R_x) that satisfy the following conditions [11, 20]:

$$\begin{aligned}\mathbf{E}[x(t)] &= \mu_x, \quad \forall t \\ R_x(t, \tau) &= R_x(\tau) \triangleq \mathbf{E}\left[x\left(t + \frac{\tau}{2}\right)x^*\left(t - \frac{\tau}{2}\right)\right], \quad \forall t\end{aligned}$$

where τ is some time delay. Both statistics are independent of the time origin (t) and the auto-correlation function only depends on the time difference (τ) between samples. All stationary random processes are WSS, but not all WSS processes are stationary [20].

Instead of non-varying means and autocorrelations, wide-sense cyclo-stationary (WSCS) random processes have periodic means and autocorrelations [15]. Therefore, for cyclostationary random processes, the mean (μ_x) and autocorrelation (R_x) are periodic for some period T_0 and satisfy the following conditions [11]:

$$\begin{aligned}\mathbf{E}[x(t + T_0)] &= \mu_x(t + T_0) = \mu_x(t), \quad \forall t \\ R_x(t + T_0, \tau) &= R_x(t, \tau) \triangleq \mathbf{E}\left[x\left(t + \frac{\tau}{2}\right)x^*\left(t - \frac{\tau}{2}\right)\right], \quad \forall t\end{aligned}$$

RF waveforms commonly exhibit cyclostationary properties due to common operations such as modulating, coding, multiplexing, and sampling which induce periodicities in the statistics of the signals. The periodicities in autocorrelation produce spectral correlations which can be exploited for signal processing [10].

To accurately calculate $\mu_x(t)$ and $R_x(t, \tau)$, we would have to use ensemble averaging over many observations of a single process and have knowledge of PDFs. However, if time averaging over a single observation is equal to ensemble averaging over many observations, the random process can be described as ergodic. It is a reasonable assumption for most waveforms used in communication and radar applications that the first and second-order statistics within the transmitted waveform satisfy the ergodic property [26]. Therefore, to avoid an unnecessary probabilistic discussion, signals in this paper are assumed to be ergodic in the mean and autocorrelation function. This allows us to treat the temporal

average as equivalent to the expected value, or ensemble average [20]. In this thesis, temporal averaging with respect to t will be denoted as $\langle \cdot \rangle_t$.

$$\mathbf{E}[\cdot] = \langle \cdot \rangle_t \triangleq \lim_{T \rightarrow \infty} \frac{1}{T} \int_{-T/2}^{T/2} (\cdot) dt \approx \lim_{N \rightarrow \infty} \frac{1}{2N+1} \sum_{n=-N}^N (\cdot) \quad (2.21)$$

2.3.1 Theory.

In order to derive the mathematical representation of cyclostationarity and, in turn, produce the SCF, it is easiest to start from simple frequency analysis. Time limited and periodic signals can be expanded into a summation of weighted sinusoids known as a Fourier Series

$$x(t) \triangleq \sum_{n=-\infty}^{+\infty} X_n e^{j\frac{2\pi}{T_0}nt} \triangleq \sum_{n=-\infty}^{+\infty} X_n e^{j2\pi n f_0 t}, \quad n \in \mathbb{I} \quad (2.22)$$

where f_0 , the inverse of the period, T_0 , is the fundamental frequency, \mathbb{I} denotes an integer set, and the coefficients X_n are the sinusoidal component weights at frequencies $f = \frac{n}{T_0} = n f_0$. Therefore, if a signal has a non-zero Fourier Series, it has the additive sinusoidal components of frequency f with weights X_n given by

$$X_n \triangleq \lim_{T \rightarrow \infty} \frac{1}{T} \int_{-T/2}^{T/2} x(t) e^{-j2\pi n f_0 t} dt. \quad (2.23)$$

Let us assume that the signal $x(t)$ contains a finite frequency component given by $a \cos(2\pi\alpha t)$, where a is the frequency magnitude component at $f = \alpha$. Therefore, the complex Fourier Series coefficient of $x(t)$ at frequency α may be represented by [10, 11, 15]

$$M_x^\alpha = \lim_{T \rightarrow \infty} \frac{1}{T} \int_{-T/2}^{T/2} x(t) e^{-j2\pi\alpha t} dt \quad (2.24a)$$

$$= \langle x(t) e^{-j2\pi\alpha t} \rangle_t. \quad (2.24b)$$

and the resulting coefficient M_x^α , for the theoretical $x(t)$ at frequency α equals $\frac{1}{2} a$.

2.3.2 Cyclic Autocorrelation Function.

Now let's progress to a signal produced by the lag-product of another signal. This quadratic transformation produces

$$y(t, \tau) = x\left(t + \frac{\tau}{2}\right)x^*\left(t - \frac{\tau}{2}\right) \quad (2.25)$$

where $(\cdot)^*$ denotes the complex conjugate and τ is a time delay. The signal $y(t)$ contains additive sinusoidal components if and only if

$$M_y^\alpha(\tau) = \left\langle y(t, \tau) e^{-j2\pi\alpha t} \right\rangle_t = \left\langle x\left(t + \frac{\tau}{2}\right)x^*\left(t - \frac{\tau}{2}\right) e^{-j2\pi\alpha t} \right\rangle_t, \quad (2.26)$$

is non-zero for any frequency $\alpha \neq 0$.

It may be apparent that Equation (2.26), the Fourier Coefficients of the lag-product $M_y^\alpha(\tau)$, is a generalized formula of the conventional autocorrelation function of x , $R_x(\tau)$. It can be shown that in the special case where $\alpha = 0$, $M_y^{\alpha=0}(\tau)$ is equivalent to the conventional autocorrelation function $R_x(\tau)$.

$$M_y^{\alpha=0}(\tau) = \left\langle y(t, \tau) e^{-j2\pi 0 t} \right\rangle_t = \left\langle y(t, \tau) \right\rangle_t = \left\langle x\left(t + \frac{\tau}{2}\right)x^*\left(t - \frac{\tau}{2}\right) \right\rangle_t \quad (2.27a)$$

$$R_x(\tau) = \mathbf{E} \left[x\left(t + \frac{\tau}{2}\right)x^*\left(t - \frac{\tau}{2}\right) \right] = \left\langle x\left(t + \frac{\tau}{2}\right)x^*\left(t - \frac{\tau}{2}\right) \right\rangle_t \quad (2.27b)$$

Therefore, $M_y^{\alpha=0}(\tau) = R_x(\tau) = \left\langle x\left(t + \frac{\tau}{2}\right)x^*\left(t - \frac{\tau}{2}\right) \right\rangle_t$ and $M_y^\alpha(\tau)$ may be interpreted as an autocorrelation function of $x(t)$ with a cyclic weighting factor of $e^{-j2\pi\alpha t}$. In literature, $M_y^\alpha(\tau)$ is commonly expressed as the cyclic autocorrelation function (CAF) and is written as [10, 11, 13, 15]

$$R_x^\alpha(\tau) \triangleq \lim_{T \rightarrow \infty} \frac{1}{T} \int_{-T/2}^{T/2} R_x(\tau) e^{-j2\pi\alpha t} dt \quad (2.28a)$$

$$= \left\langle R_x(\tau) e^{-j2\pi\alpha t} \right\rangle_t \quad (2.28b)$$

$$= \left\langle x\left(t + \frac{\tau}{2}\right)x^*\left(t - \frac{\tau}{2}\right) e^{-j2\pi\alpha t} \right\rangle_t. \quad (2.28c)$$

By definition, Equation (2.28) is not identically zero as a function of τ if and only if $x(t)$ contains second-order periodicity with frequency $\alpha \neq 0$. Therefore, the CAF highlights the

second-order periodicities with frequency α in the signal $x(t)$. Also, Equation (2.28) has the same form as Equation (2.24) which tells us that $R_x^\alpha(\tau)$ is a Fourier coefficient in the Fourier series expansion of $R_x(\tau)$ [10].

$$R_x(\tau) \triangleq \sum_{n=-\infty}^{\infty} R_x^\alpha(\tau) e^{j2\pi n \alpha \tau}, \quad \alpha = \frac{n}{T}, \quad n \in \mathbb{I} \quad (2.29)$$

Instead of an autocorrelation function with a cyclic weighting factor, the CAF can also be interpreted as a conventional cross-correlation between two identical signals separated by α in frequency. Let $u(t)$ and $v(t)$ be the signal $x(t)$ multiplied by $e^{\pm j2\pi \frac{\alpha}{2} t}$ which shifts the frequency components of $x(t)$ by $\mp \frac{\alpha}{2}$ as illustrated in Figure 2.4.

$$u(t) = x(t) e^{-j2\pi \frac{\alpha}{2} t} \quad (2.30a)$$

$$v(t) = x(t) e^{j2\pi \frac{\alpha}{2} t} \quad (2.30b)$$

The Fourier transforms of $u(t)$ and $v(t)$ show that their frequency spectrums are

$$U(f) = \mathcal{F}[u(t)] = \mathcal{F}[x(t) e^{-j2\pi \frac{\alpha}{2} t}] = X\left(f + \frac{\alpha}{2}\right) \quad (2.31a)$$

$$V(f) = \mathcal{F}[v(t)] = \mathcal{F}[x(t) e^{j2\pi \frac{\alpha}{2} t}] = X\left(f - \frac{\alpha}{2}\right) \quad (2.31b)$$

and the Wiener-Khinchin relation tells us that the Fourier transforms of $R_u(\tau)$ and $R_v(\tau)$ give us their Power Spectral Densities (PSDs) [3, 12, 20].

$$S_u(f) = S_x\left(f + \frac{\alpha}{2}\right) \quad (2.32a)$$

$$S_v(f) = S_x\left(f - \frac{\alpha}{2}\right). \quad (2.32b)$$

Defining $u(t)$ and $v(t)$ as frequency shifted versions of $x(t)$ leads us to an important conceptual understanding of the CAF. It can be shown that the conventional cross-

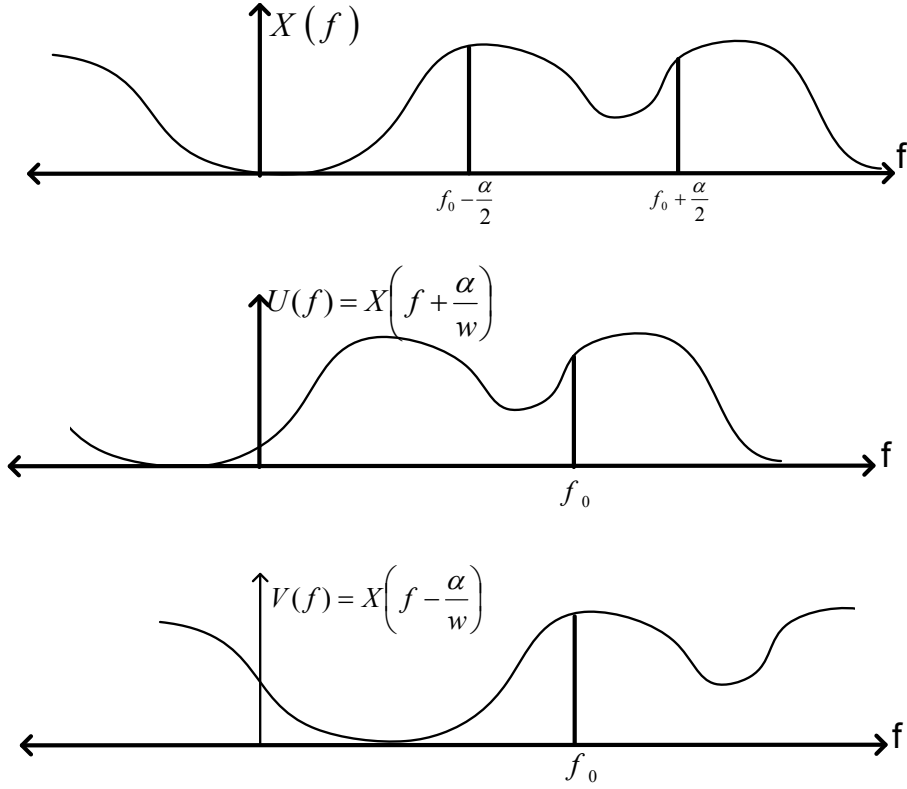


Figure 2.4: Frequency spectrum of frequency translates $u(t)$ and $v(t)$ of $x(t)$

correlation of $u(t)$ and $v(t)$ equals the CAF of $x(t)$.

$$R_{uv}(\tau) \triangleq \mathbf{E} \left[u \left(t + \frac{\tau}{2} \right) v^* \left(t - \frac{\tau}{2} \right) \right] \quad (2.33a)$$

$$= \left\langle u \left(t + \frac{\tau}{2} \right) v^* \left(t - \frac{\tau}{2} \right) \right\rangle_t \quad (2.33b)$$

$$= \left\langle \left[x \left(t + \frac{\tau}{2} \right) e^{-j\pi\alpha(t+\tau/2)} \right] \times \left[x \left(t - \frac{\tau}{2} \right) e^{j\pi\alpha(t-\tau/2)} \right]^* \right\rangle_t \quad (2.33c)$$

$$= \left\langle x \left(t + \frac{\tau}{2} \right) x^* \left(t - \frac{\tau}{2} \right) e^{-j2\pi\alpha t} \right\rangle_t = R_x^\alpha(\tau) \quad (2.33d)$$

$$R_{uv}(\tau) = R_x^\alpha(\tau)$$

This illustrates the interpretation that the CAF is simply a temporal cross-correlation between frequency-shifted versions of a signal.

2.3.3 Spectral Correlation Function.

According to the Wiener-Khinchin and cyclic Wiener-Khinchin relations, the Fourier transform of the autocorrelation function is the power spectral density (PSD) and the Fourier transform of the CAF is the SCF [12, 13].

$$S_x(f) = \int_{-\infty}^{\infty} R_x(\tau) e^{-j2\pi f\tau} d\tau = \mathcal{F} [R_x(\tau)] \quad (2.34a)$$

$$S_x^\alpha(f) = \int_{-\infty}^{\infty} R_x^\alpha(\tau) e^{-j2\pi f\tau} d\tau = \mathcal{F} [R_x^\alpha(\tau)] \quad (2.34b)$$

The SCF is represented on a bi-frequency plane because it is a function of both frequency, f , and cyclic frequency, α . Just as the conventional autocorrelation function is a special case of the CAF for when $\alpha = 0$, the PSD is included in the SCF as the special case when $\alpha = 0$. Remember from Equation (2.33) that the cross-correlation of $u(t)$ and $v(t)$ equals the CAF of $x(t)$. It follows that

$$S_x^\alpha(f) = \mathcal{F} [R_x^\alpha(\tau)] = \mathcal{F} [R_{uv}(\tau)] = S_{uv}(f) \quad (2.35)$$

where $S_{uv}(f)$ is the spectral density of cross correlation between $u(t)$ and $v(t)$ at the frequency f and $S_x^\alpha(f)$ is the spectral density of correlation between the spectral components of $x(t)$ at $f - \frac{\alpha}{2}$ and $f + \frac{\alpha}{2}$. The SCF of $x(t)$ is the Fourier transform of the temporal cross-correlation between frequency-shifted versions of $x(t)$.

Suppose that $x(t)$ in $u(t)$ and $v(t)$ in Equation (2.30) are band-limited with a double-sided bandwidth $2B$. The SCF region of support for a band-limited signal is illustrated in Figure 2.5. At the cyclic frequency of $\alpha = 0$, all spectral components of the correlated frequency translates of $x(t)$ overlap. However, for the cyclic frequency $\alpha = -B$, only spectral components from $-\frac{B}{2}$ to $\frac{B}{2}$ overlap and therefore $S_x^{\alpha=-B}(f)$ only supports the frequency region $-\frac{B}{2} \leq f \leq \frac{B}{2}$. The frequency translates have no overlapping spectral components when $|\alpha| > 2B$.

In [13] and [14], the SCF for analog and digital modulated signals are derived. It is shown that signals with the same power spectral densities may have distinct cyclic

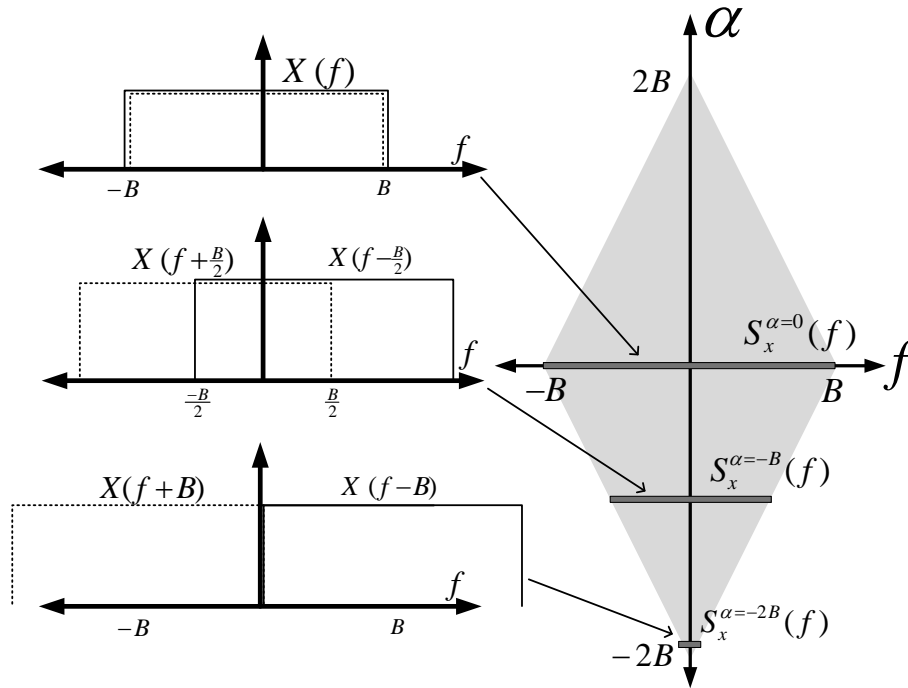


Figure 2.5: SCF Support Region for the Band-limited Signal $x(t)$.

spectrums. Also, the cyclic spectrum is shown to be robust to additive white gaussian noise (AWGN) because stationary noise has no cyclic correlation. Therefore, distinguishing signal features may be extracted from the SCF and can be used for robust classification in varying noise environments. Techniques for estimating the SCF from sampled data are explored in Section 2.4.

2.4 Estimating the Spectral Correlation Function

The theoretical SCF equations presented thus far deal with signals of infinite time duration. In practice, only finite time observations of a signal are available for analysis and, as such, a substantial amount of work has been done to modify the underlying equations to produce efficient, accurate SCF estimates. In general, temporal and frequency smoothing are the two methods used to produce these estimates. Both methods derive from the SCF

cyclic periodogram estimate [9, 10, 25].

$$S_{x_T}^\alpha(t, f) = X_T\left(t, f + \frac{\alpha}{2}\right) X_T^*\left(t, f - \frac{\alpha}{2}\right) \quad (2.36)$$

where

$$X_T(t, f) = \int_{-\infty}^{\infty} a_T(t-u) x(u) e^{-j2\pi fu} du \quad (2.37a)$$

$$= \int_{t-T/2}^{t+T/2} x(u) e^{-j2\pi fu} du \quad (2.37b)$$

is the finite time Fourier transform of $x(t)$ with $a_T(t-u)$, a data tapering window of width T . In the context of Spectral Correlation, $X_T(t, f)$ is commonly referred to in literature as a *complex demodulate*. For statistical reliability, and a reliable estimate, the time-bandwidth product should be much greater than 1 ($\Delta t \times \Delta f \gg 1$) [25]. The cyclic periodogram in Equation (2.36) has a temporal resolution dictated by the data tapering window $a_T(t-u)$ in $X_T(t, f)$ giving $\Delta t = T$. The frequency resolution is also dictated by the data tapering window size, $\Delta f \approx \frac{1}{T} \approx \frac{1}{\Delta t}$. The resulting time-bandwidth product of Equation (2.36) is $\Delta t \Delta f \approx \Delta t \frac{1}{\Delta t} \approx 1$.

Applying time-smoothing to Equation (2.36) gives the time-smoothed cyclic periodogram

$$S_{x_T}^\alpha(t, f)_{\Delta t} = \int_{-\infty}^{\infty} S_{x_T}^\alpha(u, f) \cdot h_{\Delta t}(t-u) du \quad (2.38a)$$

$$= \int_{-\infty}^{\infty} X_T\left(u, f + \frac{\alpha}{2}\right) X_T^*\left(u, f - \frac{\alpha}{2}\right) h_{\Delta t}(t-u) du \quad (2.38b)$$

where the new time resolution is defined by Δt , the width of the sliding data tapering window function $h_{\Delta t}(t-u)$. To maintain statistical reliability, the data tapering window function should have a width $\Delta t \gg \frac{1}{\Delta f} \approx T$ so that the time bandwidth product $\Delta t \times \Delta f \gg 1$. Applying frequency-smoothing to Equation (2.36) gives the frequency-smoothed cyclic

periodogram

$$S_{x_T}^\alpha(t, f)_{\Delta f} = \int_{-\infty}^{\infty} S_{x_T}^\alpha(t, \nu) \cdot h_{\Delta f}(f - \nu) d\nu \quad (2.39a)$$

$$= \int_{-\infty}^{\infty} X_T\left(t, \nu + \frac{\alpha}{2}\right) X_T^*\left(t, \nu - \frac{\alpha}{2}\right) h_{\Delta f}(f - \nu) d\nu \quad (2.39b)$$

where the new frequency resolution is defined by Δf , the bandwidth of the bandpass filter $h_{\Delta f}(f - \nu)$. To maintain statistical reliability, the bandwidth of $h_{\Delta f}(f - \nu)$ should be $\Delta f \gg \frac{1}{\Delta t} = \frac{1}{T}$ so that the time bandwidth product $\Delta t \times \Delta f \gg 1$. It can be shown that both the time-smoothed cyclic periodogram and the frequency-smoothed cyclic periodogram approach perfect estimations of the SCF when the following limits are applied [10, 13]

$$S_x^\alpha(f) = \lim_{T \rightarrow \infty} \lim_{\Delta t \rightarrow \infty} S_{x_T}^\alpha(t, f)_{\Delta t} \quad (2.40a)$$

$$= \lim_{\Delta f \rightarrow 0} \lim_{T \rightarrow \infty} S_{x_T}^\alpha(t, f)_{\Delta f} \quad (2.40b)$$

Both estimates produce a cyclic frequency resolution $\Delta \alpha \approx \frac{1}{\Delta t}$ and it follows that to maintain reliable estimates $\Delta f \gg \frac{1}{\Delta t} \gg \Delta \alpha$. Therefore, the SCF estimate must have finer resolution in cyclic frequency (α) than in spectral frequency (f) to be statistically reliable.

The time smoothing and frequency smoothing methods are generally well suited for different applications of SCF estimation. In general, variants of the time-smoothed cyclic periodogram are well suited for efficient estimation over the entire bi-frequency plane, whereas, variants derived from the frequency-smoothed cyclic periodogram are more suited for estimating the SCF at particular cyclic frequencies [22, 25].

2.4.1 Temporal Smoothing.

All temporal smoothing algorithms for estimating the SCF are derived from the temporally smoothed cyclic periodogram given in Equation (2.38). Incorporating the data

tapering function into the integral and simplifying reduces the equation to

$$\begin{aligned}
S_{x_T}^\alpha(t, f)_{\Delta t} &= \int_{-\infty}^{\infty} S_{x_T}^\alpha(t, f) \cdot h_{\Delta t}(t - u) du \\
&= \int_t^{t+\Delta t} S_{x_T}^\alpha(t, f) du = \frac{1}{T} \int_t^{t+\Delta t} X_T\left(u, f + \frac{\alpha}{2}\right) X_T^*\left(u, f - \frac{\alpha}{2}\right) du \\
&= \frac{1}{T} \left\langle X_T\left(t, f + \frac{\alpha}{2}\right) X_T^*\left(t, f - \frac{\alpha}{2}\right) \right\rangle_{\Delta t} \tag{2.41}
\end{aligned}$$

where the complex demodulate, $X_T(t, f)$, is defined as in Equation (2.37). In [25] and [22], Equation (2.38) was extended to discrete, sampled time-series.

$$S_{X_T}^{\alpha_0}[n, f_0]_{\Delta t} = \sum_{r=n}^{n+N} X_T[r, f_k] X_T^*[r, f_l] h_{\Delta t}[n - r] \tag{2.42}$$

where $\alpha_0 = f_k - f_l$, $f_0 = \frac{f_k + f_l}{2}$, r is a dummy variable, and $X_T[r, f_k]$ is the discrete version of Equation (2.37) given by

$$X_T[r, f_k] = \sum_{m=0}^{N'-1} a_T[m] x[r + m] e^{-j2\pi f_k(r+m)T_s} \tag{2.43a}$$

$$= \sum_{m=0}^{N'-1} a_T[m] x[r + m] e^{-j2\pi k(r+m)/N'} \tag{2.43b}$$

where $x[n] = x(t)|_{t=nT_s}$, $T_s = \frac{1}{2B}$, $f_k = \frac{k}{N'T_s}$, and $T = N'T_s$. The temporal resolution $\Delta t = NT_s$ and the frequency resolution $\Delta f = \frac{1}{N'T_s}$ which produces a time bandwidth product $\Delta t \Delta f = \frac{N}{N'}$ and cyclic frequency resolution $\Delta \alpha \approx \frac{1}{\Delta t} = \frac{1}{N'T_s}$. For statistical reliability $N \gg N'$ and $\Delta \alpha \ll \Delta f$ [25].

Equation (2.41), Equation (2.42), and Figure 2.6 show that the time smoothed cyclic cross periodogram is basically a correlation between the spectral components of $x[n]$ over the time observation of Δt . The time smoothing is done by allowing a data tapering window of length T time to slide over the total signal observation Δt time or equivalently a data tapering window of length N' samples to slides over the total data samples of length N . Again, the window of size N' samples or T time should be much smaller than the total observation length of N samples or Δt time for statistically accurate estimates [22, 25].

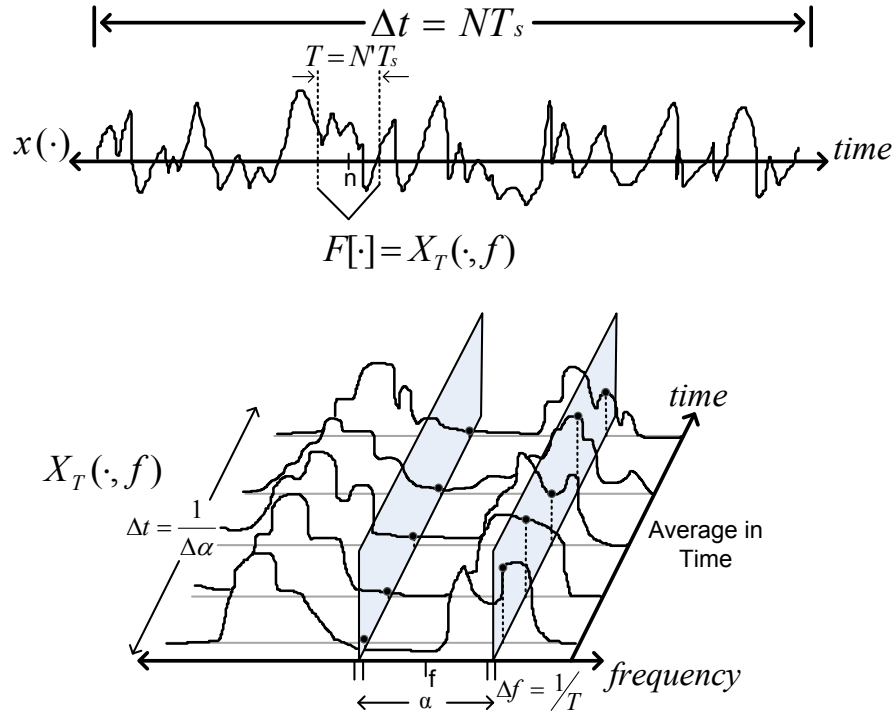


Figure 2.6: Temporal Smoothing [25]

Since this method is deemed computationally inefficient, ways to improve the computational efficiency of the time-smoothed spectral estimates were explored in [25]. One method to improve the computational efficiency is to decimate Equation (2.43) by L , where $L < N'$, giving $X_T[rL, f_k]$. This reduces the number of correlations in Equation (2.42) by a factor of L from N to $P = \frac{N}{L}$. Equivalently, instead of calculating Equation (2.43) N times, then decimating to P values, a system can simply calculate the P values of $X_T[rL, f_k]$ by shifting $x[n]$ by L samples each computation. A decimation factor of $L = \frac{N'}{4}$ has been shown to be a good choice to increase computational efficiency and minimize adverse effects from cycle leakage and cycle aliasing [4]. The time smoothing with decimation cyclic periodogram is [25]

$$S_{X_T}^{\alpha_0}[nL, f_0]_{\Delta t} = \sum_{r=n}^{n+P} X_T[rL, f_k] X_T^*[rL, f_i] h_{\Delta t}[n-r] \quad (2.44)$$

where

$$X_T [rL, f_k] = \sum_{m=0}^{N'-1} a_T [m] x [rL + m] e^{-j2\pi k(rL+m)/N'} \quad (2.45)$$

Another method to improve the cyclic spectral estimates computational efficiency is to multiply both sides of Equation (2.42) with the sinusoidal factor $e^{-j2\pi qm/N}$. This shifts the left side in cyclic frequency by $\frac{q}{N} = q\Delta\alpha$ where $q = [0, 1, \dots, N-1]$ and fits the right side into the form of an N -point fast fourier transform (FFT) [25].

$$S_{X_T}^\alpha [n, f_0]_{\Delta t} \left(e^{-j2\pi qm/N} \right) = \sum_{r=0}^N X_T [r, f_k] X_T^* [r, f_l] h_{\Delta t} [n-r] \left(e^{-j2\pi qr/N} \right) \quad (2.46a)$$

$$S_{X_T}^{\alpha_1+q\Delta\alpha} [n, f_0]_{\Delta t} = \mathcal{F} [X_T [r, f_l] X_T^* [r, f_k] \star h_{\Delta t} [r]]_N \quad (2.46b)$$

$$= \mathcal{F} [X_T [r, f_l] X_T^* [r, f_k]]_N \mathcal{F} [h_{\Delta t} [r]]_N \quad (2.46c)$$

where \star denotes a convolution, the notation $\mathcal{F} [\cdot]_N$ denotes an N -point DFT, $X_T [r, f_k]$ is computed as in Equation (2.43), $f_0 = \frac{f_k+f_l}{2} = \frac{k+l}{2} \left(\frac{f_s}{N'} \right)$, and $\alpha_0 = f_k - f_l = (l-k) \left(\frac{f_s}{N'} \right)$. Utilizing the concepts above, [25] presents the FFT accumulation method (FAM) and strip spectral correlation algorithm (SSCA) as computationally efficient time smoothing algorithms to estimate the cyclic spectrum.

2.4.1.1 FFT Accumulation Method.

The FAM applies both decimation and FFTs to Equation (2.42), resulting in

$$S_{X_T}^{\alpha_i+q\Delta\alpha} [nL, f_0]_{\Delta t} = \sum_{r=0}^{P-1} X_T [rL, f_k] X_T^* [rL, f_l] h_{\Delta t} [n-r] e^{-j2\pi qr/P} \quad (2.47a)$$

$$= \sum_{r=0}^{\frac{N}{L}-1} X_T [rL, f_k] X_T^* [rL, f_l] h_{\Delta t} [n-r] e^{-j2\pi qrL/N} \quad (2.47b)$$

$$= \mathcal{F} [X_T [rL, f_k] X_T^* [rL, f_l]]_P \mathcal{F} [h_{\Delta t} [r]]_P \quad (2.47c)$$

where $X_T [rL, f_k]$ is defined as in Equation (2.45), $\alpha_0 = \alpha_i + q\Delta\alpha$, L is the decimation factor, and $P = \frac{N}{L}$. The time and frequency resolutions are $\Delta\alpha = \frac{f_s}{PL} = \frac{f_s}{N}$, $\Delta t = \frac{1}{\Delta\alpha} = \frac{N}{f_s}$, and $\Delta f [q] = \Delta a - |q| \Delta\alpha$. Since $\Delta a = \frac{f_s}{N'}$, $\Delta f [q]$ can be reduced to $\left(1 - |q| \frac{N'}{PL} \right) \frac{f_s}{N'}$. Therefore, the time-bandwidth product is $\Delta t \Delta f = \Delta t (\Delta a - |q| \Delta\alpha) = \frac{N}{N'} - |q|$.

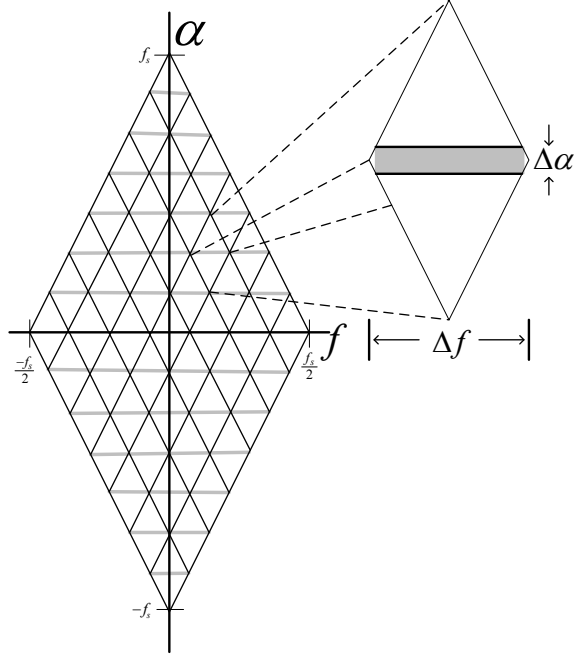


Figure 2.7: FAM Estimate Resolution [22, 25]

Figure 2.7 shows the support region for the FAM. To minimize the point estimates near the top and bottom of the channel-pair regions, where q is large and the time bandwidth product is reduced resulting in less reliable estimates, only the estimates within the region center $\pm\Delta a/2$ are retained. This leaves only the terms corresponding to

$$\begin{aligned} -\frac{\Delta a}{2} &\leq q\Delta\alpha \leq \frac{\Delta a}{2} \\ -\frac{N}{2N'} &\leq q \leq \frac{N}{2N'} - 1 \\ -\frac{PL}{2N'} &\leq q \leq \frac{PL}{2N'} - 1 \end{aligned}$$

Therefore, there are missing estimates for some cyclic frequencies, α , where the estimates are less reliable. These missing estimates may contain important cyclic features and therefore, the FAM is not advised when location of cyclic features is unknown *a priori*.

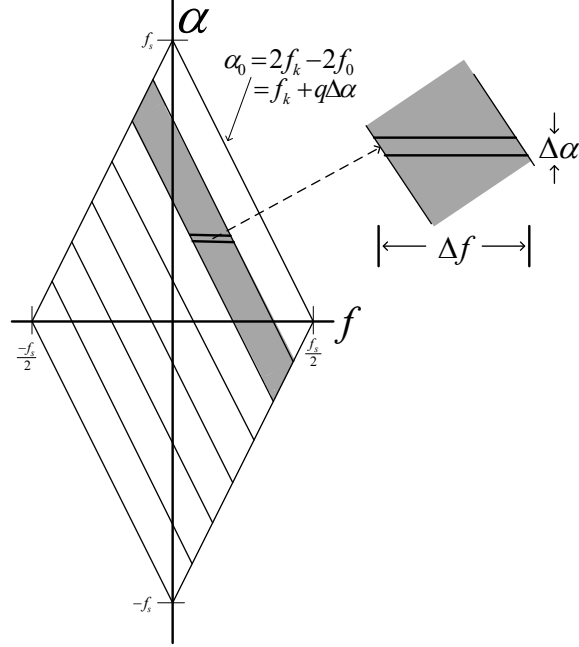


Figure 2.8: SSCA Estimate Resolution [22, 25]

2.4.1.2 Strip Spectral Correlation Algorithm.

The second temporally-smoothed cyclic spectral estimation algorithm is the SSCA, which allows estimates of all cyclic frequencies. In this algorithm, the complex demodulates $X_T[n, f_k]$ directly multiply with $x^*(n)$, which produces estimates along the frequency-skewed line $\alpha = 2f_k - 2f_0$. This algorithm has been shown to give highly efficient estimates of the SCF over the entire bi-frequency plane, but sacrifices fine frequency resolution [25]. The SSCA is given by

$$S_{X_T}^{f_k + q\Delta\alpha} \left[n, \frac{f_k}{2} - q\frac{\Delta\alpha}{2} \right]_{\Delta t} = \sum_{r=0}^N X_T[r, f_k] x^*[r] h_{\Delta t}[n-r] e^{-j2\pi qr/N} \quad (2.48a)$$

$$= \mathcal{F} [X_T[r, f_k] x^*[r]]_N \mathcal{F} [h_{\Delta t}[r]]_N \quad (2.48b)$$

where $\alpha_0 = f_k + q\Delta\alpha$ and $f_0 = \frac{f_k}{2} - \frac{q\Delta\alpha}{2}$. The temporal and frequency resolutions are $\Delta t = \frac{N}{f_s}$, $\Delta f = \frac{1}{T} = \frac{f_s}{N}$, and $\Delta\alpha \approx \frac{1}{\Delta t} = \frac{f_s}{N}$ making the time-bandwidth product $\Delta t \Delta f = \frac{N}{N'}$. Like the FAM algorithm, let $N \gg N'$ to produce reliable estimates.

2.4.2 Frequency Smoothing.

The frequency-smoothed cyclic periodogram equation was given in Equation (2.39). In [4] and [22], Equation (2.39) was extended to discrete sampled time-series.

$$S_{X_T}^{\alpha_0}[n, f_0]_{\Delta f} = \sum_{r=-\frac{N'}{2}}^{\frac{N'}{2}-1} X_T \left[n, f_k + \frac{r}{T} \right] X_T^* \left[n, f_l + \frac{r}{T} \right] h_{\Delta f}[r] \quad (2.49)$$

where $\alpha_0 = f_k - f_l$, $f_0 = \frac{f_k + f_l}{2}$, $h_{\Delta f}[r]$ represents the response of some bandpass filter with bandwidth Δf , and the complex demodulate

$$X_T[n, f_k] = \sum_{m=0}^{N-1} a_T[m] x[n+m] e^{-j2\pi f_k(n+m)T_s} \quad (2.50)$$

is now calculated from N samples instead of N' samples. Figure 2.9 gives a graphical representation of Equation (2.49). The temporal and frequency resolutions for the frequency-smoothed SCF are $\Delta f = \frac{N'}{T} = \frac{N'}{NT_s}$, $\Delta t = T = NT_s$, and $\Delta\alpha \approx \frac{1}{\Delta t}$. The time-bandwidth product is then, $\Delta t \Delta f = N'$ and we let $N' \gg 1$ for statistical reliability. It is apparent from Equation (2.49) that there is a trade-off between statistical reliability and spectral resolution [25]. To achieve highly reliable SCF estimates, a large amount of frequency smoothing is desired, but if the spectrum has narrow spectral features, the amount of spectral smoothing should be minimized [25].

2.5 Cyclic Cumulants

Statistics are used to describe and characterize the behavior of processes. Specifically, the moments and cumulants of processes are very useful for describing behavior. Since cumulant functions generally can not be computed from experimental time-series data, they are usually estimated from knowledge of moment functions, which can be computed from experimental data [3]. Temporal and spectral cumulants are shown theoretically to exhibit the property of signal selectivity in [16]. This is the ability to detect or estimate parameters of a specific signal in a received waveform even when corrupted by noise or

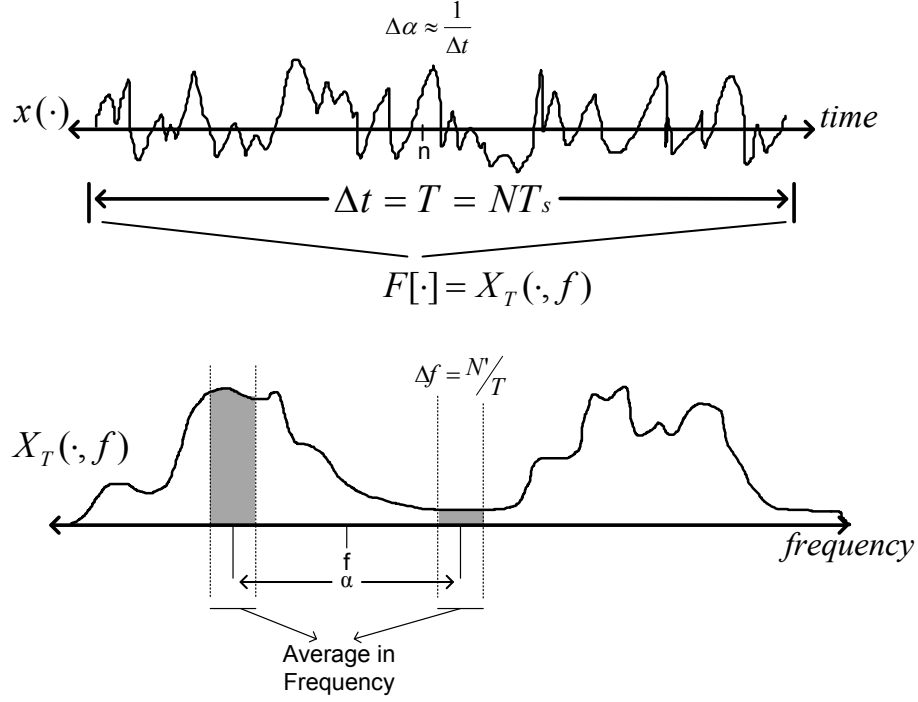


Figure 2.9: Frequency Smoothing

interference. This property was verified through simulations in [27]. The temporal moment function (TMF) for zero time-lag is [3]

$$R_x(t, \tau = 0)_{n,q} \triangleq E [x(t)^{n-q} (x^*(t))^q] \quad (2.51)$$

and is used to compute n -order, q -conjugate moments. It is apparent that the autocorrelation defined in Equation (2.27b) is a specific case of the TMF with $n = 2$ and $q = 1$ so $R_x(t, \tau)_{2,1} = E [x(t) x^*(t)]$. Using the moments, cumulants are calculated through the moment to cumulant formula, also known as the temporal cumulant function (TCF) [16, 17]

$$C_x(t, \tau)_{n,q} = \sum_{P_n} \left[(-1)^{p-1} (p-1)! \prod_{j=1}^p R_x(t, \tau)_{n_j, q_j} \right] \quad (2.52)$$

where P_n are all distinct partitions of the set $[1, 2, \dots, n]$, p is the number of elements in each partition, and $R_x(t, \tau)_{n_j, q_j}$ is the n -order, q -conjugate moment corresponding to the j th element in the partition [16]. It has been shown that the cyclic cumulants attain maximum

Table 2.4: $n=4$, $q=2$ cumulant partitions where $(\cdot)^*$ denotes a conjugate and ‘1’ and ‘2’ were generically chosen as the two conjugated terms.

p	$n=4, q=2$ Partitions P_n	$C_x(t)_{4,2}$ Partitions $(-1)^{p-1} (p-1)! \prod_{j=1}^p R_x(t, \mathbf{0})_{n_j, q_j}$
1	$(1^*, 2^*, 3, 4)$	$R_x(t)_{4,2}$
2	$(1^*, 2^*) (3, 4)$	$-R_x(t)_{2,2} R_x(t)_{2,0}$
2	$(1^*, 3) (2^*, 4)$	$-R_x(t)_{2,1}^2$
2	$(1^*, 4) (2^*, 3)$	$-R_x(t)_{2,1}^2$
2	$(1^*, 2^*, 3) (4)$	$-R_x(t)_{3,2} R_x(t)_{1,0}$
2	$(1^*, 2^*, 4) (3)$	$-R_x(t)_{3,2} R_x(t)_{1,0}$
2	$(1^*, 3, 4) (2^*)$	$-R_x(t)_{3,1} R_x(t)_{1,1}$
2	$(2^*, 3, 4) (1^*)$	$-R_x(t)_{3,1} R_x(t)_{1,1}$
3	$(1^*, 2^*) (3) (4)$	$2R_x(t)_{2,2} R_x(t)_{1,0}^2$
3	$(1^*, 3) (2^*) (4)$	$2R_x(t)_{2,1} R_x(t)_{1,1} R_x(t)_{1,0}$
3	$(1^*, 4) (2^*) (3)$	$2R_x(t)_{2,1} R_x(t)_{1,1} R_x(t)_{1,0}$
3	$(2^*, 3) (1^*) (4)$	$2R_x(t)_{2,1} R_x(t)_{1,1} R_x(t)_{1,0}$
3	$(2^*, 4) (1^*) (3)$	$2R_x(t)_{2,1} R_x(t)_{1,1} R_x(t)_{1,0}$
3	$(3, 4) (1^*) (2^*)$	$2R_x(t)_{2,0} R_x(t)_{1,1}^2$
4	$(1^*) (2^*) (3) (4)$	$-6R_x(t)_{1,1}^2 R_x(t)_{1,0}^2$

values for zero delay values, $\tau = 0$ [6]. Therefore, all n -order moments and cumulants in this research are calculated for $\tau = 0$ and τ will be omitted from the notation. For example, $C_x(t, \tau)_{4,2}$ will be expressed as $C_x(t)_{4,2}$. In Table 2.4 an example for calculating the terms for $C_x(t)_{4,2}$ from Equation (2.52) is shown. There are 15 distinct partitions of the set $[1^*, 2^*, 3, 4]$ where there are $n = 4$ items and $q = 2$ are conjugated. Item ‘1’ and item ‘2’ in the set were generically chosen as the two conjugated terms, but any combination of two may be chosen as long as the selections are maintained throughout the derivation. Summing the $C_x(t)_{4,2}$ partition terms in Table 2.4 gives Equation (2.53).

$$\begin{aligned}
C_x(t)_{4,2} = & R_x(t)_{4,2} - |R_x(t)_{2,0}|^2 - 2R_x(t)_{2,1}^2 - 2R_x(t)_{3,2} R_x(t)_{1,0} - 2R_x(t)_{3,1} R_x(t)_{1,1} \\
& + 2R_x(t)_{2,2} R_x(t)_{1,0}^2 + 8R_x(t)_{2,1} |R_x(t)_{1,0}|^2 + R_x(t)_{2,0} R_x(t)_{1,1}^2 - 6 |R_x(t)_{1,0}|^4 \quad (2.53)
\end{aligned}$$

Table 2.5: Cumulants

$C_{n,q}$	Equation
$C_{2,0}$	$R_{2,0}$
$C_{2,1}$	$R_{2,1}$
$C_{4,0}$	$R_{4,0} - 3C_{2,0}^2$
$C_{4,1}$	$R_{4,1} - 3C_{2,0}C_{2,1}$
$C_{4,2}$	$R_{4,2} - C_{2,0} ^2 - 2C_{2,1}^2$
$C_{6,0}$	$R_{6,0} - 15C_{2,0}C_{4,0} - 15C_{2,0}^3$
$C_{6,1}$	$R_{6,1} - 10C_{2,0}C_{4,1} - 5C_{2,1}C_{4,0} - 15C_{2,1}C_{2,0}^2$
$C_{6,2}$	$R_{6,2} - C_{2,0}^*C_{4,0} - 8C_{2,1}C_{4,1} - 6C_{2,0}C_{4,2} - 3C_{2,0}^*C_{2,0}^2 - 12C_{2,0}C_{2,1}^2$
$C_{6,3}$	$R_{6,3} - 3C_{2,0}^*C_{4,1} - 9C_{2,1}C_{4,2} - 3C_{2,0}C_{4,1}^* - 9C_{2,0}^*C_{2,1}C_{2,0} - 6C_{2,1}^3$
$C_{8,0}$	$R_{8,0} - 28C_{2,0}C_{6,0} - 35C_{4,0}^2 - 210C_{2,0}^2 - 105C_{2,0}^4$

The cumulant equation is greatly simplified when central moments are used instead of raw moments, or the process is known to be a zero mean process, $\mu_x = R_x(t, 0)_{1,0} = R_x(t, 0)_{1,1} = 0$. In practical situations, a signal can be made a zero mean process by subtracting the mean from it. $C_x(t, 0)_{4,2}$ reduces to

$$C_x(t)_{4,2} = R_x(t)_{4,2} - |R_x(t)_{2,0}|^2 - 2R_x(t)_{2,1}^2. \quad (2.54)$$

A list of the zero-mean cumulant equations derived from Equation (2.52) as functions of lower order moments and cumulants are shown in Table 2.5. Owing to the symmetrical signal constellations considered, the n th-order moments for n odd are zero and therefore, the n th-order cumulants for n odd are also zero and have been dropped from the cumulant equations in Table 2.5 [5].

Much like the CAF is found by Fourier transforming the autocorrelation function, the cyclic temporal cumulant function (CTCF) is produced by Fourier transforming the TCF [16]

$$C_x^\beta(t, 0)_{n,q} = \int_{-\infty}^{\infty} C_x(t, 0)_{n,q} e^{-j2\pi\beta t} dt \quad (2.55)$$

which gives the TCF's frequency components at frequency β . The n th-order, q -conjugate cycle frequencies (CFs) of interest are at $\beta = (n - 2q) f_c$ [6]. Since AWGN is a stationary,

zero-mean Gaussian process, its cumulants are time independent and non-zero only for the second order. Therefore, AWGN does not have any contribution to the higher-order ($n \geq 3$) cyclic cumulants (CCs) of a received signal $r(t)$. Last, the magnitude of the n th-order, q -conjugate CC is robust to the carrier phase and timing offsets [5, 6].

III. Methodology

THIS chapter outlines the work that led to the development of a modulation recognition system. The modulation recognition system is feature-based and designed to discriminate between BPSK, QPSK, 16-QAM, 64-QAM, 8-PSK, 16-PSK, Barker₅, Barker₁₁, Barker₅₅, Frank₄₉, P_X₄₉, and LFM modulations using features derived from theory in *Chapter II*. All simulations were done in discrete-time with matrix laboratory (MATLAB[®]), therefore all equations will be presented for discrete-time.

Section 3.1 describes the process used to simulate the waveforms and Section 3.2 describes the process of introducing AWGN to the waveforms to simulate received SNR. Section 3.3 highlights how the features were estimated, Section 3.4 explains the classifier supervised training process, and Section 3.5 gives the metrics used to assess the classifier performance.

3.1 Simulating Modulations

This section describes the process used to simulate the waveforms being considered in this research. The process used to simulate the waveforms in MATLAB[®] is shown in Figure 3.1.

Equation (3.1) is the discrete version of Equation (2.4) and is used to simulate the discrete symbols for BPSK, QPSK, 8-PSK, and 16-PSK

$$\text{BPSK : } s_m[n] = A \cos(2\pi f_c n T_s + \pi(m-1)) \quad m = 1, 2 \quad (3.1a)$$

$$\text{QPSK : } s_m[n] = A \cos\left(2\pi f_c n T_s + \frac{\pi}{2}(m-1)\right) \quad m = 1, 2, 3, 4 \quad (3.1b)$$

$$\text{8-PSK : } s_m[n] = A \cos\left(2\pi f_c n T_s + \frac{\pi}{4}(m-1)\right) \quad m = 1, 2, \dots, 8 \quad (3.1c)$$

$$\text{16-PSK : } s_m[n] = A \cos\left(2\pi f_c n T_s + \frac{\pi}{8}(m-1)\right) \quad m = 1, 2, \dots, 16 \quad (3.1d)$$

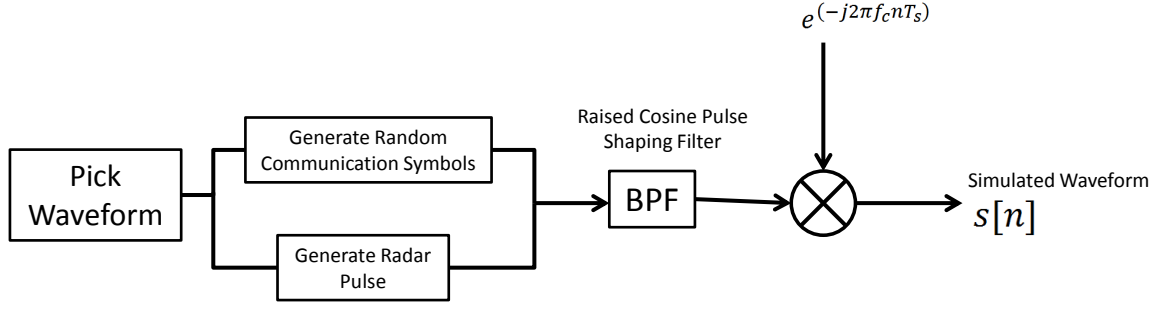


Figure 3.1: Waveform Simulation Process

where each symbol is defined on the discrete interval $0 \leq nT_s \leq T_{sym}$, T_{sym} is the symbol period, and T_s is the discrete sampling period related to sampling frequency by $f_s = \frac{1}{T_s}$. Equation (3.2) is the discrete form of Equation (2.6) and is used to generate the 16-QAM and 64-QAM symbols

$$\text{M-QAM} : s_m[n] = A_m \phi_1(nT_s) + B_m \phi_2(nT_s) \quad (3.2)$$

$$0 \leq nT_s \leq T_{sym} \quad m = 1, 2, \dots, M$$

where $\phi_1(t) = \cos(2\pi f_c n T_s)$, $\phi_2(t) = \sin(2\pi f_c n T_s)$, A_m and B_m are defined as $A_m = (2a_m - 1) - \sqrt{M}$ and $B_m = (2b_m - 1) - \sqrt{M}$ with a_m and b_m all combinations of integers in the set $[1, 2, \dots, \sqrt{M}]$. For 16-QAM, A_m and B_m may have values $[-3, -1, 1, 3]$ and for 64-QAM, A_m and B_m may have values $[-7, -5, -3, -1, 1, 3, 5, 7]$.

Since the information symbols in communication waveforms can be modeled as random, each generated communication symbol is uniformly randomly selected. This process was simulated by using the MATLAB[®] command 'randi' which uniformly randomly selects a value from a given set. The resulting communication waveform, $s[n]$, consists of a stream of random symbols $s_m[n]$. This produces pseudo random streams of each modulation where all symbols are equally likely to occur every symbol period. Also, the signal's modulated and transmitted information bandwidth is $W = 2B = \frac{2}{T_{sym}}$.

Equation (3.3) is used for simulating an up-chirp pulse with bandwidth, B centered at carrier frequency f_c with duration τ .

$$\text{LFM} : s[n] = \text{Rect}\left(\frac{nT_s}{\tau}\right) \cos\left(2\pi nT_s \left(f_c + \frac{W}{2\tau}nT_s\right)\right), \quad 0 \leq nT_s \leq \tau \quad (3.3)$$

Equation (3.4) is used to simulate Barker₅, Barker₁₁, and Barker_{5,11} codes. Barker₅ and Barker₁₁ use the codes given in Table 2.1 corresponding to length 5 and 11 respectively, but Barker_{5,11} uses the code generated by ‘nesting’ the length 5 code within a length 11 code sequence similar to the Barker_{4,5} example in Figure 2.3.

$$\text{Barker} : s_m[n] = \text{Rect}\left(\frac{nT_s}{\tau}\right) \cos(2\pi f_c nT_s + c_m \pi), \quad mT_{sym} \leq nT_s \leq (m+1)T_{sym} \quad (3.4)$$

Equation (3.5) is the discrete equation for Frank and Px coded radar pulses with the phases defined as in Equation (2.19).

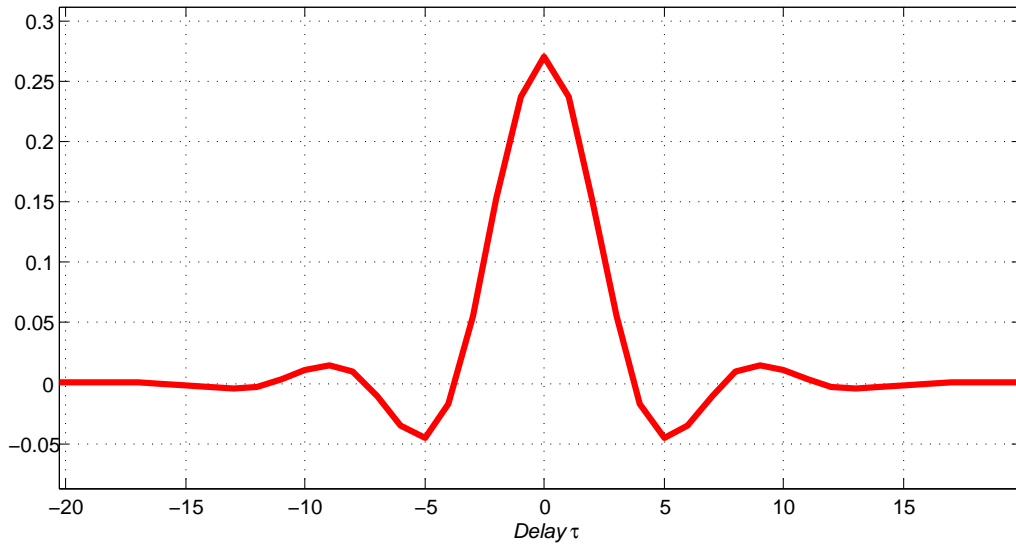
$$s_{(l_1-1)L+l_2}[n] = \cos(2\pi f_c nT_s + \phi_{l_1, l_2}) \quad (3.5)$$

The radar pulse compression modulations are considered deterministic not random. Their value during a symbol period is predetermined by the specific code sequence corresponding to the pulse compression format/type.

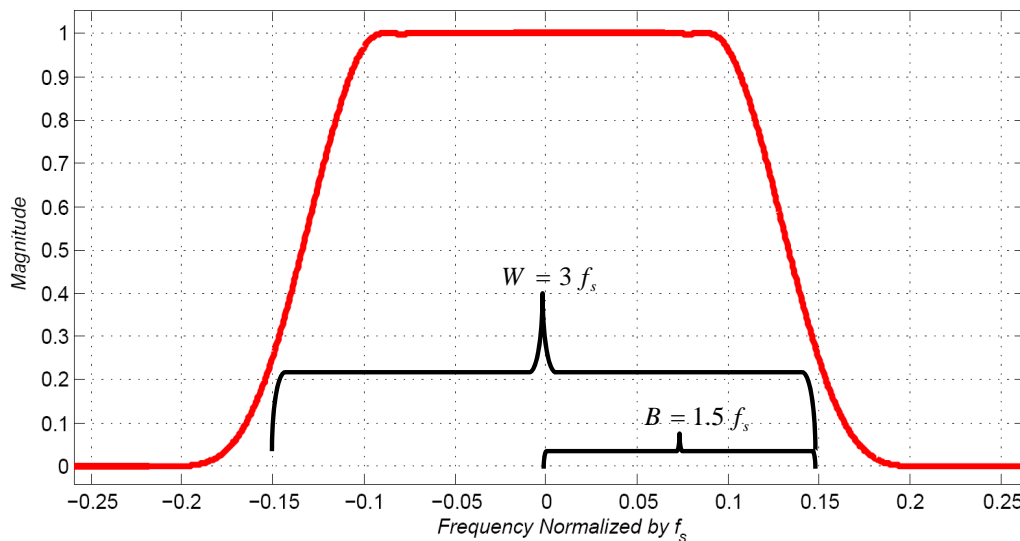
After the waveform symbols are generated, they are filtered using a raised cosine pulse shaping filter in MATLAB[®] with 50% excess bandwidth and a roll-off factor $\beta = 0.4$. This filter was used to simulate the pulse shaping filter in a transmitter and to band-limit the transmitted simulated waveform. The impulse response of a raised cosine filter is given by

$$h[n] = \text{sinc}\left(\frac{nT_s}{T_{sym}}\right) \frac{\cos\left(\frac{\pi\beta nT_s}{T_{sym}}\right)}{1 - \left(\frac{2\beta nT_s}{T_{sym}}\right)^2} \quad (3.6)$$

This raised cosine filter was generated in MATLAB[®] using the ‘firrcos’ command with the options: filter order = 10, cutoff frequency = $1.5 \times B$ where $B = f_{sym} = \frac{1}{T_{sym}}$, and roll-off factor $\beta = 0.4$. It is applied to the simulated modulations using the MATLAB[®] ‘filtfilt’



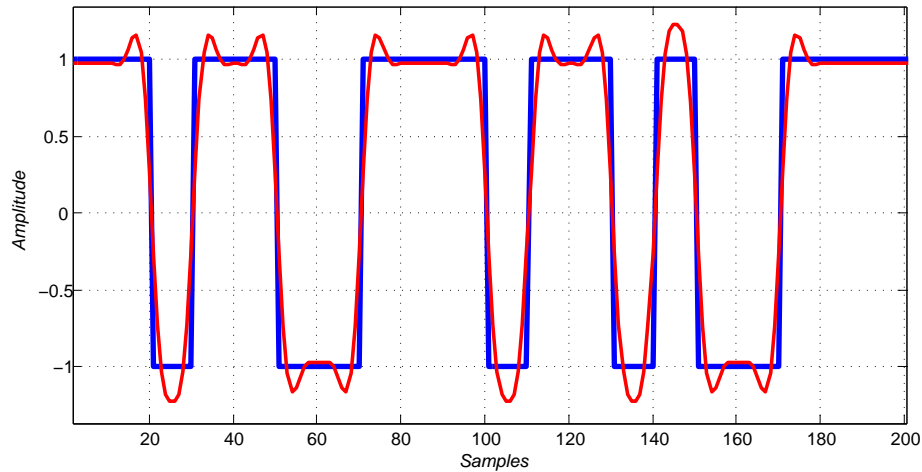
(a) Impulse Response of Pulse Shaping Filter Used



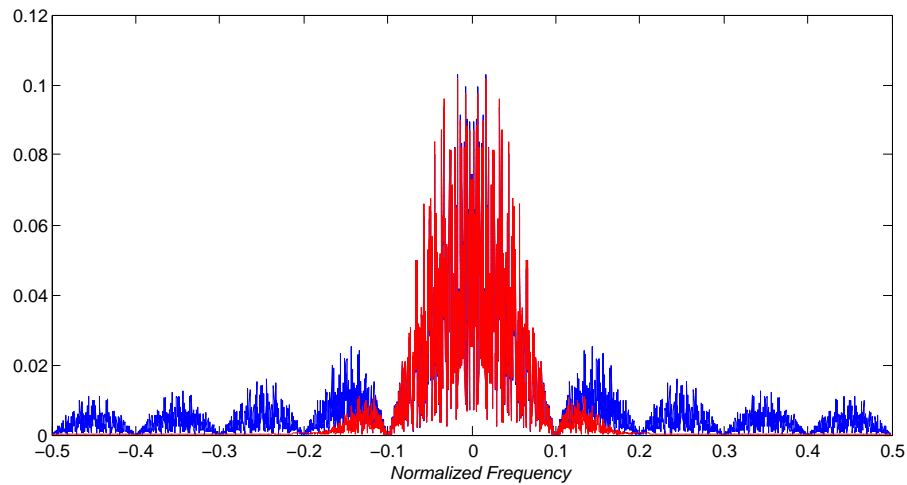
(b) Frequency Response of Pulse Shaping Filter

Figure 3.2: Pulse shaping filter properties using MATLAB[®] ‘firrcos’ command with order = 10, cutoff frequency = $0.15f_s$, and roll-off factor $\beta = 0.4$ applied with the ‘filtfilt’ command .

command which effectively squares the filter response by applying the filter twice to negate phase distortion. Thus, the pulse shaping filter used in this research is $|h[n]|^2$. The impulse and frequency response for this MATLAB[®] generated pulse shaping filter with $B = 0.1f_s$,



(a) Temporal representation of BPSK filtered by pulse shaping filter. (Red - Filtered, Blue - Unfiltered)



(b) Frequency representation of BPSK filtered by pulse shaping filter (Red - Filtered, Blue - Unfiltered)

Figure 3.3: MATLAB[®] generated pulse shaping filter from Figure 3.2 applied to simulated BPSK Signal with $B = \frac{1}{T_{Sym}} = 0.1 f_s$.

applied with the ‘filtfilt’ command, is shown in Figure 3.2. In this research, bandwidth is referred to as both B and W , where B is the baseband bandwidth and $W = 2B$ is the transmission bandwidth.

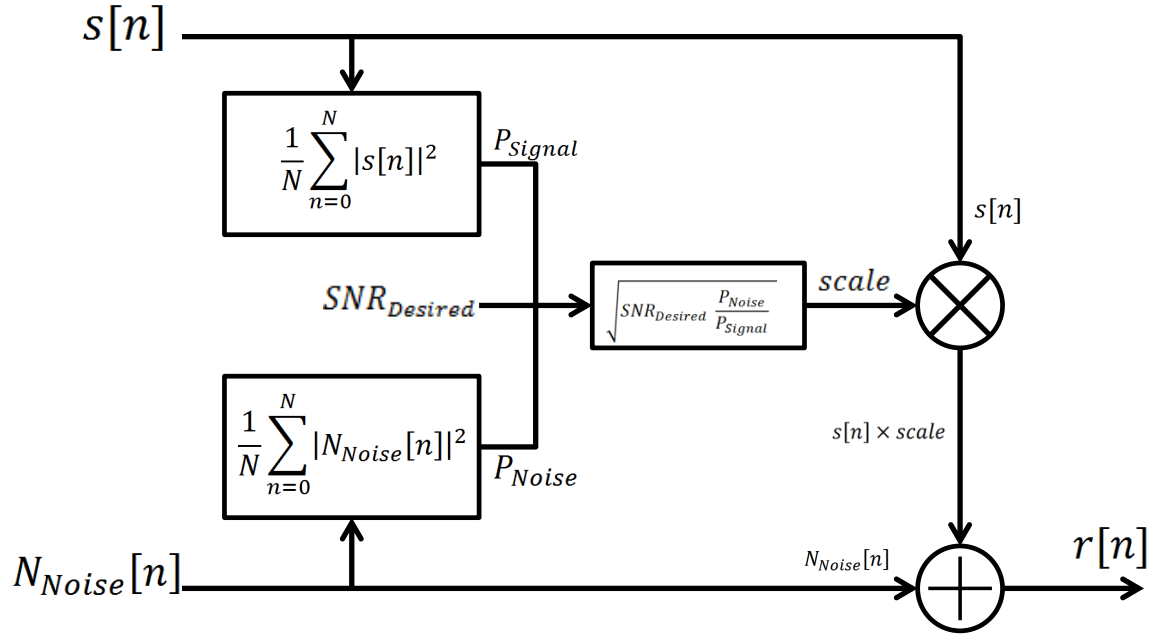


Figure 3.4: Simulated SNR Scaling Process

Furthermore, the temporal and frequency responses from passing a BPSK signal with $W = 2B = 2f_s$ through the pulse shaping filter shown in Figure 3.2 is shown in Figure 3.3. After pulse shaping, the signal is then mixed up to a carrier frequency f_c by multiplying the baseband signal by $e^{(j2\pi f_c nT_s)}$.

3.2 Simulating SNR with AWGN

After a waveform is simulated, filtered, and upconverted to a carrier frequency for transmission, channel effects are simulated by introducing randomly generated AWGN to simulate a specific SNR. The SNR is simulated through the process shown in Figure 3.4.

First complex AWGN, $N_{Noise}[n]$, is simulated. AWGN has a normal Gaussian distribution. This was realized in MATLAB[®] by generating streams of random real and complex values using the ‘randn’ command. The simulated waveform’s power and the

simulated AWGN's power is computed using Equation (3.7)

$$P_{avg} = \frac{1}{N} \sum_{m=0}^N |(\cdot)|^2 = \langle |(\cdot)|^2 \rangle_n = MEAN[|(\cdot)|^2] \quad (3.7)$$

and the ratio of signal power, P_{Signal} , and the noise power, P_{Noise} , is the SNR.

$$SNR = \frac{P_{Signal}}{P_{Noise}} = \frac{P_{s[n]}}{P_{N_{Noise}[n]}} \quad (3.8)$$

To achieve a desired SNR, the simulated waveform, $s[n]$, is scaled by a constant scale factor, $scale$, found through the relationship

$$SNR_{Desired} = \frac{P_{SignalDesired}}{P_{Noise}} \quad (3.9a)$$

$$= \frac{P_{s[n] \times scale}}{P_{N_{Noise}[n]}} \quad (3.9b)$$

$$= \frac{\langle |s[n] \times scale|^2 \rangle_n}{\langle |N_{Noise}[n]|^2 \rangle_n} \quad (3.9c)$$

$$= \frac{P_{s[n]}}{P_{N_{Noise}[n]}} \times (scale)^2 \quad (3.9d)$$

Rearranging and solving for $scale$ in the above equation gives

$$scale = \sqrt{SNR_{Desired} \frac{P_{Noise}}{P_{Signal}}} \quad (3.10)$$

so that multiplying $s[n]$ by the scale factor gives us the desired SNR.

Therefore, the simulated received signal $r[n]$ with a specific SNR is produced by multiplying the signal ($s[n]$) by the calculated scale factor from Equation (3.10) and adding this product to the simulated noise, $N_{Noise}[n]$.

$$r[n] = s[n] \times scale + N_{Noise}[n] \quad (3.11)$$

The desired SNRs in this work are expressed in a logarithmic decibel scale. To convert between linear and decibel scales utilize Equation (3.12)

$$SNR_{dB} = 10 \log_{10} (SNR) \quad (3.12a)$$

$$SNR = 10^{\frac{SNR_{dB}}{10}} \quad (3.12b)$$

3.3 Extracting Features

Once the received signal was simulated, feature analysis was done to extract useful features for use in classification. The following subsections describe the features extracted from the simulated, received waveforms.

3.3.1 Duty Cycle.

An estimated version of duty cycle, $\hat{\delta}_c$ is used to determine whether the received signal is present during the whole observation period or is a pulse. To do this, $|r[n]|^2$ is smoothed with a moving average filter to produce

$$|r[n]|_{smoothed}^2 = \frac{1}{N_{SF}} \sum_{m=n}^{n+N_{SF}-1} |r[m]|^2 \quad (3.13)$$

where N_{SF} is the smoothing factor and represents the number of samples averaged for each smoothed value. This research uses $N_{SF} = 4 \times \frac{T_{Sym}}{T_s}$ arbitrarily chosen based on simulation results. $\hat{\delta}_c$ is estimated with Equation (2.12) where an estimated P_0 is used instead of Equation (2.13b) and P_{avg} is the average power in the observed time interval Δt . \hat{P}_0 was chosen to be estimated as

$$\hat{P}_0 = \max_n [p[n]_{smoothed}] = \max_n [|r[n]|_{smoothed}^2], \quad 0 \leq nt_s \leq \Delta t \quad (3.14)$$

When the transmit pulse duration τ is not known, $\hat{\delta}_c$ provides estimated duty cycles that are statistically different for pulsed and continuous waveforms as shown in Figure 3.5 . Therefore, $\hat{\delta}_c$ is calculated as ratio between the average power in an observed time interval and the estimated \hat{P}_0 from Equation (3.14)

$$\hat{\delta}_c = \frac{P_{avg}}{\hat{P}_0}. \quad (3.15)$$

The received waveform's estimated duty cycles are shown in Figure 3.6 for various SNRs. The range bars show the 95% confidence interval for the estimated duty cycle at each SNR_{dB} based on 3,000 simulated observations per waveform per SNR. It can be seen that the estimated duty cycle is affected by noise and all the waveforms tend to have statistically

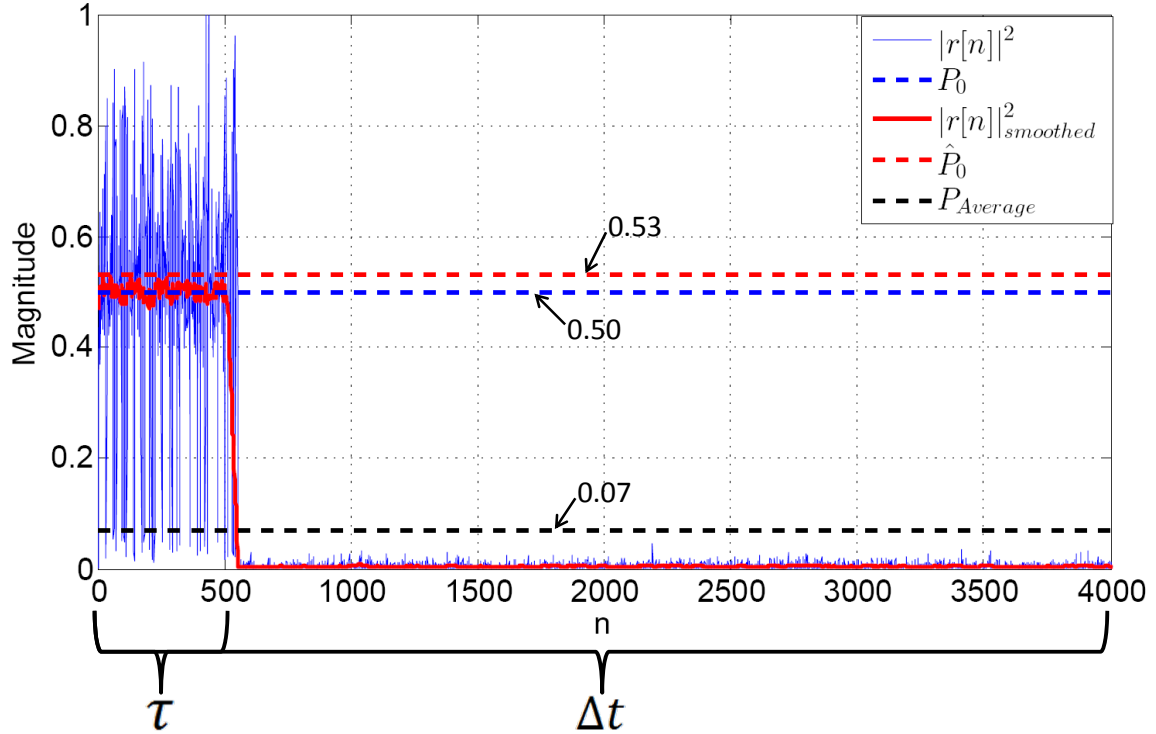


Figure 3.5: Estimating the duty cycle of an arbitrary pulse with $\text{SNR} = 20$ dB over an observation time Δt by using \hat{P}_0 instead of P_0 when τ is unknown. $\delta_c = \frac{0.07}{0.5} = 0.14$ and $\hat{\delta}_c = \frac{0.07}{0.53} = 0.13$

identical estimated duty cycles below -2 SNR_{dB} . It can also be seen that the simulated communication waveforms have statistically greater duty cycles than the simulated pulse compression radar waveforms at $\text{SNR}_{dB} \geq 2$. These results are similar to those presented in [30], which used a duty cycle threshold of 0.4 to separate pulsed radar waveforms from conventional communication waveforms. Therefore, $\hat{\delta}_c$ is chosen as a suitable feature for use in the classifier system.

This research uses a duty cycle threshold of 0.42 to arbitrarily decide if a signal is a pulse or not in the observed time interval. The duty cycle threshold of 0.42 provided a good When the estimated duty cycle is less than or equal to 0.42 it is treated as a pulse and all samples of $|r[n]|_{S_{smoothed}}^2 \leq 0.42 \hat{P}_0$ are set to zero. This process allows the system to

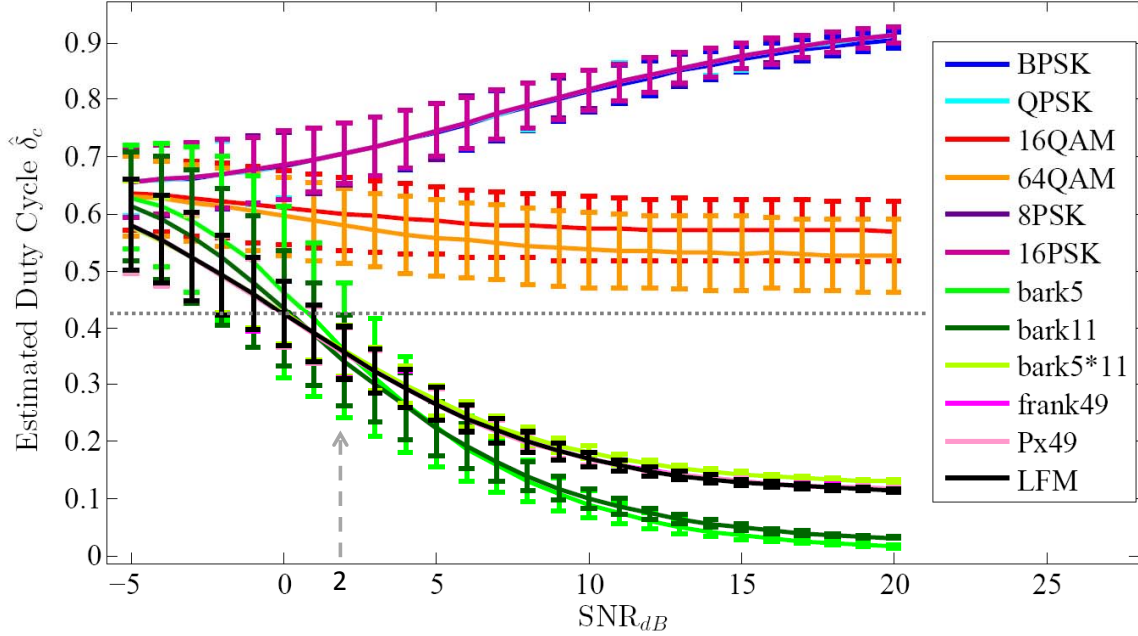


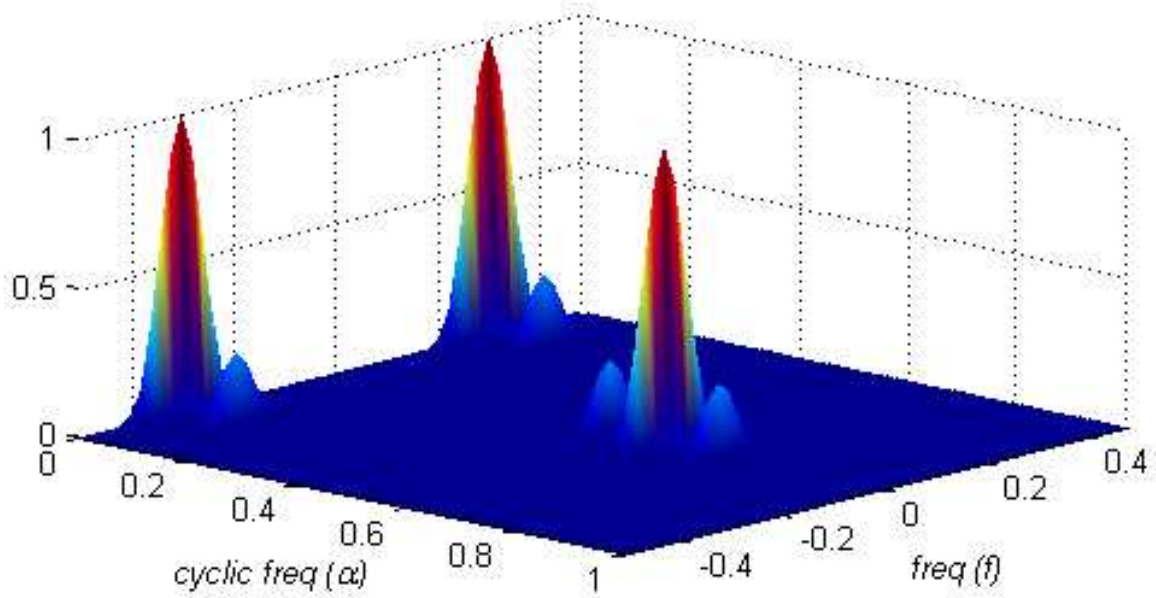
Figure 3.6: Estimated $\hat{\delta}_c$ over a range of SNR_{dB} with 95% confidence intervals calculated from 3,000 estimates per waveform per SNR_{dB} .

ignore samples that contain only noise and attempts to reduce the total amount of noise in the received observation without hindering the received signal pulse.

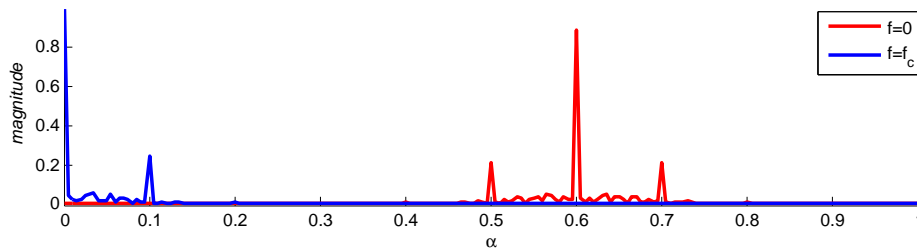
3.3.2 Cyclic Spectral Correlation.

The SCF for the received waveforms was estimated using the Frequency Smoothing Algorithm explained in Section 2.4.2. For brevity, only BPSK and QPSK examples are shown to highlight the cyclic features used in the classifier. Figure 3.7 shows the estimated SCF for a simulated BPSK waveform at a SNR of 20 dB and Figure 3.8 shows the estimated SCF for a simulated QPSK waveform at a SNR of 20 dB. Comparing the figures, one can see that BPSK has a large cyclic feature for frequency $f = 0$ and cyclic frequency $\alpha = 2 f_c = 0.6 f_s$, but QPSK does not. It can also be seen that the ratio between the SCF values for $\alpha = 2 f_c, f = 0$ and $\alpha = 0, f = f_c$ is about one for BPSK and very low for QPSK.

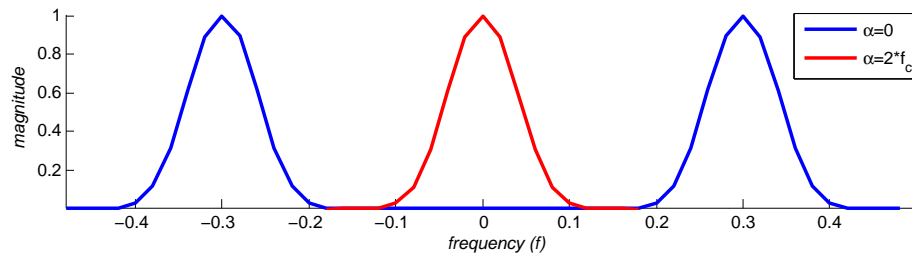
$$\left(\frac{S_{X_T}^{2f_c}(n, 0)_{BPSK}}{S_{X_T}(n, f_c)_{BPSK}} \right) \approx 1 \quad \left(\frac{S_{X_T}^{2f_c}(n, 0)_{QPSK}}{S_{X_T}(n, f_c)_{QPSK}} \right) \approx 0$$



(a) Simulated BPSK SCF Estimate

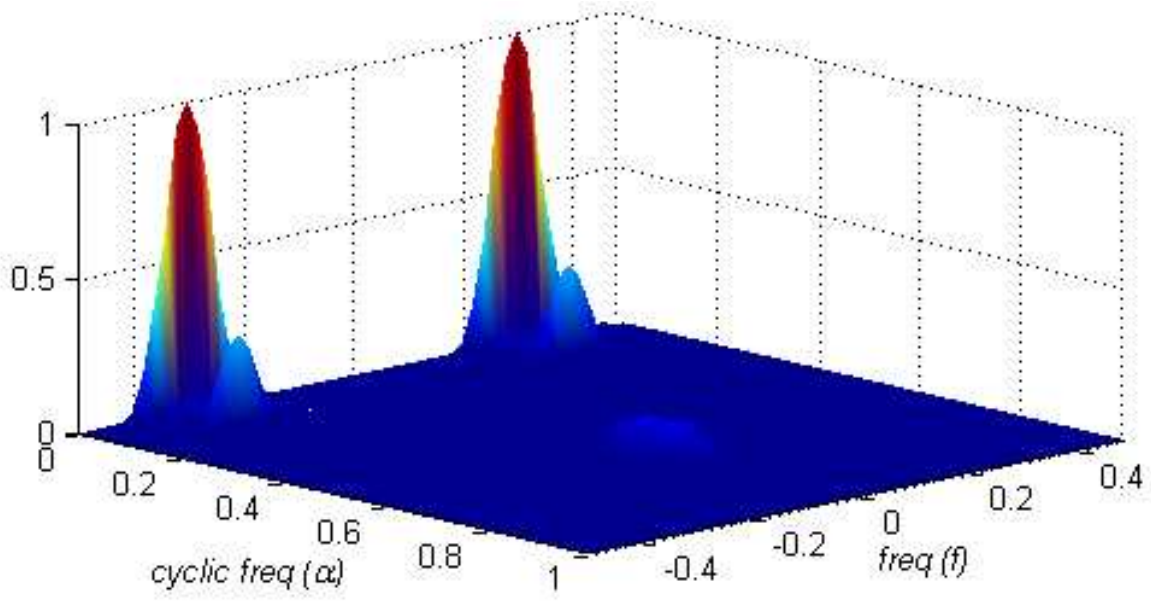


(b) Frequency Profiles of BPSK SCF

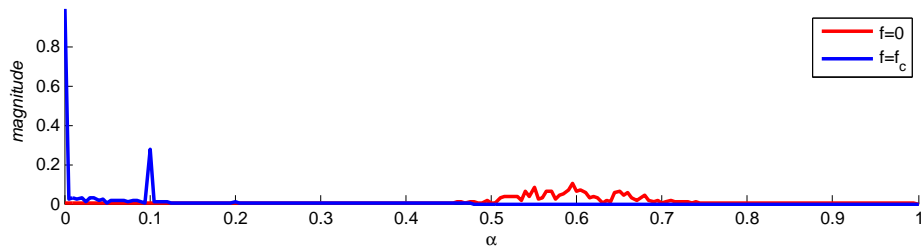


(c) Cyclic Frequency Profiles of BPSK SCF

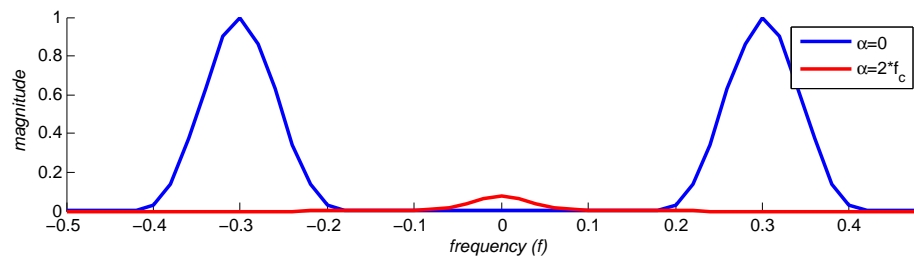
Figure 3.7: Estimated BPSK SCF at $\text{SNR} = 20\text{dB}$ with carrier frequency, $f_c = 0.3 f_s$, and a bandwidth, $W = 0.2 f_s = 2 \frac{1}{T_{Sym}}$, using frequency smoothing with $N = 4096$ and $N' = 328$.



(a) Simulated QPSK SCF Estimate

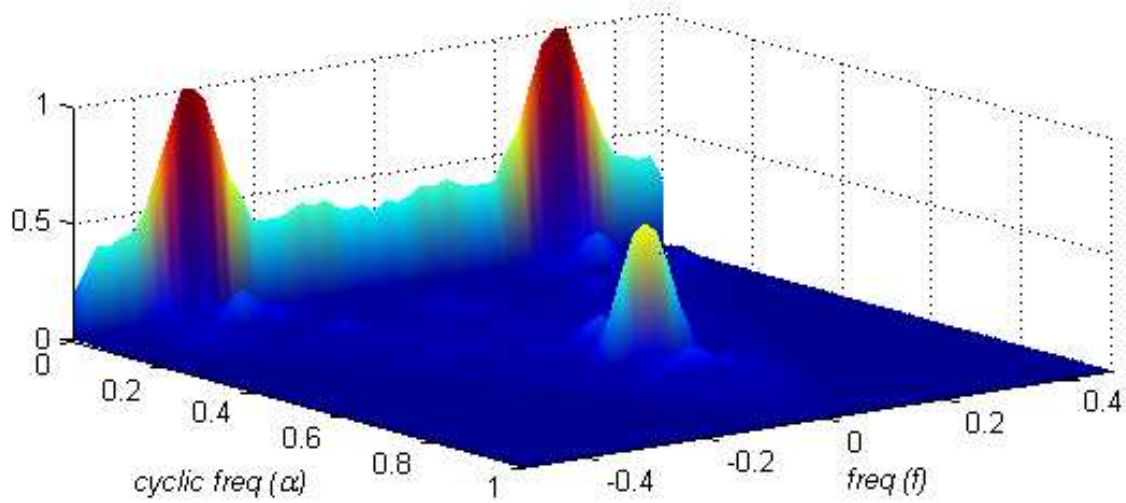


(b) Frequency Profiles of QPSK SCF

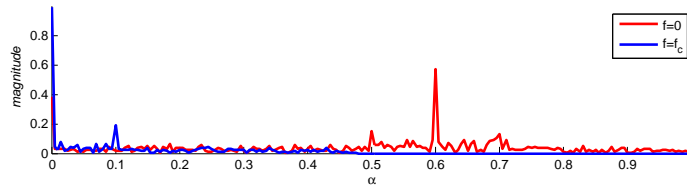


(c) Cyclic Frequency Profiles of QPSK SCF

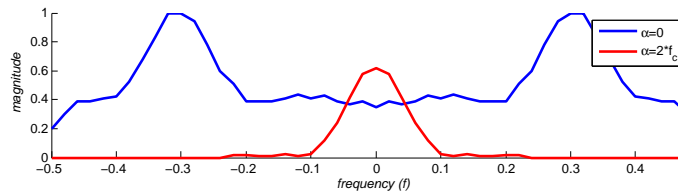
Figure 3.8: Estimated QPSK SCF at $\text{SNR} = 20\text{dB}$ with carrier frequency, $f_c = 0.3 f_s$, and a bandwidth, $W = 0.2 f_s = 2 \frac{1}{T_{Sym}}$, using frequency smoothing with $N = 4096$ and $N' = 328$.



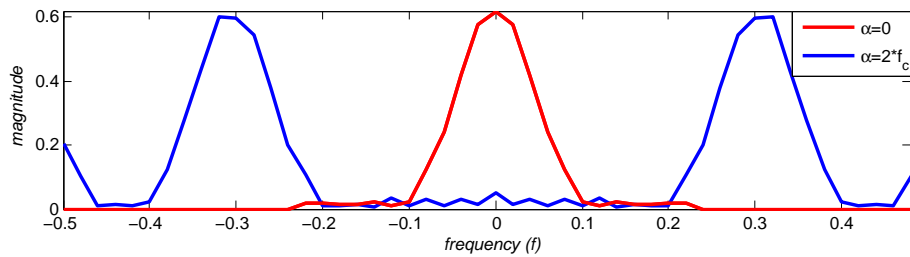
(a) Simulated BPSK SCF Estimate



(b) Frequency Profiles of BPSK SCF



(c) Cyclic Frequency Profiles of BPSK SCF



(d) Cyclic Frequency Profiles of BPSK SCF with Adjusted PSD

Figure 3.9: Estimated BPSK SCF at $\text{SNR} = -5\text{dB}$ with carrier frequency, $f_c = 0.3 f_s$, and a bandwidth, $W = 0.2 f_s = 2 \frac{1}{T_{Sym}}$, using frequency smoothing with $N = 4096$ and $N' = 328$.

Table 3.1: SCF Classifier Features

“High Resolution”	$\left(\frac{S_{X_T}^{2*f_c}(n,0)_{\Delta f}}{S_{X_T}(n,f_c)_{\Delta f, Adj}} \right)_{N'=36}^{N=4096}$	$\left(\frac{MAX_f(S_{X_T}^{2*f_c}(n,f)_{\Delta f})}{MAX_f(S_{X_T}(n,f)_{\Delta f, Adj})} \right)_{N'=36}^{N=4096}$
“Low Resolution”	$\left(\frac{S_{X_T}^{2*f_c}(n,0)_{\Delta f}}{S_{X_T}(n,f_c)_{\Delta f, Adj}} \right)_{N'=328}^{N=4096}$	$\left(\frac{MAX_f(S_{X_T}^{2*f_c}(n,f)_{\Delta f})}{MAX_f(S_{X_T}(n,f)_{\Delta f, Adj})} \right)_{N'=328}^{N=4096}$

Furthermore, Figure 3.9 shows the estimated SCF for a simulated BPSK with SNR = $-5dB$. It is apparent by comparing Figure 3.7 and Figure 3.9 that the noise floor for the PSD (SCF where $\alpha = 0$) has increased and the cyclic feature $S_{X_T}^{2f_c}(n, 0)$ has decreased. To maintain a ratio of about 1 between the specified SCF estimates, the noise floor is subtracted from the PSD estimate. This adjusted PSD estimate is denoted as $S_{X_T}^0(n, f_0)_{Adj}$ and the result is shown in Figure 3.9d. It is easily seen that the ratio between the $S_{X_T}^{2f_c}(n, 0)$ estimate and the adjusted $S_{X_T}^0(n, f_c)_{Adj}$ estimate is about 1.

$$S_{X_T}^0(n, f_c)_{Adj} = S_{X_T}^0(n, f_c) - \text{Noise Floor} \quad (3.16)$$

Four variants of these ratios are used as features in the classifier system. One feature, which has been discussed, is the ratio between specific SCF estimates $\left(\frac{S_{X_T}^{2f_c}(n,0)}{S_{X_T}(n,f_c)_{Adj}} \right)$. Another feature is the ratio between the estimated SCF frequency slices’ maximum peaks for $\alpha = 2f_c$ and $\alpha = 0$, $\left(\frac{MAX_f(S_{X_T}^{2f_c}(n,f))}{MAX_f(S_{X_T}(n,f)_{Adj})} \right)$. These two features are calculated using the frequency smoothing SCF estimation technique from Equation (2.49). Each signal observation is $N = 4096$ samples long. A less reliable, ‘high’ resolution SCF estimate where $N' = 36$ and a more reliable, ‘low’ resolution SCF estimate where $N' = 328$ are used to provide the four features used in the classifier system. The features used from SCF analysis are explicitly shown in Table 3.1. All the simulated waveforms’ values for the ‘low resolution’ feature in column 1 of Table 3.1 over the SNR range tested are shown in Figure 3.10 with their 95% confidence intervals for 3,000 simulated observations per waveform per SNR.

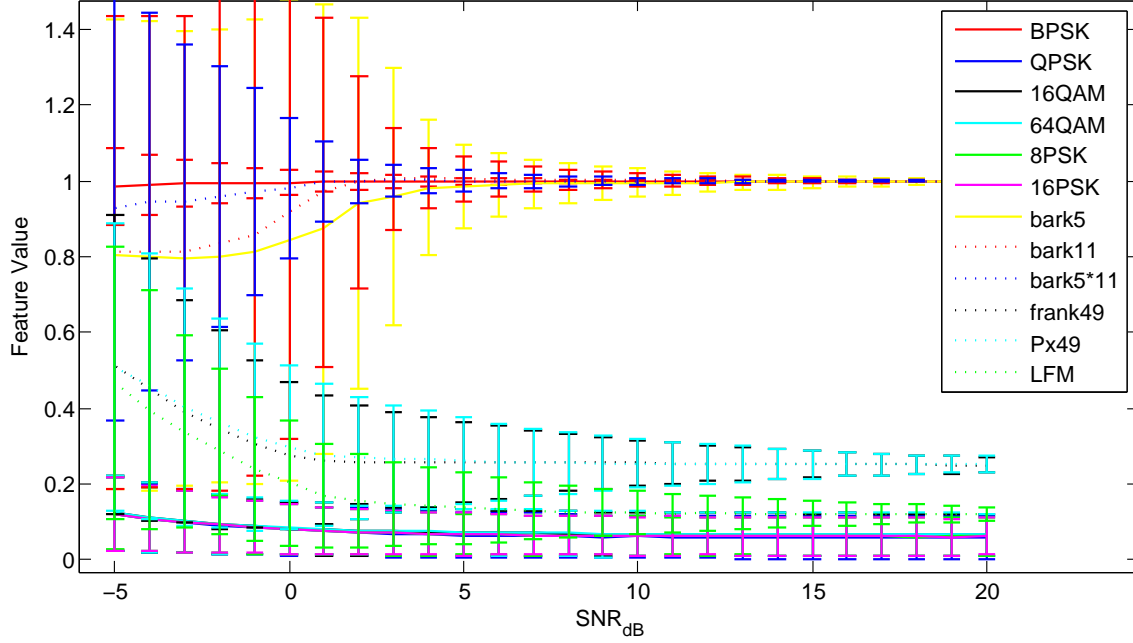


Figure 3.10: Estimated SCF feature ratio using ‘low’ resolution feature from Table 3.1

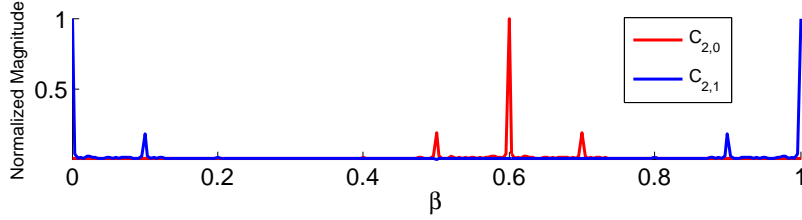
For computational efficiency, only the SCF slices for the relevant cyclic frequencies, $\alpha = 0$, and $\alpha = 2f_c$, are estimated to calculate the features.

3.3.3 Cyclic Cumulants.

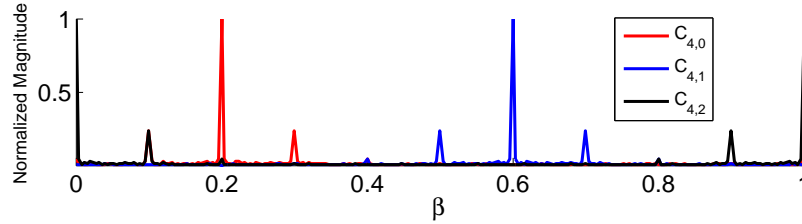
The received waveform $r[n]$ cumulants are calculated from the discrete, time-sampled received waveforms’ estimated moments. The discrete TMF for zero time-lag is modified from Equation (2.51) to the form

$$R_r[m, \tau = 0]_{n,q} \triangleq \mathbf{E}[r[m]^{n-q} (r^*[m])^q] \approx r[m]^{n-q} (r^*[m])^q \quad (3.17)$$

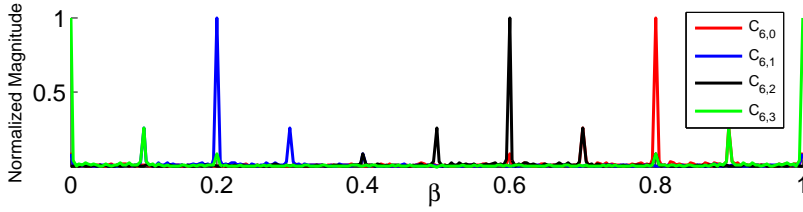
where m is the discrete sample index, and $R_r[m, \tau = 0]_{n,q}$ is the n th-order, q -conjugate moments for time sample m . The moments were estimated according to Equation (3.17) and the cumulant equations from Table 2.5 were used to calculate the estimated n th-order q -conjugate cumulants. Taking the cumulant’s discrete fourier transform (DFT) gives the



(a) Estimated BPSK 2nd-Order Cumulant Spectrums



(b) Estimated BPSK 4th-Order Cumulant Spectrums



(c) Estimated BPSK 6th-Order Cumulant Spectrums

Figure 3.11: Estimated n -order q -conjugate cyclic cumulant spectrums calculated from a BPSK waveform with $\text{SNR} = 20\text{dB}$ using Equation (3.18).

CTCF which is used to calculate the cyclic temporal cumulants (CTCs).

$$C_x^{\beta k} [m, 0]_{n,q} = \sum_{m'=0}^{N-1} C_x [m', 0]_{n,q} e^{-j2\pi\beta k m' T_s} \quad (3.18a)$$

$$= \sum_{m'=0}^{N-1} C_x [m', 0]_{n,q} e^{-j2\pi k \frac{m'}{N}} \quad (3.18b)$$

The estimated CTCF for a BPSK waveform with $\text{SNR} = 20\text{dB}$ over the cyclic frequencies $0 \leq \beta \leq 1$ is shown in Figure 3.11. The cyclic cumulant's maximum occurs at the cyclic frequency $\beta = (n - 2q) f_c$. Also, one can notice that secondary peaks occur at $\beta = (n - 2q) f_c \pm \frac{1}{T_{\text{Sym}}}$ corresponding to \pm the symbol rate from the max peak. Since not all

Table 3.2: Cyclic Cumulant Features

$ C_{2,1}^{\beta=0} $	$ C_{4,0}^{\beta=4f_c} $	$ C_{8,0}^{\beta=8f_c} $	$\frac{ C_{4,2}^{\beta=0} }{ C_{2,1}^{\beta=0} ^2}$	$\frac{ C_{4,0}^{\beta=4f_c} }{ C_{2,1}^{\beta=0} ^2}$
$\frac{\sqrt[3]{ C_{6,1}^{\beta=4f_c} }}{ C_{2,1}^{\beta=0} }$	$\frac{\sqrt[3]{ C_{6,1}^{\beta=4f_c} }}{\sqrt{ C_{4,0}^{\beta=4f_c} }}$	$\frac{\sqrt[3]{ C_{6,3}^{\beta=0} }}{ C_{2,1}^{\beta=0} }$	$\frac{\sqrt[3]{ C_{6,3}^{\beta=0} }}{\sqrt{ C_{4,0}^{\beta=4f_c} }}$	$\frac{\sqrt[4]{ C_{8,0}^{\beta=8f_c} }}{ C_{2,1}^{\beta=0} }$
$\frac{\sqrt[4]{ C_{8,0}^{\beta=8f_c} }}{\sqrt{ C_{4,0}^{\beta=4f_c} }}$	$\frac{\sqrt[4]{ C_{8,0}^{\beta=8f_c} }}{\sqrt[3]{ C_{6,3}^{\beta=0} }}$	$\frac{\sqrt[4]{ C_{8,2}^{\beta=4f_c} }}{ C_{2,1}^{\beta=0} }$	$\frac{\sqrt[4]{ C_{8,2}^{\beta=4f_c} }}{\sqrt{ C_{4,0}^{\beta=4f_c} }}$	$\frac{\sqrt[4]{ C_{8,2}^{\beta=4f_c} }}{\sqrt[3]{ C_{6,1}^{\beta=4f_c} }}$
$\frac{\sqrt[4]{ C_{8,2}^{\beta=4f_c} }}{\sqrt[3]{ C_{6,3}^{\beta=0} }}$	$\frac{\sqrt[4]{ C_{8,4}^{\beta=0} }}{ C_{2,1}^{\beta=0} }$	$\frac{\sqrt[4]{ C_{8,4}^{\beta=0} }}{\sqrt{ C_{4,0}^{\beta=4f_c} }}$	$\frac{\sqrt[4]{ C_{8,4}^{\beta=0} }}{\sqrt[3]{ C_{6,1}^{\beta=4f_c} }}$	$\frac{\sqrt[4]{ C_{8,4}^{\beta=0} }}{\sqrt[3]{ C_{6,3}^{\beta=0} }}$

modulation types have peaks in every n -order q -conjugate cyclic cumulant spectrum, these cumulants are utilized for features in the proposed classifier system. The peaks of these CTCFs may also be used to estimate the carrier frequency and symbol rates of unknown received waveforms.

For computational efficiency, instead of calculating the entire cyclic cumulant spectrum, the classifier system only estimates the cyclic cumulants' spectrums at the single frequency of interest, $\beta = (n - 2q) f_c$, where the CTCF attains its maximum value. The ratios between the estimated cyclic cumulants' magnitude at cyclic frequency $\beta = (n - 2q) f_c$ are used for features. The features calculated from the estimated CTCFs are listed in Table 3.2.

3.4 Classifier Training

After the received waveform's features are estimated, they are formatted into the feature vector $\underline{\psi}$.

$$\underline{\psi} = [\psi_1, \psi_2, \dots, \psi_{25}] \quad (3.19)$$

Feature vectors estimated from received waveforms whose modulations are known *a priori* are then used to 'train' the classifier. This form of classifier training is known as *supervised*

Table 3.3: Classifier Features

Feature	Equation	Feature	Equation	Feature	Equation
ψ_1	$\left(\frac{S_{X_T}^{2*fc}(n,0)_{\Delta f}}{S_{X_T}(n,fc)_{\Delta f, Adj}} \right)_{N'=328}^{N=4096}$	ψ_{10}	$\frac{ C_{4,0}^{\beta=4fc} }{ C_{2,1}^{\beta=0} ^2}$	ψ_{18}	$\frac{\sqrt[4]{ C_{8,2}^{\beta=4fc} }}{ C_{2,1}^{\beta=0} }$
ψ_2	$\left(\frac{MAX_f(S_{X_T}^{2*fc}(n,f)_{\Delta f})}{MAX_f(S_{X_T}(n,f)_{\Delta f, Adj})} \right)_{N'=328}^{N=4096}$	ψ_{11}	$\frac{\sqrt[3]{ C_{6,1}^{\beta=4fc} }}{ C_{2,1}^{\beta=0} }$	ψ_{19}	$\frac{\sqrt[4]{ C_{8,2}^{\beta=4fc} }}{\sqrt{ C_{4,0}^{\beta=4fc} }}$
ψ_3	$\left(\frac{S_{X_T}^{2*fc}(n,0)_{\Delta f}}{S_{X_T}(n,fc)_{\Delta f, Adj}} \right)_{N'=36}^{N=4096}$	ψ_{12}	$\frac{\sqrt[3]{ C_{6,1}^{\beta=4fc} }}{\sqrt{ C_{4,0}^{\beta=4fc} }}$	ψ_{20}	$\frac{\sqrt[4]{ C_{8,2}^{\beta=4fc} }}{\sqrt[3]{ C_{6,1}^{\beta=4fc} }}$
ψ_4	$\left(\frac{MAX_f(S_{X_T}^{2*fc}(n,f)_{\Delta f})}{MAX_f(S_{X_T}(n,f)_{\Delta f, Adj})} \right)_{N'=36}^{N=4096}$	ψ_{13}	$\frac{\sqrt[3]{ C_{6,3}^{\beta=0} }}{ C_{2,1}^{\beta=0} }$	ψ_{21}	$\frac{\sqrt[4]{ C_{8,2}^{\beta=4fc} }}{\sqrt[3]{ C_{6,3}^{\beta=0} }}$
ψ_5	$\hat{\delta}_c = \frac{P_{avg}}{\hat{P}_0}$	ψ_{14}	$\frac{\sqrt[3]{ C_{6,3}^{\beta=0} }}{\sqrt{ C_{4,0}^{\beta=4fc} }}$	ψ_{22}	$\frac{\sqrt[4]{ C_{8,4}^{\beta=0} }}{ C_{2,1}^{\beta=0} }$
ψ_6	$ C_{2,1}^{\beta=0} $	ψ_{15}	$\frac{\sqrt[4]{ C_{8,0}^{\beta=8fc} }}{ C_{2,1}^{\beta=0} }$	ψ_{23}	$\frac{\sqrt[4]{ C_{8,4}^{\beta=0} }}{\sqrt{ C_{4,0}^{\beta=4fc} }}$
ψ_7	$ C_{4,0}^{\beta=4fc} $	ψ_{16}	$\frac{\sqrt[4]{ C_{8,0}^{\beta=8fc} }}{\sqrt{ C_{4,0}^{\beta=4fc} }}$	ψ_{24}	$\frac{\sqrt[4]{ C_{8,4}^{\beta=0} }}{\sqrt[3]{ C_{6,1}^{\beta=4fc} }}$
ψ_8	$ C_{8,0}^{\beta=8fc} $	ψ_{17}	$\frac{\sqrt[4]{ C_{8,0}^{\beta=8fc} }}{\sqrt[3]{ C_{6,3}^{\beta=0} }}$	ψ_{25}	$\frac{\sqrt[4]{ C_{8,4}^{\beta=0} }}{\sqrt[3]{ C_{6,3}^{\beta=0} }}$
ψ_9	$\frac{ C_{4,2}^{\beta=0} }{ C_{2,1}^{\beta=0} ^2}$				

learning and is shown in Figure 3.12. The classifier uses ‘training’ $\underline{\psi}$ vectors for each modulation type to estimate the 25-dimensional PDF for that modulation. All features used by the classifier system are listed in Table 3.3.

The classification model used in this research assumes that the $\underline{\psi}$ feature values for each class have a multivariate-Gaussian distribution represented by

$$P(\underline{\psi}|k) = \frac{1}{(2\pi)^{\frac{25}{2}} \det(\Sigma_k)^{\frac{1}{2}}} \exp \left[-\frac{1}{2} (\underline{\psi} - \hat{\underline{\mu}}_k)^T \hat{\Sigma}_k^{-1} (\underline{\psi} - \hat{\underline{\mu}}_k) \right] \quad (3.20)$$

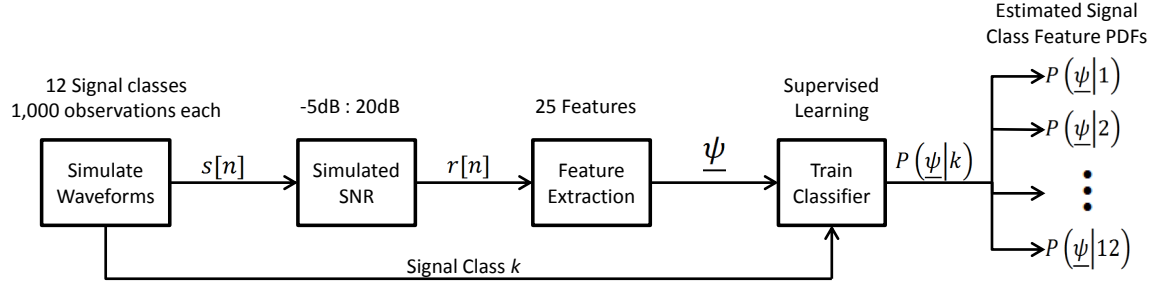


Figure 3.12: Classifier Training

where $P(\underline{\psi}|k)$ is the PDF of a feature vector, $\underline{\psi}$, for a given signal class k , $\hat{\Sigma}_k$ is the estimated feature's sample covariance matrix for signal k , $\hat{\mu}_k$ is a vector of estimated feature sample means of signal k , $(\cdot)^T$ denotes the matrix transpose operation, and Σ_k^{-1} is the inverse matrix of Σ_k .

The sample mean and unbiased sample covariance for signal k are estimated during supervised training from M independent estimations of signal k 's features

$$\hat{\mu}_k = \frac{1}{M} \sum_{m=1}^M \underline{\psi}_k \quad (3.21a)$$

$$\hat{\Sigma}_k = \frac{1}{M-1} \sum_{m=1}^M (\underline{\psi}_k - \hat{\mu}_k)(\underline{\psi}_k - \hat{\mu}_k)^T \quad (3.21b)$$

where $\underline{\psi}_k$ are calculated features from observations known to be from signal class k .

The classifier was trained for each signal class at each SNR using $\underline{\psi}$ vectors extracted from 1,000 independently simulated waveforms of each signal class at each simulated SNR. All twelve signal class waveforms were simulated for 26 levels of SNR from 20dB to -5dB, totaling $12 \times 1,000 = 12,000$ $\underline{\psi}$ vectors used for training each SNR and $12,000 \times 26 = 312,000$ $\underline{\psi}$ vectors used for training overall. The MATLAB[®] command 'ClassificationDiscriminant.fit' with the 'diagQuadratic' option was used to estimate the signal class feature PDFs, $P(\underline{\psi}|k)$ from the training observations.

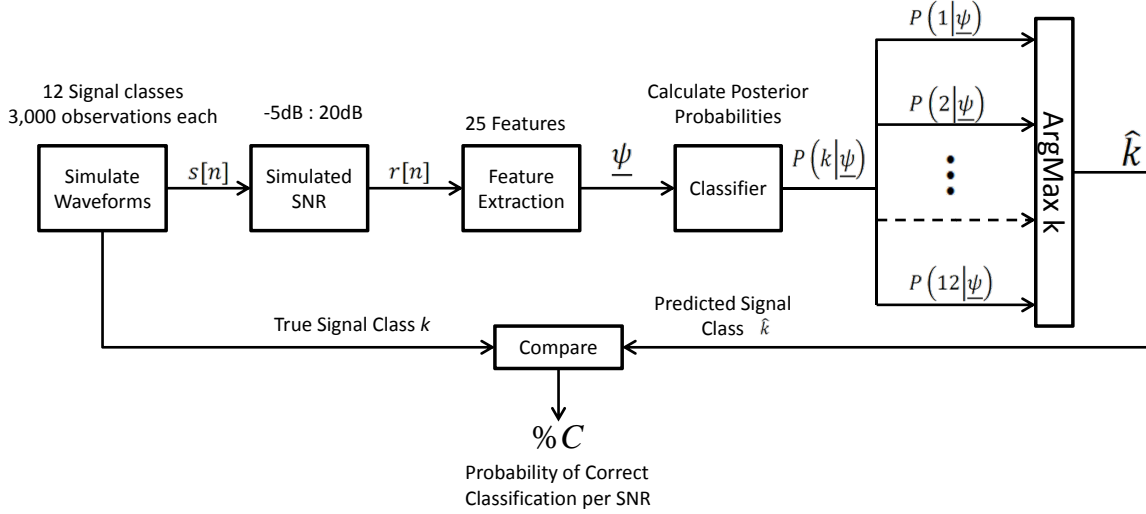


Figure 3.13: Test the Classifier

3.5 Performance Criteria

Classifier predictions from independent test observations are used to approximate the classifier performance for each simulated SNR. Using the estimated $P(\underline{\psi}|k)$ for each signal class developed through the training process shown in Figure 3.12, the classifier model calculates the estimated posterior probabilities

$$P(k|\underline{\psi}) = \frac{P(\underline{\psi}|k)P(k)}{P(\underline{\psi})} = \frac{P(\underline{\psi}|k)P(k)}{\sum_{k'=1}^K P(\underline{\psi}|k')P(k')} \quad (3.22)$$

where $P(k|\underline{\psi})$ is the probability that an estimated $\underline{\psi}$ vector is from signal k , the denominator term is a normalization constant to assure that $\sum_{k'=1}^K P(k'|\underline{\psi}) = 1$, and $P(k)$ is the prior probability of $\underline{\psi}$ belonging to signal class k . For this classifier, all signal classes are assumed to be equally likely so $P(k) = \frac{1}{K}$ for all signal classes. This is a classifier predicts the signal class that $\underline{\psi}$ belongs to based on the maximum *a posteriori* (MAP) likelihood

$$\hat{k} = \arg \max_{k=1, \dots, K} P(k|\underline{\psi}) \quad (3.23)$$

The classifier's performance is assessed through the process shown in Figure 3.13 with 3,000 independently simulated observations of each signal class at each known SNR. The

		Predicted Class \hat{k}			
		1	2	...	12
True Class k	1	Number of 1's correctly predicted as 1's	Number of 1's incorrectly predicted as 2's	...	Number of 1's incorrectly predicted as 12's
	2	Number of 2's incorrectly predicted as 1's	Number of 2's correctly predicted as 2's	...	Number of 2's incorrectly predicted as 12's
	⋮	⋮	⋮	⋮	⋮
	12	Number of 12's incorrectly predicted as 1's	Number of 12's incorrectly predicted as 2's	...	Number of 12's correctly predicted as 12's

Figure 3.14: Confusion Matrix

25 features are estimated from each observation and formatted into the feature vector $\underline{\psi}$. $\underline{\psi}$ is then the input to the trained classifier which calculates posterior probabilities that the estimated $\underline{\psi}$ belongs to the signal class k . The posterior probability for the signal class k with the maximum likelihood is then selected as the predicted signal class \hat{k} . The MATLAB[®] ‘predict’ command is used to calculate and compare the posterior probabilities ($P(k|\underline{\psi})$) to make the MAP likelihood classification decision in Equation (3.23).

The ratio of correct class predictions over total predictions is the probability of correct classification

$$\%C = \frac{\text{Total \# of trials where } k_T = \hat{k}}{\text{Total \# of trials}} \quad (3.24)$$

where k_T represents the true signal class and \hat{k} is the predicted signal class. This ratio will represent the classifier’s overall performance. Confusion matrices and receiver operating characteristic (ROC) curves will also be used to illustrate the classifier’s performance for each signal class at SNRs of interest. A confusion matrix provides the true class and predicted class information for all trials as shown in Figure 3.14. A ROC curve illustrates

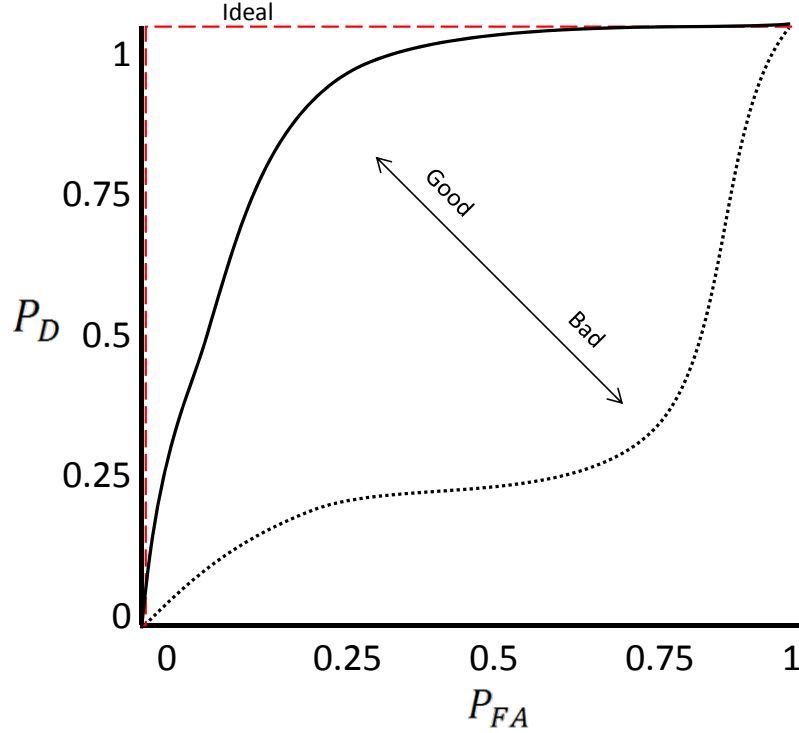


Figure 3.15: ROC Curve Examples

the probability of detection (P_D) versus the probability of false alarm (P_{FA}) for a varying threshold λ at a specific SNR. For this research's application, P_D is the probability that the true signal class will be correctly detected with a threshold λ and P_{FA} is the probability that an incorrect signal class will be falsely detected as the true signal class for the same λ . These probabilities are calculated from the posterior probability mass functions (PMFs) generated by classifier test results using

$$P_{D, \lambda} = \frac{\text{Total \# of trials where } [P(k = k_T | \underline{\psi}) > \lambda]}{\text{Total \# of trials where } k = k_T} \quad (3.25a)$$

$$P_{FA, \lambda} = \frac{\text{Total \# of trials where } [P(k \neq k_T | \underline{\psi}) > \lambda]}{\text{Total \# of trials } k \neq k_T} \quad (3.25b)$$

Examples of generic ROC curves are shown in Figure 3.15.

IV. Results and Analysis

THIS chapter will describe the simulations, present results, and analyze the modulation classification system's performance. It is done by generating probability of correct classification versus SNR_{dB} graphs, ROC curves, and confusion matrices. The feature-based modulation classification system's ability to recognize various signal class groupings will also be tested.

In Section 4.1 the test simulations are explained, including all pertinent signal parameters used for both training and testing. Section 4.2 presents the test simulation results and provides an analysis of them.

4.1 Simulation Setup

The designed modulation classification system was tested for the signal modulations: BPSK, QPSK, 16-QAM, 64-QAM, 8-PSK, 16-PSK, Bi-phase Barker₅, Bi-phase Barker₁₁, Bi-phase Barker_{5,11}, Frank₄₉, PX₄₉, and LFM. First, each signal modulation was independently simulated 4,000 times for each of 26 SNR_{dB} levels, a pulse shaping filter with 50% excess bandwidth was used to band-limit the signals, and independent realizations of AWGN were added to each simulated signal modulation to achieve the desired simulated SNR_{dB} . Each simulated waveform is $2^{12} = 4,096$ samples long with a normalized intermediate frequency (IF) bandwidth of $W = 2B = 0.2f_s$ and was modulated to a carrier frequency $f_c = 0.3f_s$. It is assumed that the carrier frequency and the SNR have been accurately determined and are available to the modulation classification system for feature extraction and classification.

The first test simulation provides a baseline for the modulation classification system's performance. 25 signal features were estimated from 1,000 observations of each signal modulation at all SNR_{dB} levels and were used for training the classifier. This process

was described in Section 3.4 and shown in Figure 3.12. Then, the 25 features were estimated from 3,000 new observations of each signal modulation and were used to test the classifier's performance at each simulated SNR_{dB} . The testing process was described in Section 3.5 and illustrated in Figure 3.13. The classifier's performance for 'ideal' conditions is evaluated by using training and testing observations with the same critical parameters such as bandwidth and carrier frequency.

This ideal case is assessed for three classification scenarios. First, the scenario where the system must classify all distinct signal modulations that were simulated. Second, the signal modulations are grouped by their general modulation family type to assess the system's ability to recognize and classify a signal's modulation family. BPSK, QPSK, and LFM remain their own distinct classes, but 16-QAM and 64-QAM are labeled collectively as M-QAM; 8-PSK and 16-PSK are labeled collectively as M-PSK; Barker₅, Barker₁₁, and Barker_{5,11} are labeled collectively as Bi-Phase Barker; and last, Frank₄₉ and P_X₄₉ are labeled collectively as Poly Phase. Third, the signal modulations are grouped into the broad categories of communication and pulsed radar waveforms. The communication category includes BPSK, QPSK, 16-QAM, 64-QAM, 8-PSK, and 16-PSK while the pulsed radar category includes Bi-phase Barker₅, Bi-phase Barker₁₁, Bi-phase Barker_{5,11}, Frank₄₉, P_X₄₉, and LFM. The classifier is re-trained and re-tested for these relaxed signal groupings to assess its performance when only general information about an unknown waveform's modulation is required.

Next, the modulation classification system's robustness to carrier frequency and bandwidth deviation between the observations used for training and the observations used for testing were assessed. The classification system is still trained with 1,000 observations and tested with 3,000 observations of each signal modulation at all SNR_{dB} levels. The training observations were simulated with $W = 2B = 0.2f_s$ and $f_c = 0.3f_s$ for both tests, but the test observations had varied simulated signal parameters; first with $f_c = 0.3f_s$ and

an increased IF bandwidth $W = 2B = 0.4f_s$, and then with IF bandwidth $W = 2B = 0.2f_s$ and a decreased carrier frequency $f_c = 0.2f_s$.

Probability of correct classification ($\%C$) versus SNR_{dB} graphs, ROC curves, and confusion matrices are generated for each simulation test. These measures of performance were explained in detail in Section 3.5 and are used to attain a comprehensive assessment for the modulation classification system developed in this research work.

4.2 Classifier Performance with Ideal Training Data

4.2.1 Signal Modulation Type Classification.

The designed modulation classification system was first simulated for a classification scenario with ideal conditions. Figure 4.1 shows the performance versus simulated SNR_{dB} for the $\%C$ modulation classification for all twelve signal modulations considered: BPSK, QPSK, 16-QAM, 64-QAM, 8-PSK, 16-PSK, Bi-phase Barker₅, Bi-phase Barker₁₁, Bi-phase Barker_{5,11}, Frank₄₉, Px₄₉, and LFM. This is broken down into the classifier's classification performance for each simulated signal modulation in Figure 4.2. Per the simulation results in Figure 4.1 and Figure 4.2, the modulation classification system has an overall average $\%C > 90\%$ for the simulated signal modulations tested at $\text{SNR} = 9\text{dB}$. Table 4.1 provides the $\text{SNR} = 9\text{dB}$ confusion matrix for the system's performance in Figure 4.2.

Figure 4.2a and Figure 4.2c shows that classifier performances for BPSK, QPSK, 16-QAM, 64-QAM, LFM, Barker₅, Barker₁₁, and Barker_{5,11} are generally increasing over SNR. However, there is some confusion in the simulated classifier system for the other signal modulation types at low SNR levels. The performance for 8-PSK and 16-PSK seem to be negatively correlated in Figure 4.2b up to $\text{SNR} = -4\text{dB}$ and the performance for Frank₄₉ and Px₄₉ seem to be negatively correlated in Figure 4.2d up to $\text{SNR} = 8\text{dB}$.

Table 4.1: Signal Modulation Type Confusion Matrix for SNR = 9dB in Figure 4.1

		Communication						Pulse Compression Radar					
		BPSK	QPSK	16QAM	64QAM	8PSK	16PSK	Barker ₅	Barker ₁₁	Barker _{5,11}	Frank ₄₉	Px ₄₉	LFM
Communication	BPSK	3000	0	0	0	0	0	0	0	0	0	0	0
	QPSK	0	3000	0	0	0	0	0	0	0	0	0	0
	16QAM	0	0	2777	223	0	0	0	0	0	0	0	0
	64QAM	1	0	143	2855	0	0	0	1	0	0	0	0
	8PSK	0	0	0	0	2999	1	0	0	0	0	0	0
	16PSK	0	0	0	0	3	2997	0	0	0	0	0	0
Pulse Compression Radar	Barker ₅	0	0	0	0	0	0	2827	173	0	0	0	0
	Barker ₁₁	0	0	0	0	0	0	391	2607	2	0	0	0
	Barker _{5,11}	0	0	0	0	0	0	2	5	2993	0	0	0
	Frank ₄₉	0	0	0	0	0	0	0	0	0	2496	499	5
	Px ₄₉	0	0	0	0	0	0	0	0	0	1771	1214	15
	LFM	0	0	0	0	1	0	0	0	0	2	5	2992

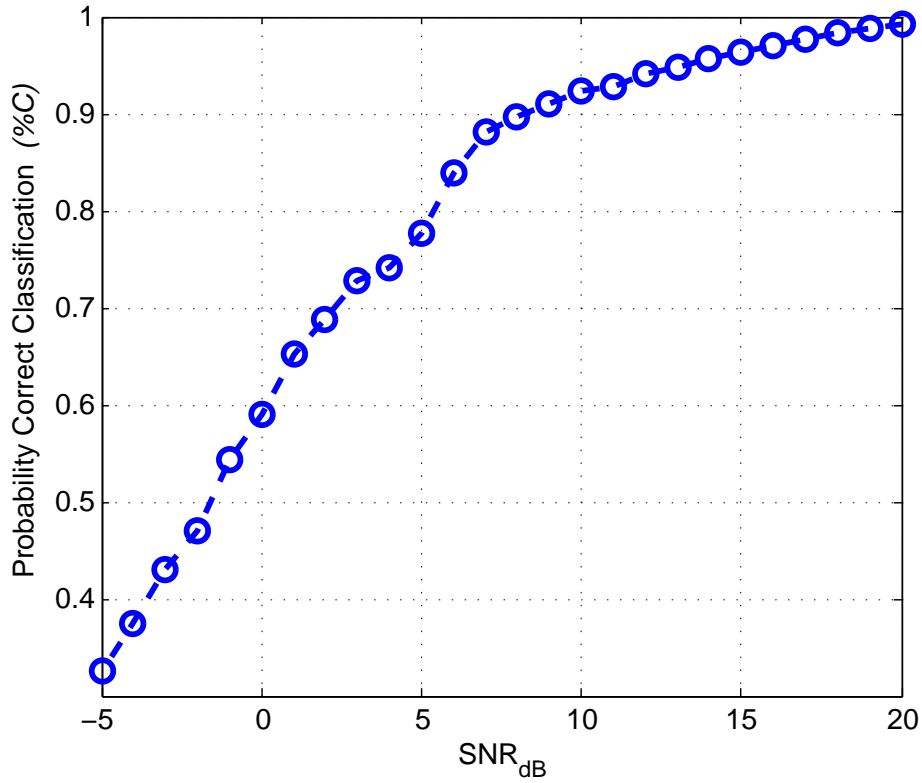
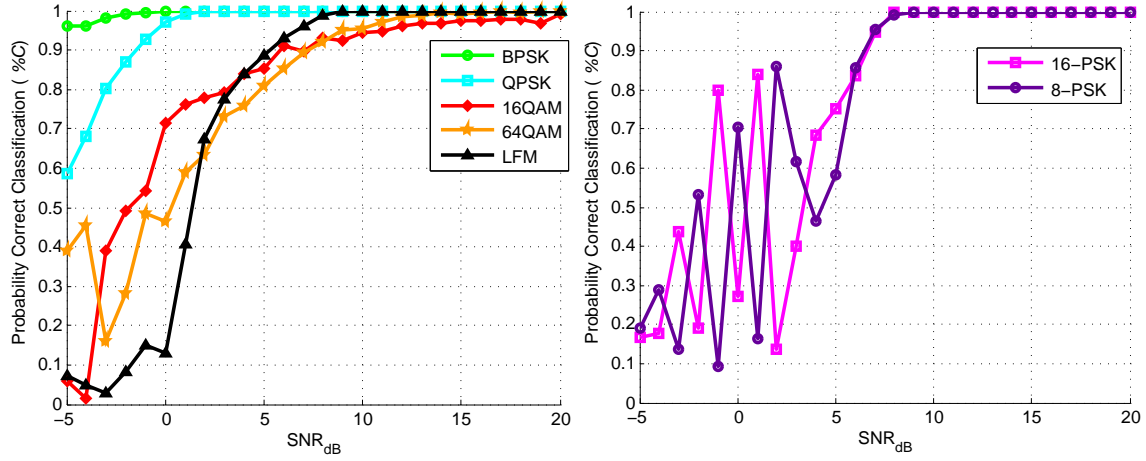
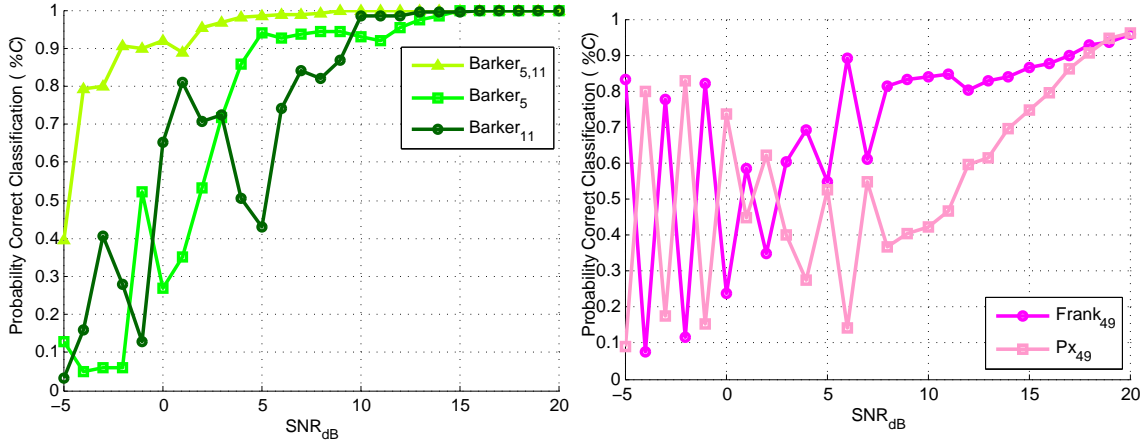


Figure 4.1: Classifier average performance, for all 12 signal modulation types considered, developed from 48,000 simulated observations with $W = 0.2f_s$ and $f_c = 0.3f_s$. 12,000 observations were used for training, 1,000 from each signal modulation type, and 36,000 observations were used for testing, 3,000 from each signal modulation type.



(a) BPSK, QPSK, 16-QAM, 64-QAM, and LFM

(b) 8-PSK and 16-PSK



(c) Barker₅, Barker₁₁, and Barker_{5,11}

(d) Frank₄₉ and Px₄₉

Figure 4.2: Specific modulation type classification performance of system in Figure 4.1

At SNR = 9dB, the simulated system's overall average classification performance %C is greater than 90%, but Table 4.1 shows that more than half of the Px₄₉ modulated pulses were misclassified as Frank₄₉ modulated pulses and about 16% of the Frank₄₉ modulated pulses were misclassified as Px₄₉ modulated pulses. This should not be too surprising since Frank₄₉ and Px₄₉ coded modulated pulses have very similar phase sequences. Additionally, all other simulated signal modulation types, besides Barker₁₁, boast less than 10% misclassification and BPSK, QPSK, 8-PSK, 16-PSK, Barker_{5,11}, and

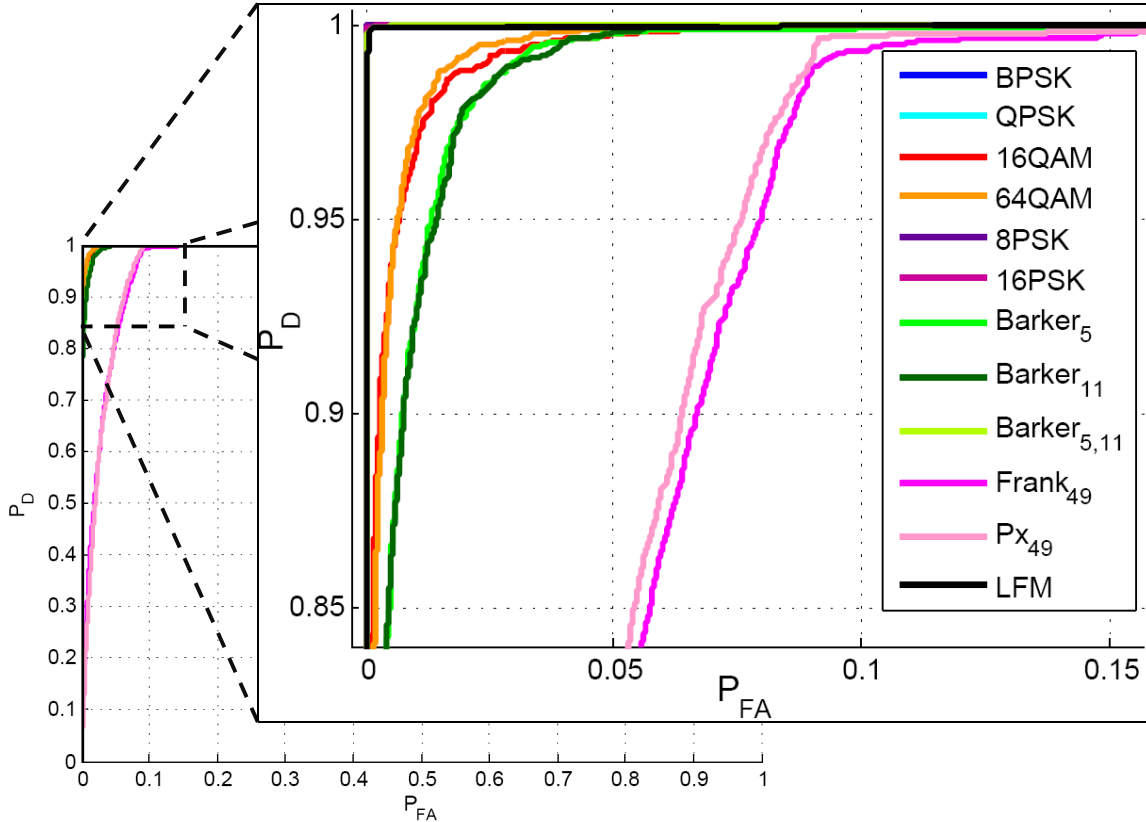


Figure 4.3: Classifier System ROCs for the 12 Modulation Types at SNR = 9dB

LFM were classified with greater than 99% accuracy. It is also interesting to note that only one simulated observation of pulse compression radar modulation was misclassified as a communication modulation and vice versa. Also, the misclassifications are mainly between different orders of similar modulation types such as 16-QAM and 64-QAM; 8-PSK and 16-PSK; Barker₅, Barker₁₁, and Barker_{5,11}; and Frank₄₉ and P_X₄₉.

Figure 4.3 shows the classification system's ROC curves for all signal modulations at SNR = 9dB. The figure region for P_{FA} from 0 to 0.15 and P_D from 0.85 to 1 has been expanded to ease figure readability. Remember, that the ROC curve for any signal modulation 'X', represents the probability of signal modulation 'X' being correctly detected (P_D) and the corresponding probability any other modulation is incorrectly detected as modulation 'X' (P_{FA}) for a sliding threshold. Therefore, it can be seen in

Table 4.2: Signal Modulation Type Confusion Matrix for SNR = 0dB in Figure 4.1

		Communication						Pulse Compression Radar					
		BPSK	QPSK	16QAM	64QAM	8PSK	16PSK	Barker ₅	Barker ₁₁	Barker _{5,11}	Frank ₄₉	Px ₄₉	LFM
Communication	BPSK	2991	0	0	0	0	0	0	9	0	0	0	0
	QPSK	0	2914	79	1	6	0	0	0	0	0	0	0
	16QAM	0	71	2147	731	28	14	0	5	0	3	1	0
	64QAM	0	14	1509	1389	24	40	0	15	0	5	4	0
	8PSK	0	0	48	33	2109	802	7	1	0	0	0	0
	16PSK	0	1	53	33	2089	816	7	1	0	0	0	0
Pulse Compression Radar	Barker ₅	0	0	0	0	0	0	808	1696	182	54	228	32
	Barker ₁₁	0	0	0	0	0	0	187	1960	526	78	193	56
	Barker _{5,11}	0	0	0	0	0	0	15	219	2762	0	4	0
	Frank ₄₉	0	0	0	0	0	0	8	25	2	712	2152	101
	Px ₄₉	0	0	0	0	0	0	11	26	3	643	2207	110
	LFM	0	0	0	0	0	0	24	60	6	595	1928	387

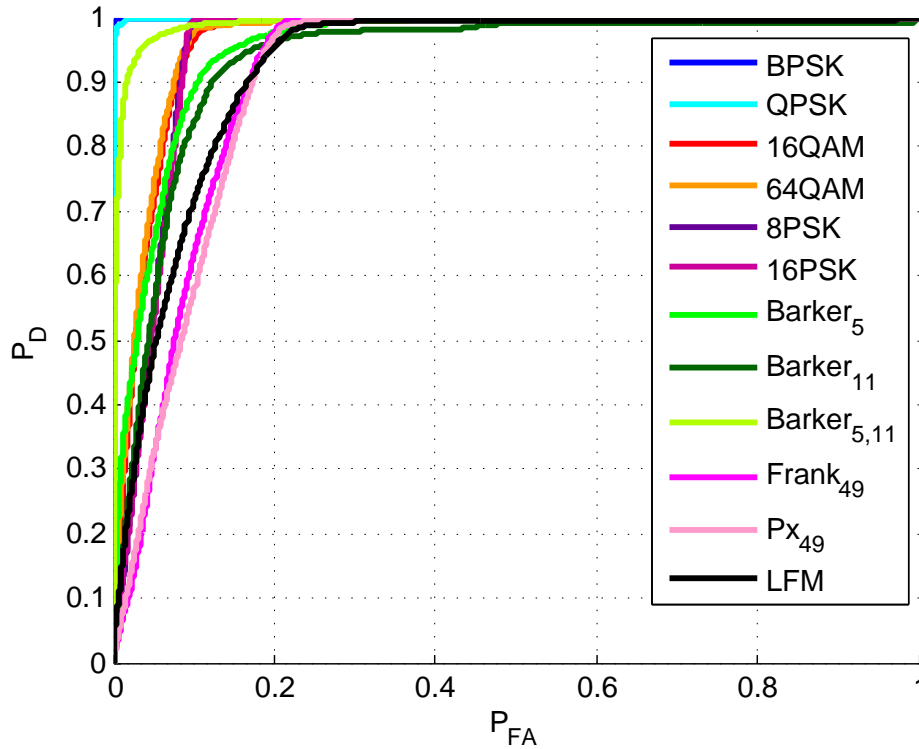


Figure 4.4: Classifier System ROCs for the 12 Modulation Types at SNR = 0dB

Figure 4.3 that specific thresholds can be set to achieve $P_D = 90\%$ with $P_{FA} < 2\%$ for every modulation type but Px₄₉ and Frank₄₉ in a 9dB SNR environment with this

simulated modulation classification system. The simulated $P_{x_{49}}$ and $Frank_{49}$ modulations must sacrifice $P_{FA} \approx 7\%$ to achieve $P_D = 90\%$.

Even though the simulated classification system achieved $\%C < 60\%$ in a 0dB SNR environment, Table 4.2 and Figure 4.2a shows that BPSK and QPSK can still be reliably recognized by the classification system with $\%C > 95\%$ accuracy in such noisy environments. Also, per Figure 4.4, the classification system can achieve $P_D = 90\%$ with $P_{FA} < 10\%$ for the simulated communication modulations and $P_D = 90\%$ with $P_{FA} < 20\%$ for the simulated pulse compression radar modulations by using specific thresholds.

4.2.2 Signal Modulation Family Classification.

For this simulation test, the system's performance recognizing and classifying general modulation families is analyzed. Using the same simulated 48,000 observations at every SNR as before, the classifier was trained and tested to recognize the modulation families given in Table 4.3. Figure 4.5 shows this simulated classifier's overall average probability of correct classification ($\%C$) versus SNR_{dB} performance for the seven modulation families considered compared to the previous classifier for modulation type classification. The

Table 4.3: Modulation Families

Modulation Family	Modulation Types	# of Training/Test Observations per SNR
BPSK	BPSK	1,000/3,000
QPSK	QPSK	1,000/3,000
M-QAM	16-QAM, 64-QAM	2,000/6,000
M-PSK	8-PSK, 16-PSK	2,000/6,000
Bi-Phase Barker	Barker ₅ , Barker ₁₁ , Barker _{5,11}	3,000/9,000
Poly Phase	Frank ₄₉ , Px ₄₉	2,000/6,000
LFM	LFM	1,000/3,000

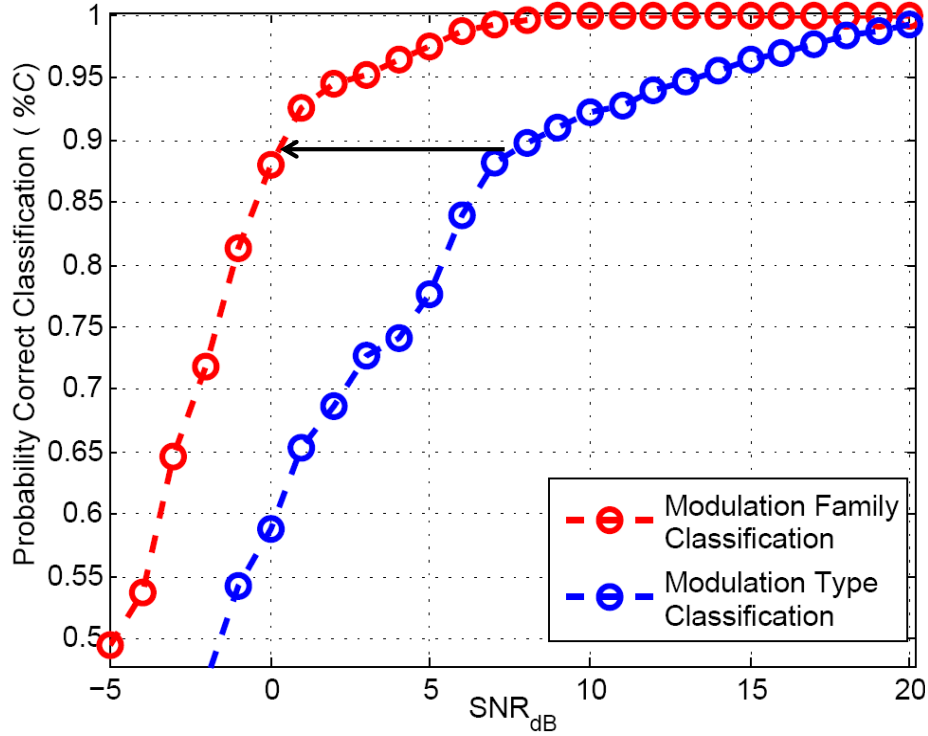


Figure 4.5: Classifier average performance, for the 7 modulation families given in Table 4.3, developed from 48,000 simulated observations with $W = 0.2f_s$ and $f_c = 0.3f_s$. 12,000 simulated observations were used for training and 36,000 simulated observations were used for testing.

classifier’s classification performance for each simulated modulation family is shown in Figure 4.6.

Per the simulation results in Figure 4.5 and Figure 4.6, this modulation classification system achieves overall $\%C \approx 88\%$ at $\text{SNR} = 0\text{dB}$ and the simulated modulation families can be correctly identified with overall $\%C = 90\%$ at an SNR about 8dB less than that required for simulated modulation type classification. Also, every modulation family has a $\%C > 90\%$ for $\text{SNR} > 6\text{dB}$.

Table 4.4 provides the $\text{SNR} = 0\text{dB}$ confusion matrix for the system in Figure 4.5. Since some general modulation families encompass multiple specific modulation types, the total number of observations used for training and testing each modulation family for

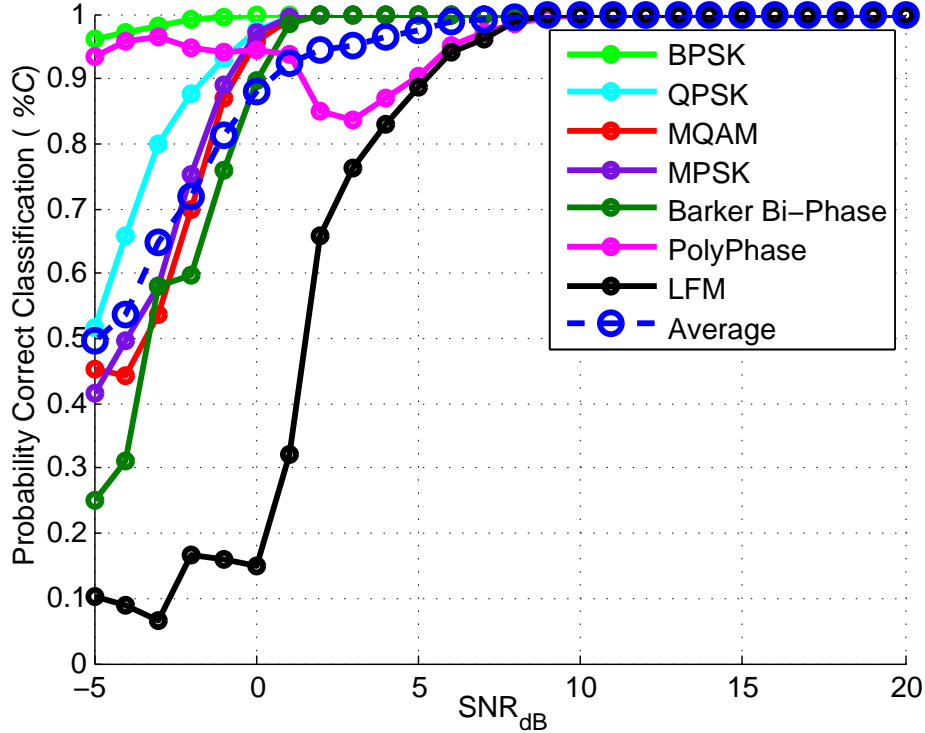


Figure 4.6: Modulation family classification performance of system in Figure 4.5 with overall average system classification performance

this simulation is also given in Table 4.3. Nearly 85% of LFM modulated pulses were misclassified as Poly Phase modulated pulses, but the signal modulations in the other modulation families are recognized with $\%C > 89\%$. Also, there was only one simulated pulse compression radar modulation family observation misclassified as a communication modulation family and only 51 of 18,000 simulated communication modulation family observations were misclassified as a pulse compression radar modulation family.

The ROC curves for the modulation family classification system at $\text{SNR} = 0\text{dB}$ in Figure 4.5 are given in Figure 4.7. The modulation family classification system can set thresholds to achieve $P_D = 90\%$ and $P_{FA} < 1\%$ for all but the simulated Poly Phase and LFM signals at this SNR. The simulated Poly Phase pulse compression modulations can achieve $P_D = 90\%$ and $P_{FA} \approx 10\%$ and the simulated LFM can achieve $P_D = 90\%$ and $P_{FA} \approx 17\%$.

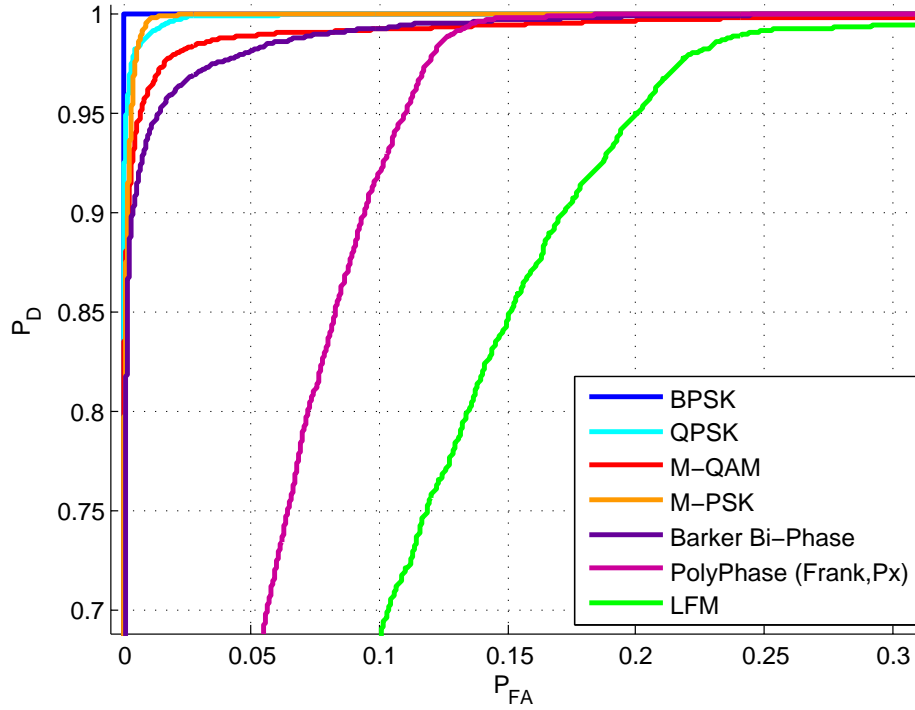


Figure 4.7: Classifier System ROCs for 7 Modulation Families at SNR = 0dB

Table 4.4: Modulation Family Confusion Matrix for SNR = 0dB in Figure 4.5

		Communication				Pulse Compression Radar			# Test Observations
		BPSK	QPSK	MQAM	MPSK	Bi-Phase (Barker)	Poly Phase (Frank, Px)	LFM	
Communication	BPSK	2991	0	0	0	9	0	0	3,000
	QPSK	0	2920	75	5	0	0	0	3,000
	MQAM	0	100	5738	124	12	26	0	6,000
	MPSK	0	1	167	5828	4	0	0	6,000
Pulse Compression Radar	Bi-Phase (Barker)	1	0	0	0	8075	741	183	9,000
	Poly Phase (Frank, Px)	0	0	0	0	21	5675	304	6,000
	LFM	0	0	0	0	46	2500	454	3,000

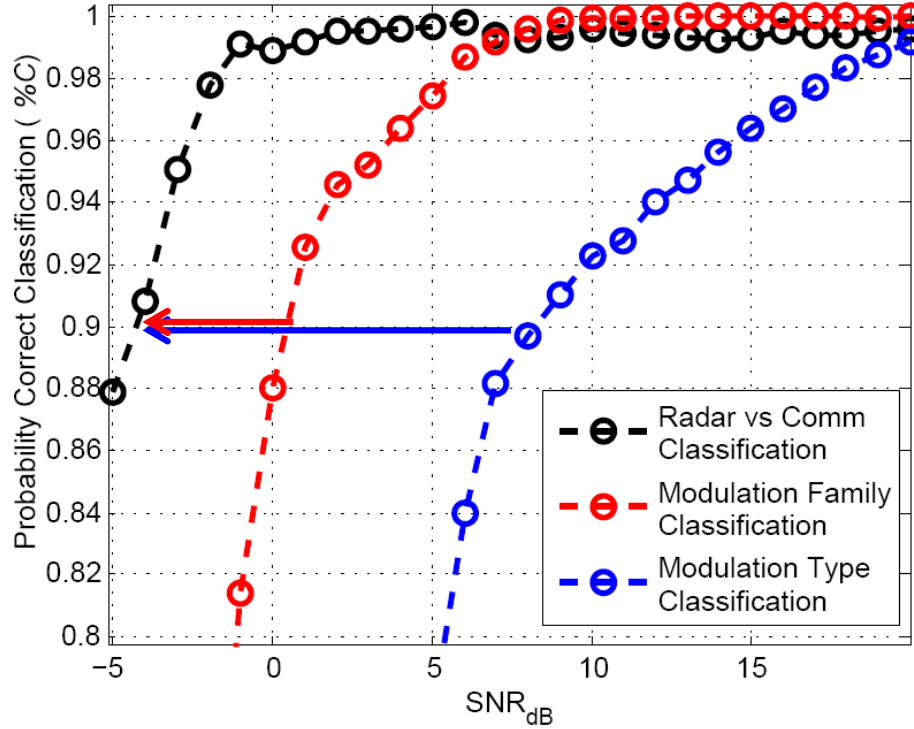


Figure 4.8: Classifier average performance, for distinguishing between communication and pulsed radar modulations according to Table 4.5. System is developed from 48,000 simulated observations with $W = 0.2f_s$ and $f_c = 0.3f_s$. A total of 12,000 simulated observations were used for training and 36,000 simulated observations were used for testing.

4.2.3 Communication vs. Pulse Compression Radar Modulation Classification.

Last, the system's ability to distinguish the simulated communication modulations from the simulated radar pulse compression modulations is shown. For this simulation, the classification system is trained and tested for classifying the 12 signal modulations as either a communication modulation or pulse compression radar modulation as illustrated in Table 4.5. Again, the same 48,000 observations at every SNR_{dB} (4,000 for each of 12 signal modulation types) were used to train and test the classification system for this binary classification decision. Figure 4.8 shows the simulated pulse radar versus communication classifier's overall probability of correct classification (%C) versus SNR_{dB}

Table 4.5: Radar and Communication Waveforms

Signal Type	Modulation Types	# of Training/Test Observations per SNR
Communication	BPSK, QPSK, 16-QAM, 64-QAM, 8-PSK, 16-PSK	6,000/18,000
Radar	Barker ₅ , Barker ₁₁ , Barker _{5,11} , Frank ₄₉ , P _X ₄₉ , LFM	6,000/18,000

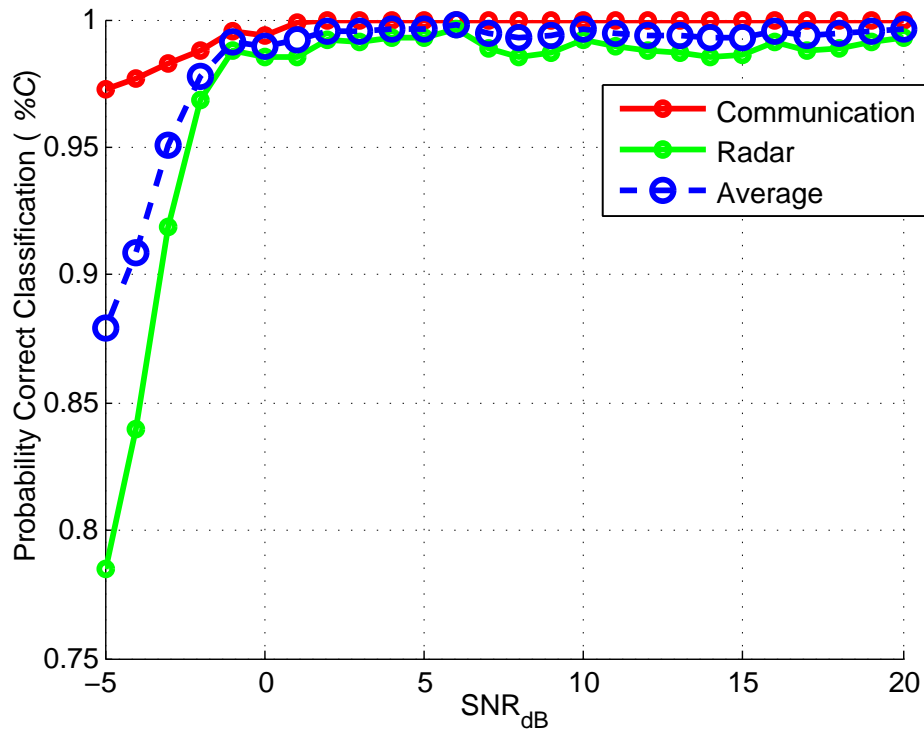


Figure 4.9: Pulsed radar and communication classification performance of system in Figure 4.8 with overall average system classification performance

performance compared to the previous classifiers simulated, and Figure 4.9 shows the system's individual %C for pulse compression radar and communication modulations.

Per the simulation results in Figure 4.8, this modulation classification system achieves %C > 98% at SNR = -1dB and even maintains %C > 90% at SNR = -4dB. It

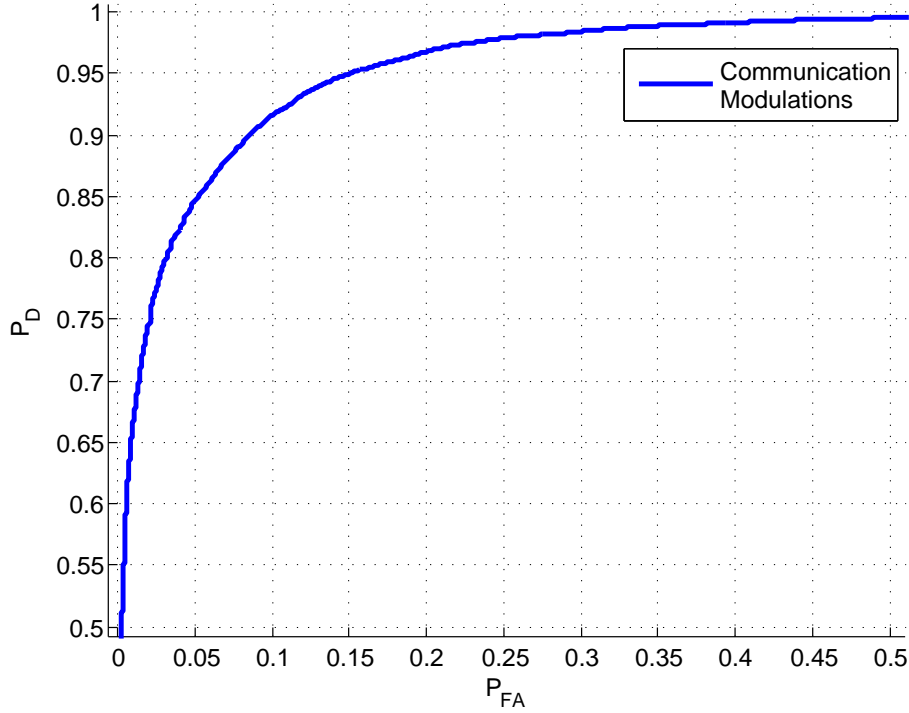


Figure 4.10: Classifier system ROCs for communication detection at $\text{SNR} = -5\text{dB}$. The ROC for pulsed radar detection is simply the reflection of the communication detection ROC about $P_D = 1 - P_{FA}$.

can achieve overall $\%C = 90\%$ between pulse compression radar and communication modulations at an SNR 5dB lower than it can for modulation family classification and about 12dB lower than modulation type classification. The simulations show in Figure 4.8 that the proposed system can provide reliable $\%C > 90\%$ for modulation types down to $\text{SNR} \approx 8\text{dB}$, modulation families down to $\text{SNR} \approx 0.5\text{dB}$, and pulse compression radar versus communication modulation down to $\text{SNR} \approx -4\text{dB}$.

In Figure 4.9, it is seen that pulse compression radar modulations are classified with $\%C$ less than the communication modulation waveforms and never achieve $\%C > 99\%$. Therefore, the overall $\%C$ for the system never achieves $\%C = 100\%$. The communication modulations are classified with very good reliability maintaining $\%C > 96\%$ for $\text{SNR} > -5\text{dB}$, but the pulse compression radar modulation $\%C$ degrades to $\%C \approx 78\%$ by $\text{SNR} = -5\text{dB}$.

Table 4.6: Communication vs Pulsed Radar Modulation Confusion Matrix for SNR = -1dB in Figure 4.8

	Communication	Pulse Compression Radar
Communication	17914	86
Pulse Compression Radar	226	17774

Table 4.7: Communication vs Pulsed Radar Modulation Confusion Matrix for SNR = -5dB in Figure 4.8

	Communication	Pulse Compression Radar
Communication	17503	497
Pulse Compression Radar	3865	14135

Since this test scenario is a binary classification decision, only the communication modulation ROC curve is shown in Figure 4.10. The pulsed radar modulation ROC curve can be inferred from Figure 4.10 as the reflection about $P_D = 1 - P_{FA}$. Thresholds in this simulated classifier system can be set to achieve $P_D > 90\%$ for both communication and pulsed radar modulations with $P_{FA} < 10\%$ at SNR = -5dB. The confusion matrix results for the system in Figure 4.8 at SNR = -1dB and SNR = -5dB are given in Table 4.6 and Table 4.7 respectively. From both Table 4.6 and Table 4.7, one can see that the system tends to incorrectly classify pulse compression radar modulations more than communication modulations.

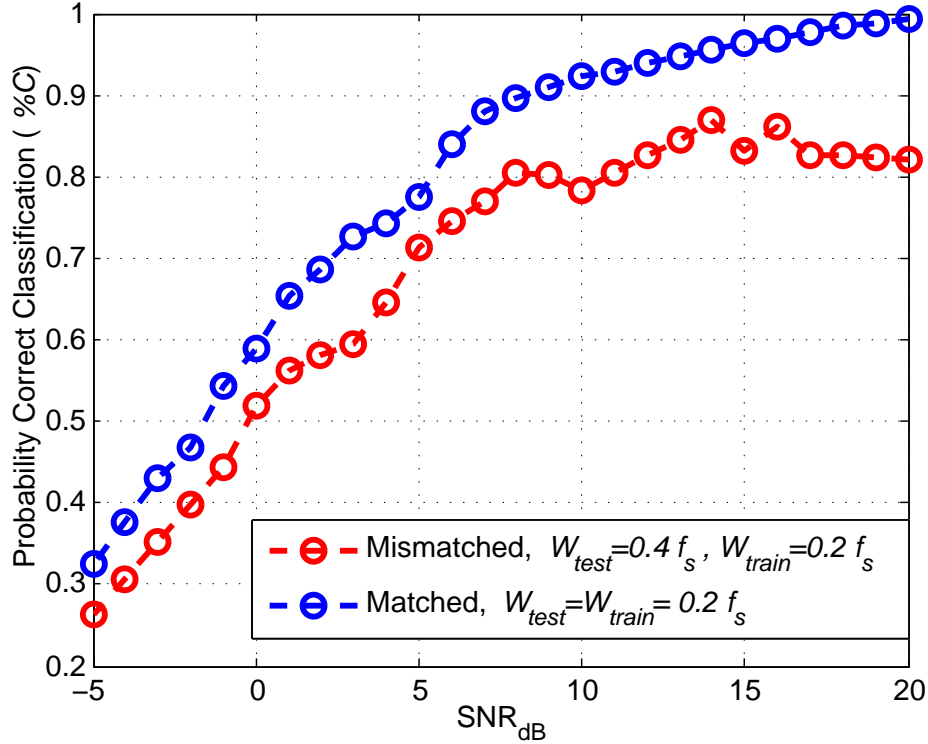
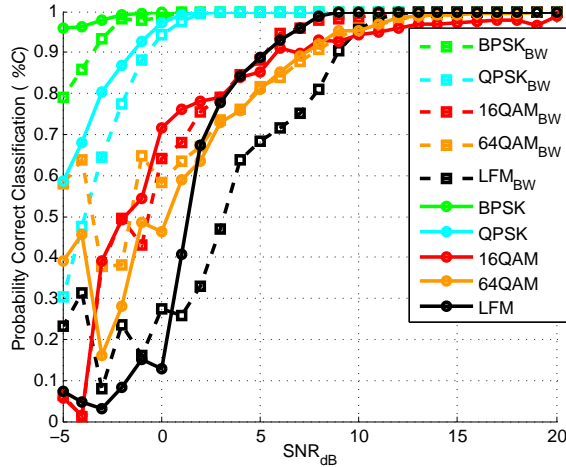


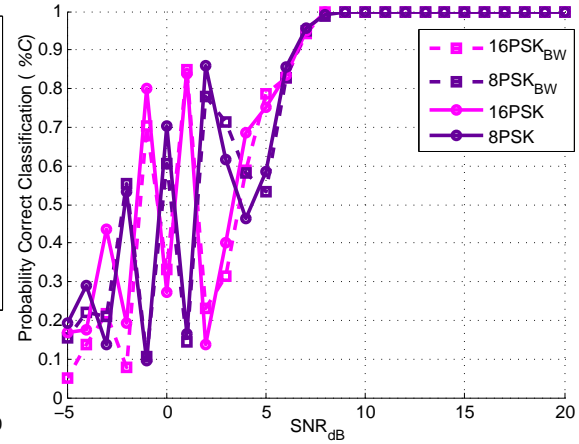
Figure 4.11: Classifier performance with mismatched bandwidth between training and test observations for all 12 signal modulations considered. Trained from 12,000 simulated observations, 1,000 for each signal modulation type, with $W = 0.2f_s$ and $f_c = 0.3f_s$ and tested with 36,000 simulated observations, 3,000 from each signal modulation type, with $f_c = 0.3f_s$ and an increased $W = 0.4f_s$.

4.3 Classifier Bandwidth Sensitivity

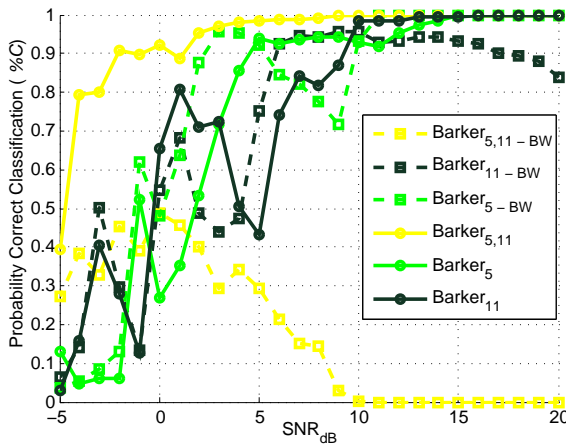
The modulation classification system's sensitivity to bandwidth deviation between the observations used for training and the observations used for testing is assessed in this section. 1,000 observations of each signal modulation at all SNR levels with $W = 2B = 0.2f_s$ and $f_c = 0.3f_s$ are used for training, and the classifier is tested with 3,000 signal modulation observations at each SNR with the same $f_c = 0.3f_s$, but an increased bandwidth $W = 2B = 0.4f_s$. The modulation classification system's sensitivity to mismatched bandwidth between training and testing signal observations is shown by Figure 4.11, Figure 4.12, Table 4.8, and Figure 4.13.



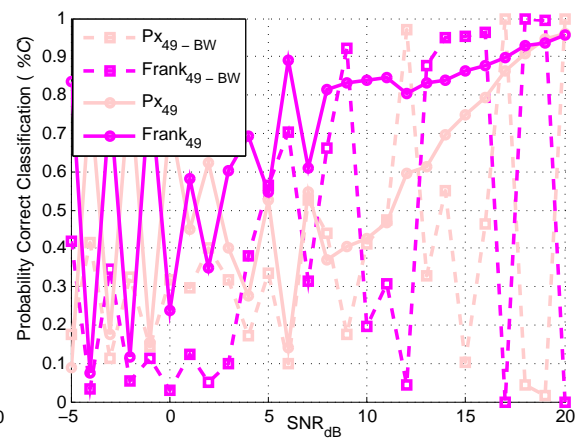
(a) BPSK, QPSK, 16-QAM, 64-QAM, and LFM



(b) 8-PSK and 16-PSK



(c) Barker₅, Barker₁₁, and Barker_{5,11}



(d) Frank₄₉ and Px₄₉

Figure 4.12: Specific signal modulation classification performances compared between the systems with overall average classification performance shown in Figure 4.11. Subscripted ‘BW’ indicates mismatched bandwidths between training data and testing observations and the square markers with dashed lines are the corresponding %C performance for mismatched bandwidth.

From Figure 4.11 it is seen that bandwidth has some effect as overall classification performance was degraded when the test observations had different information bandwidths than the training observations. This mismatch in bandwidth had the largest effect on the Frank₄₉, Px₄₉, and Barker_{5,11} classification performance. The confusion matrix for this simulation at SNR = 8dB is shown in Table 4.8 and the ROC is shown in Figure 4.13.

Table 4.8: Confusion matrix for the 12 modulation types using mismatched training and testing bandwidths at SNR = 8dB in Figure 4.11

		Communication						Pulse Compression Radar					
		BPSK	QPSK	16QAM	64QAM	8PSK	16PSK	Barker ₅	Barker ₁₁	Barker _{5,11}	Frank ₄₉	Px ₄₉	LFM
Communication	BPSK	3000	0	0	0	0	0	0	0	0	0	0	0
	QPSK	0	3000	0	0	0	0	0	0	0	0	0	0
	16QAM	0	0	2935	65	0	0	0	0	0	0	0	0
	64QAM	2	0	272	2724	0	0	0	0	0	2	0	0
	8PSK	0	0	0	0	2967	33	0	0	0	0	0	0
	16PSK	0	0	0	0	8	2992	0	0	0	0	0	0
Pulse Compression Radar	Barker ₅	0	0	0	0	0	0	2331	669	0	0	0	0
	Barker ₁₁	0	0	0	7	0	0	163	2830	0	0	0	0
	Barker _{5,11}	0	0	0	0	0	0	101	2465	434	0	0	0
	Frank ₄₉	0	0	0	0	0	0	0	30	0	1984	957	29
	Px ₄₉	0	0	0	0	0	0	0	0	0	1560	1318	122
	LFM	0	0	0	0	0	0	0	5	0	135	428	2432

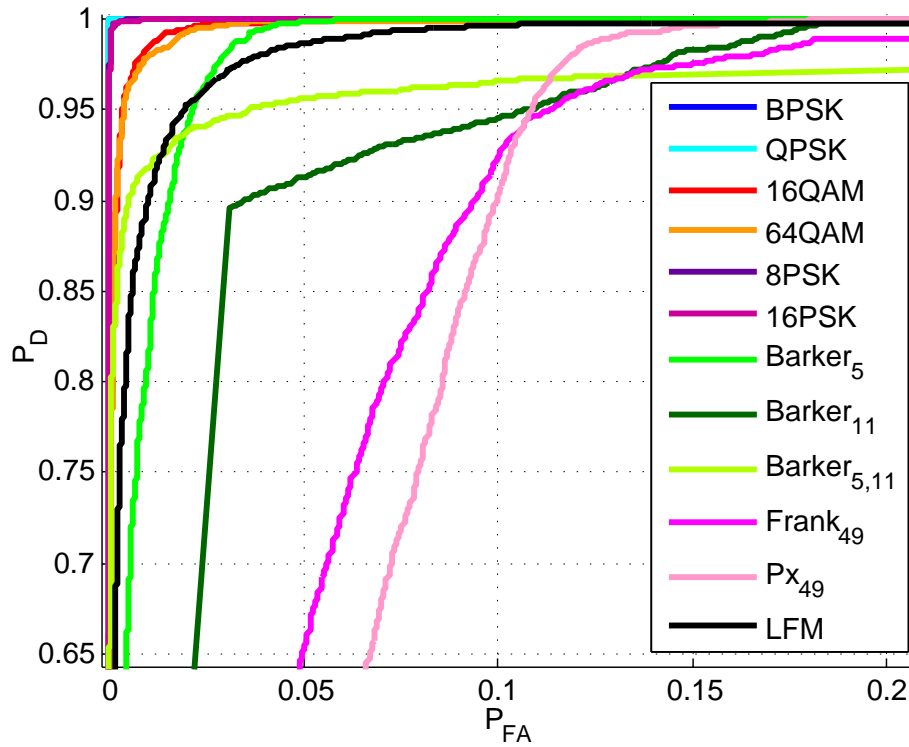


Figure 4.13: Classifier System ROCs for the 12 Modulation Types at SNR = 8dB with Mismatched Bandwidth of $W = 0.4f_s$

Even though the %C using MAP likelihood is very low for some modulation types, the ROCs in Figure 4.13 suggests there is a threshold for each modulation type that will allow $P_D > 90\%$ with $P_{FA} < 10\%$ at SNR = 8dB when all modulations are equally likely.

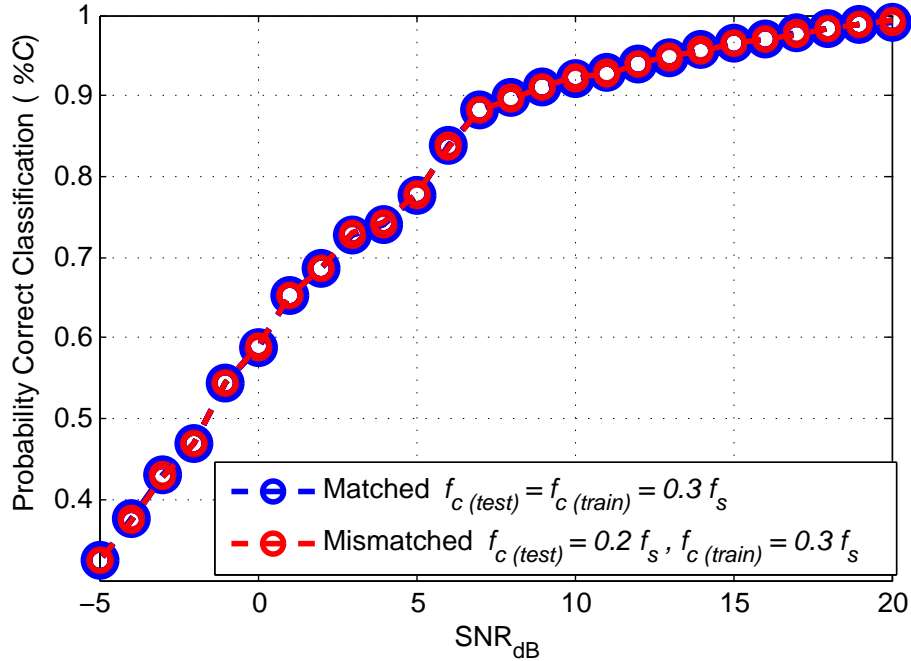


Figure 4.14: Classifier performance with mismatched carrier frequency between training and test observations for all 12 signal modulations considered. Trained from 12,000 simulated observations, 1,000 for each signal modulation type, with $W = 0.2f_s$ and $f_c = 0.3f_s$ and tested with 36,000 simulated observations, 3,000 from each signal modulation type, with matched $W = 0.2f_s$ and a decreased $f_c = 0.2f_s$.

4.4 Classifier Carrier Frequency Sensitivity

The modulation classification system's sensitivity to carrier frequency deviation between the training and testing observations is also assessed. 1,000 observations of each signal modulation at all SNR levels with $W = 2B = 0.2f_s$ and $f_c = 0.3f_s$ were used for classifier training and 3,000 signal modulation observations at each SNR with the same bandwidth, $W = 2B = 0.2f_s$, but a decreased carrier frequency $f_c = 0.2f_s$ were used for testing. The performance sensitivity to carrier frequency is summarized by Figure 4.14.

From Figure 4.14 it is seen that carrier frequency has little effect on the modulation feature PDFs because the overall %C is the same when test observations had different carrier frequencies than the training observations. There was also only little effect on the ROCs and confusion matrices so they are not presented.

V. Conclusions

THE goal of this research was to advance the application of modulation classification by developing and simulating a reliable automatic modulation recognition system capable of discerning between a wide range of both common pulse compression radar and communication modulations. The performance was simulated for varying classification groupings, signal bandwidths, and signal carrier frequencies for a wide range of received SNR.

5.1 Summary

A modulation classification system based on estimated duty cycle and cyclic features was developed and its performance characterized for three distinct class groupings in with ‘ideal’ training data, where received *testing* signal parameters equal *training signal parameters*. Also, performance when the received signal’s bandwidth or carrier frequency was different from the training observations’ was assessed to determine system robustness when suboptimal training data is available.

Using the developed, feature-based maximum *a posteriori* (MAP) classification system with ideal training observations, an average correct modulation type classification rate of $\%C > 90\%$ was achieved at $\text{SNR} = 8\text{dB}$. Furthermore, the BPSK and QPSK signals were classified at $\%C > 95\%$ accuracy at $\text{SNR} = 0\text{ dB}$; the classification system had the most trouble distinguishing between the Frank₄₉ and P_X₄₉ radar pulse compression modulations given they have nearly identical phase sequences. The system’s performance was $\%C \approx 90\%$ at $\text{SNR} = 0\text{dB}$ when it was re-trained to recognize modulation families; it had the most trouble distinguishing between the LFM and Poly-Phase radar modulation families. Last, the system’s performance was $\%C \approx 90\%$ at $\text{SNR} = -4\text{dB}$ when it was re-trained to distinguish only between the pulsed radar and communication

modulations. As the noise corrupting the received signal becomes dominant (lower SNRs), the cyclic features used for classification become less reliable and classification performance degrades.

The classification system's performance suffers when the received signal bandwidth differs from the training signal's bandwidth. The system is still able to classify the communication modulations with comparable reliability, but many pulse compression radar modulation's classification reliability is greatly affected. When training signal's bandwidth $W = 0.2f_s$ and testing signal's bandwidth $W = 0.4f_s$, the overall %C was degraded by about 10%-14% over the simulated SNR range. Alternatively, the mismatched carrier frequency simulation showed little effect on the system's performance. Provided, accurate carrier frequency information is available to the classification system, the mismatched carrier frequency did not effect the classification feature PDFs. These simulations indicated that the developed classification system may be robust to variances in carrier frequency, but requires matched bandwidth between training signal data and received signal's to provide reliable classification performance.

5.2 Impact

This research has taken current communication modulation classification methods and applied them to a larger signal set that includes both communication and pulse compression radar modulations. It has also incorporated many features shown to be successful in current literature, such as duty cycle, spectral correlation, and cyclic cumulants, into one classification system. The results provide evidence that an integrated modulation classification system with application for both communication and pulsed radar modulations is feasible for applications in both Cognitive SDR, Cognitive Radar, and EW operations.

A very broad range of applications have use for automatic modulation research. Cognitive Radio and Radar systems as well as EW operations rely heavily on spectrum

sensing methods that incorporate automatic modulation recognition processes. Cognitive Radios rely on it for spectrum information used in spectrum management and EW operations use it to extract information about non-cooperative signals. Reactive Jamming systems may use automatic modulation recognition to efficiently jam specific modulations without interfering with others. By extending the research to both pulsed radar and communication modulations, this research adds to the very limited literature that addresses integrated automatic radar and communication modulation recognition.

5.3 Recommendations for Future Work

Automatic modulation classification is a challenging task, made even more so by non-cooperative environments. As the number of unknown signal characteristics and the channel interference increases, the difficulty of extracting signal identifiable features is increased. This remains the most challenging aspect of classification systems and is a primary area of necessary research.

This research makes the assumption that the classification system accurately knows the carrier frequency of received signals for feature estimation. Future research can apply carrier frequency estimation processes to the system. Also, extension to additional signal modulation types is an added benefit so as to classify a wider set of signals. These should include spread spectrum, frequency hopping, and orthogonal frequency division multiplexing (OFDM) modulations. Feature analysis would be a good research thrust to determine feature relevance and decide if removing any features improves performance. Also, extending the system for simulations using a MIMO receiver or discerning if a signal was transmitted from a MIMO system is beneficial. As always, increasing the channel complexity to characterize the classification system's performance in multi-path and fast-fading channels is a valuable area for further research. Last, extending these concepts shown in simulation to physical hardware, such as a SDR, is beneficial future research to compare simulated performance with physical test performance.

Bibliography

- [1] Ahmad, T., A. Jameel, and B. Ahmad. “Pattern Recognition using Statistical and Neural Techniques”. *2011 International Conference on Computer Networks and Information Technology (ICCNIT)*, 87 –91. July 2011.
- [2] Axell, E., G. Leus, E. G. Larsson, and H. V. Poor. “Spectrum Sensing for Cognitive Radio : State-of-the-Art and Recent Advances”. *IEEE Signal Processing Magazine*, 29(3):101 –116, May 2012.
- [3] B. Boashash, E. J. Powers and A. M. Zoubir (editors). *Higher-Order Statistical Signal Processing*. Longmen, 1995.
- [4] Brown, W. A., III and H. H. Loomis, Jr. “Digital Implementations of Spectral Correlation Analyzers”. *IEEE Transactions on Signal Processing*, 41(2):703–720, Feb 1993.
- [5] Dobre, O. A., A. Abdi, Y. Bar-Ness, and W. Su. “Survey of Automatic Modulation Classification Techniques: Classical Approaches and New Trends”. *IET Communications*, 1(2):137 –156, April 2007.
- [6] Dobre, O. A., A. Abdi, Y. Bar-Ness, and Wei Su. “Blind Modulation Classification: A Concept Whose Time has Come”. *2005 IEEE Sarnoff Symposium on Advances in Wired and Wireless Communication*, 223 –228. April 2005.
- [7] Duda, R. O., P. E. Hart, and D. G. Stork. *Pattern Classification*. Wiley, second edition, 2001.
- [8] E. C. Farnett, T. B. Howard and G. H. Stevens. *Radar Handbook*. McGraw-Hill Book Co., 1970.
- [9] Gardner, W. A. “Measurement of Spectral Correlation”. *IEEE Transactions on Acoustics, Speech and Signal Processing*, 34(5):1111 – 1123, Oct 1986.
- [10] Gardner, W. A. “The Spectral Correlation Theory of Cyclostationary Time-Series”. *Signal Processing*, 11(1):13–36, 1986.
- [11] Gardner, W. A. *Statistical Spectral Analysis: A Nonprobabilistic Theory*. Prentice Hall, 1988.
- [12] Gardner, W. A. “Exploitation of Spectral Redundancy in Cyclostationary Signals”. *IEEE Signal Processing Magazine*, 8(2):14–36, Apr 1991.
- [13] Gardner, W. A., W. A. Brown, and C. K. Chen. “Spectral Correlation of Modulated Signals: Part I – Analog Modulation”. *IEEE Transactions on Communications*, 35:584–594, Jun 1987.

- [14] Gardner, W. A., W. A. Brown, and C. K. Chen. “Spectral Correlation of Modulated Signals: Part II – Digital Modulation”. *IEEE Transactions on Communications*, 35:595–601, Mar 1996.
- [15] Gardner, W. A., A. Napolitano, and L. Paura. “Cyclostationarity: Half a century of research”. *Signal Processing*, 86(4):639–697, Apr. 2006.
- [16] Gardner, W. A. and C. M. Spooner. “The Cumulant Theory of Cyclostationary Time-Series, Part I: Foundation”. *IEEE Transactions on Signal Processing*, 42(12):3387–3408, Dec 1994.
- [17] Guenther, B. E. *Multi-User signal Classification Via Cyclic Spectral Analysis*. Master’s thesis, Wright State University, Oct 2010.
- [18] Haykin, S., D. J. Thomson, and J. H. Reed. “Spectrum Sensing for Cognitive Radio”. *Proceedings of the IEEE*, 97(5):849 –877, May 2009.
- [19] Jain, A. K., R. P. W. Duin, and J. Mao. “Statistical Pattern Recognition: A Review”. *IEEE Transactions on Pattern Analysis and Machine Intelligence*, 22(1):4 –37, Jan 2000.
- [20] Kay, S. M. *Intuitive Probability and Random Processes Using MATLAB®*. Springer, 2006.
- [21] Levanon, N. and E. Mozeson. *Radar Signals*. Wiley, 2004.
- [22] Like, E. C. *Non-Cooperative Modulation Recognition Via Exploitation of Cyclic Statistics*. Master’s thesis, Wright State University, Dec. 2007.
- [23] Lunden, J. and V. Koivunen. “Automatic Radar Waveform Recognition”. *IEEE Journal of Selected Topics in Signal Processing*, 1(1):124 –136, June 2007.
- [24] Rappaport, T. S. *Wireless Communications: Principles and Practice*. Third edition, 2002.
- [25] Roberts, R. S., W. A. Brown, and Jr. Loomis, H. H. “Computationally Efficient Algorithms for Cyclic Spectral Analysis”. *IEEE Signal Processing Magazine*, 8(2):38 –49, April 1991.
- [26] Sklar, B. *Digital Communications: Fundamentals and Applications*. Prentice-Hall, 2001.
- [27] Swami, A. and B. M. Sadler. “Hierarchical Digital Modulation Classification Using Cumulants”. *IEEE Transactions on Communications*, 48(3):416–429, Mar 2000.
- [28] Toomay, J. C. and P. J. Hannen. *Radar Principles for the Non-Specialist*. SciTech, third edition, 2004.

- [29] Yucek, T. and H. Arslan. “A Survey of Spectrum Sensing Algorithms for Cognitive Radio Applications”, First Quarter 2009.
- [30] Zhang, X., W. You, Q. Guo, and H. Cao. “Recognition Method Studies for Radar and Communication Signals Based on Spectral Correlation”. *2010 3rd International Symposium on Systems and Control in Aeronautics and Astronautics (ISSCAA)*, 363–366. June 2010.

REPORT DOCUMENTATION PAGE

Form Approved
OMB No. 0704-0188

The public reporting burden for this collection of information is estimated to average 1 hour per response, including the time for reviewing instructions, searching existing data sources, gathering and maintaining the data needed, and completing and reviewing the collection of information. Send comments regarding this burden estimate or any other aspect of this collection of information, including suggestions for reducing this burden to Department of Defense, Washington Headquarters Services, Directorate for Information Operations and Reports (0704-0188), 1215 Jefferson Davis Highway, Suite 1204, Arlington, VA 22202-4302. Respondents should be aware that notwithstanding any other provision of law, no person shall be subject to any penalty for failing to comply with a collection of information if it does not display a currently valid OMB control number. **PLEASE DO NOT RETURN YOUR FORM TO THE ABOVE ADDRESS.**

1. REPORT DATE (DD-MM-YYYY) 21-03-2013		2. REPORT TYPE Master's Thesis		3. DATES COVERED (From — To) Oct 2011–Mar 2013	
4. TITLE AND SUBTITLE Automatic Modulation Classification of Common Communication and Pulse Compression Radar Waveforms using Cyclic Features				5a. CONTRACT NUMBER	
				5b. GRANT NUMBER	
				5c. PROGRAM ELEMENT NUMBER	
				5d. PROJECT NUMBER	
				5e. TASK NUMBER	
				5f. WORK UNIT NUMBER	
6. AUTHOR(S) Hadjis, John A., Second Lieutenant, USAF					
7. PERFORMING ORGANIZATION NAME(S) AND ADDRESS(ES) Air Force Institute of Technology Graduate School of Engineering and Management (AFIT/EN) 2950 Hobson Way WPAFB, OH 45433-7765				8. PERFORMING ORGANIZATION REPORT NUMBER AFIT-ENG-13-M-20	
9. SPONSORING / MONITORING AGENCY NAME(S) AND ADDRESS(ES) Air Force Research Laboratory Attn: AFRL RYWE (Dr. Vasu Chakravarthy) 2241 Avionics Circle WPAFB, OH 45433 1(937) 785-5579 ext 4245 Vasu.Chakravarthy@wpafb.af.mil				10. SPONSOR/MONITOR'S ACRONYM(S) AFRL/RWYE	
12. DISTRIBUTION / AVAILABILITY STATEMENT DISTRIBUTION STATEMENT A. APPROVED FOR PUBLIC RELEASE; DISTRIBUTION UNLIMITED				11. SPONSOR/MONITOR'S REPORT NUMBER(S)	
13. SUPPLEMENTARY NOTES This work is declared a work of the U.S. Government and is not subject to copyright protection in the United States.					
14. ABSTRACT This research develops a feature-based MAP classification system and applies it to classify several common pulse compression radar and communication modulations. All signal parameters are treated as unknown to the classifier system except SNR and the signal carrier frequency. The features are derived from estimated duty cycle, cyclic spectral correlation, and cyclic cumulants. The modulations considered in this research are BPSK, QPSK, 16-QAM, 64-QAM, 8-PSK, and 16-PSK communication modulations, as well as Barker ₅ coded, Barker ₁₁ coded, Barker _{5,11} coded, Frank ₄₉ coded, Px ₄₉ coded, and LFM pulse compression modulations. Simulations show that average correct signal modulation type classification %C > 90% is achieved for SNR > 9dB, average signal modulation family classification %C > 90% is achieved for SNR > 1dB, and an average communication versus pulse compression radar modulation classification %C > 90% is achieved for SNR > -4dB. Also, it is shown that the classification performance using selected input features is sensitive to signal bandwidth but not to carrier frequency. Mismatched bandwidth between training and testing signals caused degraded classification of %C ≈ 10% – 14% over the simulated SNR range.					
15. SUBJECT TERMS Spectral Correlation, Automatic modulation Classification, Cyclic Features, Cyclic Cumulants, Radar, Communication					
16. SECURITY CLASSIFICATION OF:			17. LIMITATION OF ABSTRACT	18. NUMBER OF PAGES	19a. NAME OF RESPONSIBLE PERSON
a. REPORT	b. ABSTRACT	c. THIS PAGE			Dr. Richard K. Martin (ENG)
U	U	U	UU	96	19b. TELEPHONE NUMBER (include area code) (937) 2553636 x4625; Richard.Martin@afit.edu